Title
Interfacial Region Thermophysics and Intrinsic Stability of Thin Free Liquid Films

Author
GAN, YU

Publication Date
2011

Peer reviewed|Thesis/dissertation

Interfacial Region Thermophysics and Intrinsic Stability of Thin Free Liquid Films

By

Yu Gan

A dissertation submitted in partial satisfaction of the

requirements for the degree of

Doctor of Philosophy

in

Engineering – Mechanical Engineering

in the

Graduate Division

of the

University of California, Berkeley

Committee in charge:

Professor Van P. Carey, Chair

Professor Ralph Greif

Professor Per F. Peterson

Professor Samuel S. Mao

Spring 2011

UMI copyright page

Abstract

Interfacial Region Thermophysics and Intrinsic Stability of Thin Free Liquid Films

by

Yu Gan

Doctor of Philosophy in Engineering – Mechanical Engineering

University of California, Berkeley

Professor Van P. Carey, Chair

The film rupture process that dictates merging of adjacent bubbles is particularly important in nucleate boiling heat transfer, bubbly two-phase flow in small tubes, and the mechanisms that dictate the Leidenfrost transition. To understand the mechanisms of bubble merging in nano-structured boiling surfaces and in nanotubes, it is useful to explore film stability and onset of rupture at the molecular level. This dissertation reports the results of such an investigation combining three strategies that includes a new formulation of capillarity theory for free liquid films, molecular dynamics (MD) simulations using similar interaction potentials and bubble merging experiments. Two forms of our molecular film capillarity theory are developed here: one for non-polar fluids based on a Lennard-Jones interaction potential, and a second specifically for water using a modified treatment of the SPC/E interaction potential that accounts for water dipole interactions. The capillarity theory provides theoretical relationships among parameters that govern film structure and thermophysical behavior, while the companion MD simulations allow more detailed molecular level exploration of the film thermophysics. Results obtained with theoretical models and MD simulation studies indicate that the wave instability and the lack of thermodynamics intrinsic stability can lead to rupture of the liquid film, as its thickness decreases below a critical value. It is further predicted that wave instability predominates as an onset of rupture mechanism for liquid films of macroscopic extent, but for free liquid films with nanoscale lateral extent (in, for example, nanostructured boiling surfaces), lack of core stability is more likely to be the mechanism. For electrolyte aqueous solutions, theoretical models and MD simulation studies suggest that dissolved salts tend to alter the surface tension at liquid vapor interfaces and affect the stability of the free liquid film between adjacent bubbles. Bubble merging experiments are designed and carried out for various electrolyte aqueous solutions. The interaction of pairs of bubbles injected into solution with different dissolved salt concentrations is studied experimentally to determine the probability of merging from statistics for ensembles of bubble pairs. The results of these experiments indicate that for some types of salts, very low dissolved salt concentrations can strongly reduce the tendency of adjacent bubbles to merge, implying that the presence of the dissolved salt in such cases strongly enhances the stability of the free liquid film between adjacent bubbles. The trends are compared to predictions of free liquid film stability by wave instability theory and MD simulations.

TABLE OF CONTENTS

List of Figures……..…. iii

List of Tables……...…. viii

List of Symbols……..… ix

Chapter 1 – Introduction…… 1

§1.1 – Wave instability model studies on film stability…… 1

§1.2 – Redlich-Kwong model studies on the interfacial region…… 3

§1.3 – Molecular dynamics studies on the interfacial region…… 9

§1.4 – The effect of electrolyte on its aqueous solution properties…… 10

§1.5 – Overview of this report…… 15

Chapter 2 – Film capillarity theory for free liquid films…… 17

§2.1 – Partition function…… 17

§2.2 – Interfacial volumetric free energy…… 27

§2.3 – Determination of density profiles…… 31

§2.4 – Comparison of thick half film with a single interface…… 35

§2.5 – Exploration of intrinsic stability…… 37

§2.6 – Surface tension deviation…… 47

§2.7 – Effect of temperature on critical thickness and surface tension…… 49

§2.8 – Modified wave instability model…… 51

§2.9 – Summary…… 55

Chapter 3 – MD simulation techniques and implementations…… 57

§3.1 – Position initialization…… 57

§3.2 – Velocity initialization…… 64

§3.3 – Periodic boundary condition…… 67

§3.4 – Potential functions…… 68

§3.5 – Advancing algorithms and simulation stages…… 75

§3.6 – Thermodynamic properties calculation…… 82

§3.7 – Summary…… 87

Chapter 4 – Stability analysis by MD simulations…… 89

§4.1 – Density profiles and critical thickness…… 89

§4.2 – Critical thickness variation…… 97

§4.3 – Surface tension…… 101

§4.4 – Surface tension deviation for thinning films…… 106

§4.5 – Summary…… 108

Chapter 5 – Experiment and comparison…… 109

§5.1 – Experiment apparatus and procedure…… 109

§5.2 – Experiment results and interpretation…… 111

§5.3 – Comparisons among theoretical model analysis, MD simulations and experiments…… 114

§5.4 – Summary…… 120

Chapter 6 – Conclusions…… 121

References…… 123

LIST OF FIGURES

Chapter 1

Figure 1.1	A perturbing wave on a free liquid film in Scheludko's model	2
Figure 1.2	System configuration of a single vapor-liquid interfacial region in Carey's work [14]	4
Figure 1.3	Pair relative position in interfacial region	5
Figure 1.4	Reduced density profiles across the interfacial region at various reduced temperatures	8
Figure 1.5a	Effects of 1:1 electrolyte concentration on the change in surface tension relative to water reported by Weissenborn and Pugh [30]	11
Figure 1.5b	Effect of electrolyte concentration on the change in surface tension relative to water for electrolytes containing multivalent ions. Reported by Weissenborn and Pugh [30]	12
Figure 1.6a	Surface tension of NaCl aqueous solution at constant temperatures [33]	13
Figure 1.6b	Surface tension of NaCl aqueous solution at constant concentrations [33]	13
Figure 1.7	Bubble merging experiments for NaCl aqueous solution at room temperature by Aguilera [37] and Liendo [38]	15
Figure 1.8	System configuration of free liquid film bounded by its vapor on both sides	16

Chapter 2

Figure 2.1	The extended simple point charge (SPC/E) model for water molecule	20
Figure 2.2	Relative positions of two water molecules in Cartesian coordinate system	22
Figure 2.3	Variation of volumetric free energy with molar density	29
Figure 2.4	Comparison of $\sigma/(P_c L_i)$ for water among this study, Carey's model [14] and NIST data [41]	37

Figure 2.5 Variation of $\hat{\rho}_{cl}$ with $\delta_{ml} = \hat{n}"/\hat{\rho}_l$ for argon at $T_r = 0.6$ predicted by Equation 2.55 38

Figure 2.6 Density profile for argon at $T_r = 0.6$, $\delta_{ml} = 3.44$ nm 39

Figure 2.7 Density profile for argon at $T_r = 0.6$, $\delta_{ml} = 1.15$ nm 39

Figure 2.8 Density profile for argon at $T_r = 0.6$, $\delta_{ml} = 1.05$ nm (conditions resulting in incipient loss of film core stability) 40

Figure 2.9 Density profile for argon at $T_r = 0.6$, $\delta_{ml} = 0.57$ nm (conditions resulting in ruptured film) 40

Figure 2.10 Variation of $\hat{\rho}_{cl}$ with $\delta_{ml} = \hat{n}"/\hat{\rho}_l$ for water at $T_r = 0.6$ predicted by Equation 2.55 44

Figure 2.11 Density profile for water at $T_r = 0.6$, $\delta_{ml} = 3.38$ nm 45

Figure 2.12 Density profile for water at $T_r = 0.6$, $\delta_{ml} = 1.13$ nm 45

Figure 2.13 Density profile for water at $T_r = 0.6$, $\delta_{ml} = 1.01$ nm (conditions resulting in incipient loss of film core stability) 46

Figure 2.14 Density profile for water at $T_r = 0.6$, $\delta_{ml} = 0.56$ nm (conditions resulting in ruptured film) 46

Figure 2.15 Variation of the half-interface free energy with film thickness at $T_r = 0.6$ 48

Figure 2.16 Variation of critical thickness δ_c with reduced temperature T_r for argon and water 50

Figure 2.17 The transition lateral film dimension L_{tran} for argon at $T_r = 0.6$ 53

Figure 2.18 The transition lateral film dimension L_{tran} for water at $T_r = 0.6$ 53

Figure 2.19 Variation of the transition lateral film dimension L_{tran} with reduced temperature T_r 55

Chapter 3

Figure 3.1 System illustration of liquid film bounded by its vapor on both sides 57

Figure 3.2 Face-centered-cubic (f.c.c) lattice structure used in the initial configuration 58

Figure 3.3 The initial configuration of argon MD simulation at $T_r = 0.6$ with 1188 molecules 60

Figure 3.4 The local molecular coordinate frame with the molecular center of mass at origin 61

Figure 3.5 3-1-3 Euler's angle orientation of molecules using angles α_1, α_2 and α_3 62

Figure 3.6 The initial configuration of water MD simulation at $T_r = 0.65$ with 736 molecules 63

Figure 3.7 F.c.c lattice structure with a solute ion in its body center 63

Figure 3.8 The initial configuration of 0.75 M NaCl MD simulation at $T_r = 0.6$. Green particles represent Na^+ ions and yellow particles represent Cl^- ions. 64

Figure 3.9 The flow chart used to determine the rotational kinetic energy of polyatomic molecule 66

Figure 3.10 Schematic for periodic boundary condition 67

Figure 3.11 The flow chart of the velocity Verlet algorithm. Subscript i represents each monatomic molecule or ion in the simulation 76

Figure 3.12 The flow chart of the RATTLE algorithm. Subscript i represents a molecule, a and b represent atoms in the molecule, and ϵ_{tol} is the specified tolerance 78

Figure 3.13 Schematic of various simulation stages 79

Figure 3.14 Surface tension and statistical temperature variations with time steps for a MD simulation (0.36 M NaCl aqueous solution with $n_{z,l} = 4$ at $T_r = 0.65$) reaching equilibrium 80

Figure 3.15 Density and ion concentration data collection bins in the simulation domain 83

Figure 3.16 Determination of f_{ijk} for local pressure calculation 85

Chapter 4

Figure 4.1 Time-averaged density profiles predicted by MD simulations for argon at $T_r = 0.6$ 90

Figure 4.2 Time-averaged density profiles predicted by MD simulations for pure water at $T_r = 0.6$ 90

Figure 4.3	Time-averaged density profiles predicted by MD simulations for 0.38 M NaCl aqueous solution at $T_r = 0.6$	91
Figure 4.4	Variations of $\overline{\rho_{cc}}$ with δ_f for argon at $T_r = 0.6$	93
Figure 4.5	Variations of $\overline{\rho_{cc}}$ with δ_f for pure water at $T_r = 0.6$	93
Figure 4.6	Variations of $\overline{\rho_{cc}}$ with δ_f for 0.38 M NaCl aqueous solution at $T_r = 0.6$	94
Figure 4.7	Snapshots of molecules in MD simulations of argon: (a) $\overline{\rho_{cc}} < \rho_{spinodal,l}$ (b) $\overline{\rho_{cc}} > \rho_{spinodal,l}$	95
Figure 4.8	Snapshots of molecules in MD simulations of water: (a) $\overline{\rho_{cc}} < \rho_{spinodal,l}$ (b) $\overline{\rho_{cc}} > \rho_{spinodal,l}$	96
Figure 4.9	Snapshots of molecules and ions in MD simulations of 0.38 M NaCl aqueous solutions: (a) $\overline{\rho_{cc}} < \rho_{spinodal,l}$ (b) $\overline{\rho_{cc}} > \rho_{spinodal,l}$	97
Figure 4.10	Critical thickness variations with reduced system temperature predicted by MD simulations for argon	98
Figure 4.11	Critical thickness variations with reduced system temperature predicted by MD simulations for pure water	99
Figure 4.12	Critical thickness variations with reduced system temperature predicted by MD simulations for 0.38 M NaCl aqueous solution	99
Figure 4.13	Critical thickness variations with electrolyte solute concentration predicted by MD simulations for NaCl aqueous solution at five reduced temperatures	100
Figure 4.14	Variations of surface tension with reduce temperatures for system of argon	102
Figure 4.15	Variations of surface tension with reduce temperatures for system of water	103
Figure 4.16	Effect of ionic solute concentration on the change in surface tension relative to water (experimental data are from Weissenborn and Pugh [30], Abramzon and Gaukhberg [31], and Svenningsson, *et al.* [32]).	104
Figure 4.17	Ion concentration profile and density profile for the 1.88M NaCl aqueous solution simulation with film with $\delta_{ml} = 2.47$ nm at $T_r = 0.46$.	105
Figure 4.18	Surface tension variations with film thickness δ_f for pure water predicted by MD simulations at $T_r = 0.6$	106

Chapter 5

Figure 5.1 The schematic diagram of the experimental apparatus 110

Figure 5.2 Typical behaviors of bubbles in experiments: (a) formation of pairs of bubbles, (b) merged bubble in pure water or $NaClO_4$ solutions, (b) separate bubbles in other electrolyte aqueous solution. 111

Figure 5.3 Comparison of bubble merging experiment results for NaCl aqueous solutions. Experiment results reported by other researchers include: Lessard [36], Aguilera [37] and Craig [75] 112

Figure 5.4 Comparison of bubble merging experiment results for $CaCl_2$ aqueous solutions. Experiment results reported by the other researcher are from Craig [75] 113

Figure 5.5 Illustration of the relationship between the bubble merging probability and critical thickness 114

Figure 5.6 Critical thickness variations with reduced temperature predicted by the film capillarity intrinsic stability model, MD simulations, and wave instability models for the lateral dimension of the simulations ($L = 3.83$ nm) for argon 115

Figure 5.7 Critical thickness variations with reduced temperature predicted by the film capillarity intrinsic stability model, MD simulations, and wave instability models for the lateral dimension of the simulations ($L = 2.48$ nm) for water 116

Figure 5.8 Critical thickness variations with NaCl solute concentrations predicted by wave instability models and MD simulations are compared with bubble merging probability variation from experiments 117

Figure 5.9 Critical thickness variations with NaI solute concentrations predicted by wave instability models and MD simulations are compared with bubble merging probability variation from experiments 118

Figure 5.10 Critical thickness variations with $NaClO_4$ solute concentrations predicted by wave instability models and MD simulations are compared with bubble merging probability variation from experiments 118

Figure 5.11 Critical thickness variations with $CaCl_2$ solute concentrations predicted by wave instability models and MD simulations are compared with bubble merging probability variation from experiments 119

LIST OF TABLES

Table 2.1	Reduced saturation liquid and vapor densities based on the Redlich-Kwong model [14]	19
Table 2.2	Properties and constants used for the partition function of argon	19
Table 2.3	Properties and constants used for the partition function of water	21
Table 2.4	Calculated results for argon at $T_r = 0.6$ for four typical δ_{ml} values	43
Table 2.5	Calculated results for water at $T_r = 0.6$ for four typical δ_{ml} values	47
Table 2.6	Surface tension deviation correlation constants at various reduced temperatures	51
Table 3.1	Constants of SPC/E form potential functions used in MD simulations for water and ions	71
Table 4.1	Surface tension deviation correlation constants for NaCl, NaI, $NaClO_4$ and $CaCl_2$ aqueous solutions at room temperature of 25°C.	107
Table 5.1	The bubble merging probability P_m for NaCl, NaI, NaClO4 and CaCl2 aqueous solutions with various concentrations at room temperature of 25 °C.	112

LIST OF SYMBOLS

A_H	Hamaker constant	N_A	Avogadro constant
a_{R0}	Redlich-Kwong equation of state constant	n_{cut}	Fourier cutoff number
b_R	Redlich-Kwong equation of state constant	n_v, n_l	Refractive index for vapor and liquid
C	Concentration	P	Pressure
$\vec{d}$	Dipole moment	q	Point charge
F	Helmholtz free energy	R	Universal gas constant
$\vec{F}$	Force	R_M	Rotation matrix
G	Gibbs free energy	r	Separation
h	Planck constant	r_{cut}	Cutoff radius
I	Moment of inertia	r_{lj}	Lennard-Jones potential length parameter
$\vec{k}$	Reciprocal lattice vector	r_T	Tolman length
k_B	Boltzmann constant	T	Temperature
k_{cut}	Magnitude of cutoff vector	U	System total potential
L	Lateral film size	V	Volume
L_b	Bond length	v	Velocity
$L_{lattice}$	Dimension of MD lattice cell	Γ	Surface excess mass
L_{tran}	Transitional lateral size	δ	Film thickness
M	Mass	δ_c	Critical film thickness
N	Number of particles	δ_f	Mean density film thickness
δ_i	Interfacial region thickness	ϕ	Molecular interaction potential

δ_{is}	Intra-spinodal sublayer thickness	φ	Electric field
δ_{ml}	Film molar loading thickness	ψ	Free energy per unit volume
δ_{th}	Threshold film thickness of surface tension deviation	ψ_e	Excess volumetric free energy
δ_{sep}	Thickness of separating film	Ω	Euler's angles
ϵ_0	Vacuum permittivity	ω	Rotational velocity
$\epsilon_{dielectric}$	Dielectric constant		
ϵ_{lj}	Lennard-Jones potential energy parameter	**Subscript**	
ϵ_{rot}	Rotational kinetic energy	a, b	Specified atoms in molecules
ζ	Number of degrees of freedom	c	Critical property
$\theta_{rot,m}$	Mean molecular rotational temperature	i, j	Molecules
κ_w	Shielding charge width	r	Reduced property
μ	Chemical potential	α, β	Ions
ν_e	Electronic absorption frequency		
ρ	Density	**Superscript**	
$\hat{\rho}$	Molar density	f	Fourier space
$\overline{\rho_{cc}}$	Mean density within the central core region	m	Intra-molecular component
ρ_{cl}	Local density at the centerline	r	Real space
σ	Surface tension	s	Self-interacting term
σ_s	Symmetry number		
τ	Time step		
Φ	Total potential energy		

CHAPTER 1 – INTRODUCTION

§ 1.1 WAVE INSTABILITY MODEL STUDIES ON FILM STABILITY

The stability of thin free liquid films has been explored in a number of earlier investigations. These studies were motivated by the importance of film rupture as a mechanism in coalescence of bubbles during boiling, bubble merging in two-phase flow, and collapse of foams. Here we are particularly interested in these phenomena in nano-structured boiling surfaces and in nano-channel two-phase flow where the lateral extent of the interface is small. Most of the earliest investigations of free liquid film stability developed a model analysis that focuses on the fluid dynamics and/or thermodynamics of the wave motion at the film interfaces. Typical of these investigations are the early studies of Squire [1] and Hagerty and Shea [2], which focus on the fluid dynamics of wave motion, and the studies of Scheludko [3], Vrij [4], Vrij and Overbeek [5], and Donner and Vrij [6] which emphasize thermodynamics and the effect of the free energy change associated with wave motion.

The circumstance of interest here is a free liquid film that is progressively thinned by bubble growth, bubble motion or drainage of the liquid film between bubbles due to capillary effects or gravity. The key issue is determination of the conditions under which the film will rupture. These earlier studies indicate that in systems of this type, a range of wavelengths are generally amplified, and the analysis is used to determine the ‘‘most dangerous” wavelength that grows in amplitude A most rapidly [7]. Usually a timescale τ of interest is dictated by the nature of the application, and a critical film thickness δ_c can be determined by multiplying half the maximum growth rate by the timescale: $\delta_c = 0.5(dA/dt)_{max}\tau$. The critical thickness thus defined is the film thickness at which the wave amplitude grows to the point of film rupture ($A = 0.5\delta_c$) in the characteristic time τ. In more recent investigations, the wave perturbation theory was further developed by Radoev, et al. [8] and Manev et al. [9]. These investigations examine the establishment of conditions necessary to wave amplitude growth, and the rate of subsequent growth as factors that impact stability and rupture.

As shown in Figure 1.1, in Scheludko’s [3] model of wave instability, two opposite effects of perturbing waves on system free energy are postulated: an increase in free energy ΔF_s due to the increase in interface surface area, and a decrease in free energy ΔF_v due to the decrease in volumetric energy:

$$\Delta F_s = \frac{2\sigma(\pi A)^2}{\lambda} \tag{1.1}$$

$$\Delta F_v = -\lambda A^2 \frac{A_H}{2\pi\delta^4} \tag{1.2}$$

where A and λ are the amplitude and the wavelength of the perturbing wave, respectively, A_H is the Hamaker constant. Since for a stable system, the total system free energy change should be positive, by setting $\Delta F_s + \Delta F_v = 0$, Scheludko [3] obtained the following expression for the critical thickness δ_c:

$$\delta_c = \left(\frac{A_H \lambda^2}{4\pi^3 \sigma}\right)^{0.25} \tag{1.3}$$

with the interpretation that the film thickness δ has to be greater than δ_c for a film not to be ruptured spontaneously. The random disturbances in the film are presumed to be made up of Fourier wave components of virtually all wavelengths. Hence in a film of large lateral extent, it follows from this relation that for any thickness δ there will be a wavelength large enough to make the film unstable ($\delta_c > \delta$). This model therefore predicts that films of any thickness will eventually rupture.

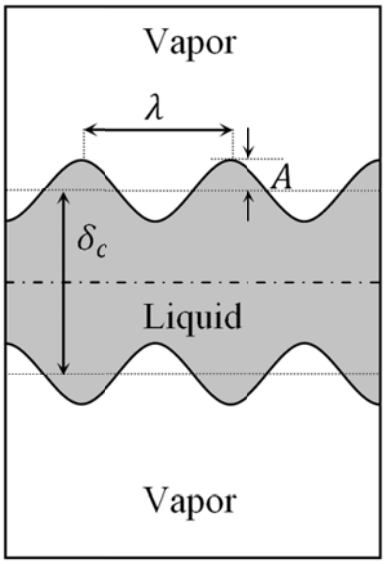

Figure 1.1 A perturbing wave on a free liquid film in Scheludko's model

As noted above, there are also circumstances of interest in which the lateral extent of the thin liquid film may be very small. Researchers are, for example, now fabricating nano-structured boiling surfaces in which bubbles may form in liquid-filled structure spaces with dimensions on the order of 10-50 nm [10, 11]. Liquid films separating bubbles during boiling in the structure will have a lateral extent on the order of about 10 nm. The thin liquid film between two adjacent bubbles in a nano-channel could also have a lateral extent on the order of about 10 nm. The model analysis developed by Vrij [4] can be applied to thin liquid films of limited lateral extent. Vrij [4] incorporated film thinning dynamics into Scheludko's model and applied certain simplifications in his study, such as only considering the perturbation components of wavelengths much greater than initial film thickness [7], assuming that the van der Waals interaction term predominates over the electrostatic repulsion term, etc. For the simple case of a stationary film, i.e. no draining in the liquid film, Vrij [4] proposed that the maximum perturbation wavelength is restricted by the lateral film size L, and therefore $\lambda_{max} = L$ can be substituted in Eq. (1.3) to get a quantitative way of calculating the critical thickness δ_c as

$$\delta_c = \left(\frac{A_H L^2}{4\pi^3 \sigma}\right)^{0.25} \tag{1.4}$$

Although wave instability has been the primary focus of efforts to predict conditions that result in film rupture, it has also been suggested that for ultra thin films, onset of rupture could result from hole formation due to thermal fluctuations in the film, or interaction of the interfacial regions in thin free liquid films. The analysis of De Vries [12] indicated that for common fluids, the free energy of forming a hole which is big enough to breach the film would require a free energy increase so large that its spontaneous formation due to thermal fluctuations is very unlikely unless the film is extremely thin. For common fluids at temperatures near 300 K, the film thickness would have to be on the order of 2 nm for this sort of hole formation to be a likely event. As noted by Vrij [4] and Donner and Vrij [6], experimentally measured critical film thicknesses for film rupture are typically in the order of tens of nanometer, which suggests that hole formation is not the determining mechanism.

§ 1.2 REDLICH-KWONG MODEL STUDIES ON THE INTERFACIAL REGION

The wave perturbation model studies summarized above were based on the assumption that the vapor-liquid interfacial region between two phases can be simplified as a well-defined 2-D surface without thickness. This assumption is questionable when the critical thickness is comparable to the interfacial region thickness. In van de Waals theory of capillarity [13], it generally argued that a step change of density from one phase to another is less

thermodynamically favorable than a continuous change in an interfacial region between two phases. By incorporating the Redlich-Kwong fluid properties into the classical mean field van der Waals theory of capillarity, Carey [14] proposed a Redlich-Kwong capillarity model to predict the thermodynamic properties and structure of the vapor-liquid interfacial region. In his work [14], a system of a single vapor-liquid interfacial region is studied as shown in Figure 1.2.

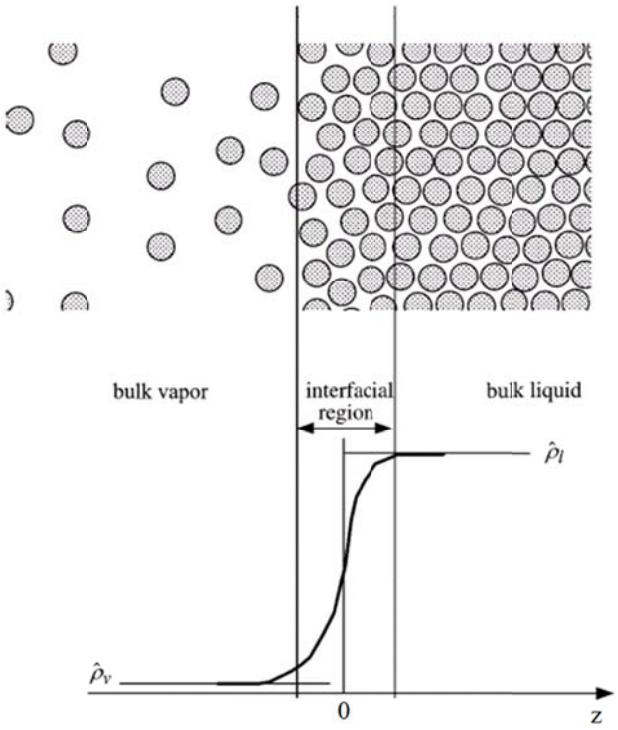

Figure 1.2 System configuration of a single vapor-liquid interfacial region in Carey's work [14]

The intermolecular potential energy interaction is computed using Rayleigh's method. As shown in Figure 1.3, for a molecule at an arbitrary z location, the mean energy per molecule is computed by summing the potential energy interaction with all the surrounding molecules and dividing by 2 to assign half the energy to each molecule in the pair. This is represented as

$$\frac{\Phi(z)}{N} = \frac{1}{2}\int \rho(z)\phi \, dV \tag{1.5}$$

where ϕ is the radially symmetric molecular interaction potential, and Φ/N is the mean energy per molecule at a location z in the interfacial region.

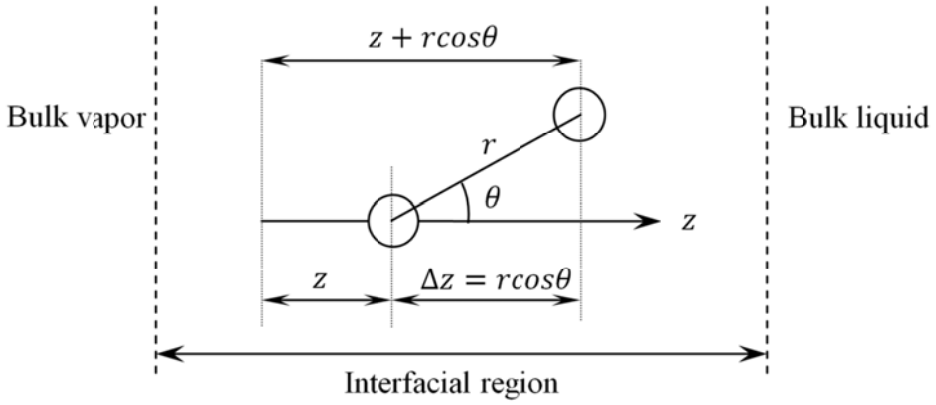

Figure 1.3 Pair relative position in interfacial region

By considering a donut-shaped differential volume dV around the z axis, $dV = 2\pi r^2 sin\theta d\theta dr$, the integral of Equation 1.5 can be implemented over the entire system, from an average minimum separation of closest molecules r_{min} to a maximum separation distance r_{max} representing the effective range of the long-range attraction forces between molecules. The resulting volumetric integral can be cast in the form:

$$\frac{\Phi(z)}{N} = \pi \int_{r_{min}}^{r_{max}} \phi(r) r^2 \int_0^{\pi} \rho(rcos\theta + z) sin\theta d\theta dr \tag{1.6}$$

Expanding $\rho(rcos\theta + z)$ about a specific z value for small $rcos\theta$, and substituting it into Equation 1.6, the integration with respect to θ yields:

$$\frac{\Phi(z)}{N} = \frac{2\pi N}{V} \int_{r_{min}}^{r_{max}} \phi(r) r^2 dr + \frac{\pi}{3} \rho"(z) \int_{r_{min}}^{r_{max}} \phi(r) r^4 dr \tag{1.7}$$

As shown by Carey [15], for a system of uniform density, the classical Redlich-Kwong equation of state amounts to postulating that:

$$-2\pi \int_{r_{min}}^{r_{max}} \phi(r) r^2 dr = a_{R0}\gamma_0(T)\eta_0\left(\frac{V}{N}\right) \tag{1.8}$$

in which, $\gamma_0(T)$ and $\eta_0(V/N)$ are of the forms:

$$\gamma_0(T) = T^{-\frac{1}{2}} \tag{1.9}$$

$$\eta_0\left(\frac{V}{N}\right) = \frac{V}{Nb_R}\ln\left(\frac{V+Nb_R}{V}\right) \tag{1.10}$$

a_{R0} and b_R are the constants of Redlich-Kwong equation of states for a fluid of uniform density.

Consistent with this approach, Carey [14] similarly postulated that:

$$-\frac{2\pi}{3} \int_{r_{min}}^{r_{max}} \phi(r) r^4 dr = a_{R1}\gamma_1(T)\eta_1\left(\frac{V}{N}\right) \tag{1.11}$$

Substituting Equation 1.8 and Equation 1.11 into Equation 1.7 yields:

$$\Phi(z) = -a_{R0}\gamma_0(T)\eta_0\left(\frac{V}{N}\right)\frac{N^2}{V} - \frac{1}{2}a_{R1}\gamma_1(T)\eta_1\left(\frac{V}{N}\right)N\rho"(z) \tag{1.12}$$

The above given relation for $\Phi(z)$ can be used to obtain the natural log of the canonical partition function as:

$$\ln Q = N + \left(\frac{3N}{2}\right)\ln\left[\frac{2\pi M k_B T(V - Nb_R)^{2/3}}{N^{2/3}h^2}\right] + N\left[\frac{\xi - 5}{2}\ln\pi - \ln\sigma_s\right] + \frac{(\xi - 3)N}{2}\ln\left(\frac{T}{\theta_{rot,m}}\right) + \frac{a_{R0}N}{b_R k_B T^{3/2}}\ln\left(\frac{V + Nb_R}{V}\right) + \frac{a_{R0}\kappa V\rho"(z)}{2b_R k_B T^{3/2}}\ln\left(\frac{V + Nb_R}{V}\right) \tag{1.13}$$

where M is the molecular mass of the molecule, k_B is the Boltzmann constant, h is Planck's constant, ξ is the number of translational and rotational storage modes, σ_s is the symmetry number for the molecule, $\theta_{rot,m}$ is the mean rotational temperature for the molecule if it is a polyatomic species, and κ , which arises due to the non-uniform density distribution, is defined as:

$$\kappa = \frac{a_{R1}\gamma_1\eta_1}{a_{R0}\gamma_0\eta_0} = \frac{-\frac{2\pi}{3}\int_{r_{min}}^{r_{max}}\phi(r)r^4dr}{-2\pi\int_{r_{min}}^{r_{max}}\phi(r)r^2dr} \tag{1.14}$$

Using the partition function from Equation 1.13, Carey [14] defined the free energy per unit volume ψ as:

$$\psi = \frac{F}{V} = \frac{-k_B T\ln Q}{V} \tag{1.15}$$

in which, F is the Helmholtz free energy. The interfacial free energy σ is the system excess free energy (per unit area of interface) above that for a step changes in density $\hat{\rho}$ at the interface at $z = 0$ (as shown in Figure 1.2):

$$\sigma = \int_{-\infty}^{0}[\psi - \psi(\hat{\rho}_v)]dz + \int_{0}^{\infty}[\psi - \psi(\hat{\rho}_l)]dz \tag{1.16}$$

here, $\hat{\rho}_v$ and $\hat{\rho}_l$ are the molar densities of the bulk vapor and bulk liquid phases respectively. By substituting Equations 1.13 and 1.15 into Equation 1.16, the interfacial free energy σ is

expressed as a functional, i.e. a function of a function, which maps the density function $\hat{\rho}(z)$ into the value of σ as a real number. Based on thermodynamics arguments, the equilibrium density function $\hat{\rho}(z)$ is that which minimizes the interfacial free energy σ. In his work, Carey [14] assumed Lennard-Jones 12-6 potential model for $\phi(r)$:

$$\phi(r) = 4\epsilon_{lj}\left[\left(\frac{r_{lj}}{r}\right)^{12} - \left(\frac{r_{lj}}{r}\right)^{6}\right] \tag{1.17}$$

where, ϵ_{lj} and r_{lj} are the energy and length parameters of the potential. By transforming equations into their reduced forms with respect to fluid critical properties and applying the Calculus of Variations [16] to this problem, Carey was able to solve the equilibrium density profiles $\hat{\rho}(z)$ across the interfacial region between bulk vapor and liquid phases. Shown in Figure 1.4 are reduced density profiles at various reduced temperatures, in which $L_i = [k_B T_c/P_c]^{1/3}$ is used as a non-dimensionalization factor for length parameters.

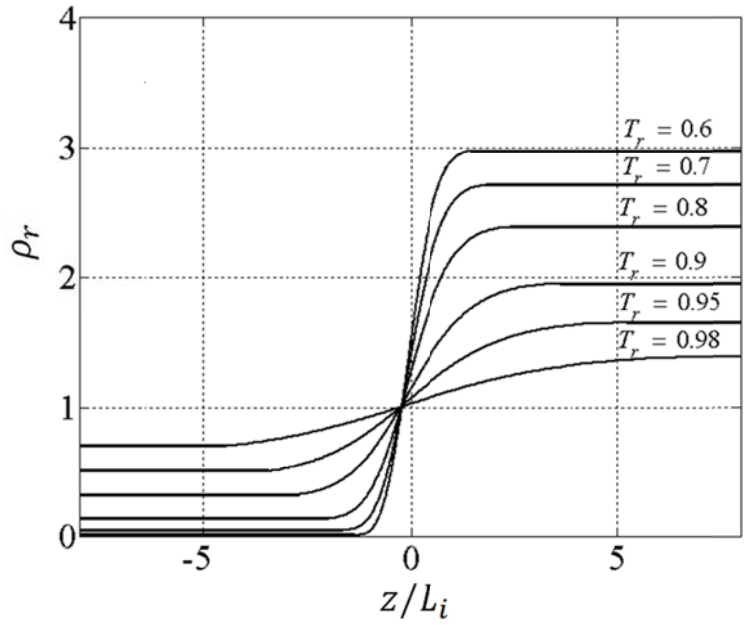

Figure 1.4 Reduced density profiles across the interfacial region at various reduced temperatures; L_i is the non-dimensionalization factor for length parameters defined as: $L_i = [k_B T_c/P_c]^{1/3}$

The thickness of the interfacial region is found in the range from 1nm to 10 nm for various fluids at various system temperatures.

Also reported in Carey's work [14] is that within the interfacial region is a sublayer that lacks the intrinsic stability usually associated with a stable phase. Both the thickness of the interfacial region and the thickness of the unstable sublayer increase with the increase of system reduced temperature.

§ 1.3 MOLECULAR DYNAMICS STUDIES ON THE INTERFACIAL REGION

Besides the method of thermodynamics analysis, computer simulation method is also widely adopted in the research of interfacial region and film stability. By investigating the system on a "bottom-up" approach, computer simulations provide additional insight into the behaviors of molecules and their interactions within the interfacial region.

Monte Carlo (MC) and Molecular Dynamics (MD) are two major methods used for computer simulations. In MC simulations, a sequential series of proposed molecular configuration are accepted or rejected based on criteria related to the possible system potential energy change. In MD simulations, the molecular configuration is updated for each of a series of time steps based on the integration of Newton's second law. Although the MC simulation has the advantage in the ease of implementation, MD simulation is generally preferred since it provides a physically meaningful temporal evolution of the system.

A number of previous investigations have used MD simulations to explore the free liquid film structure and stability. Studies of this type have considered films of Lennard-Jones fluids [17, 18], argon [17, 19–22], nitrogen [21], water [18, 23-24], water and alcohol mixtures [25–27], hydrocarbons [28] and fluorocarbons [29]. Statistical analysis of MD simulation results appears to support Carey's study [14] by Redlich-Kwong capillarity model discussed above. It is reported that the core of the interfacial region exhibits high levels of property fluctuations and is at best weakly stable [20, 27]. As the thickness of a free liquid film diminishes, the stable core fluid separating the interfacial regions becomes thinner, which may strengthen the interaction between the interior sublayers in the interfacial regions that lack intrinsic stability. This suggests that the interaction of these subregions may be a precursor to film rupture.

Although significant work has recently been performed in MD simulations, many areas are left unexplored for the properties of vapor-liquid interfacial regions, such as the nature of the interaction between adjacent interfacial regions and its effects on thin film stability, the relationship of surface tension to the critical film thickness. Therefore, one of the major focuses in our research is to use MD simulations in tandem with extended film capillarity theory to explore the thermophysics of vapor-liquid interfacial regions and stability of free thin liquid films. A more detailed description about the MD simulations and simulation data analysis is presented in later sections.

§ 1.4 THE EFFECT OF ELECTROLYTE ON ITS AQUEOUS SOLUTION PROPERTIES

Among investigations of electrolytes in their aqueous solutions, two topics are especially important and tightly related with our research: the effect of electrolytes on surface tension of solutions and the influence of electrolytes on bubble coalescence.

Surface tension

Investigations of the surface tension of electrolytes aqueous solution have been reported in a number of literatures. The widely cited experimental results were reported by Weissenborn and Pugh [30], in which the surface tension of aqueous solutions of 36 inorganic electrolytes had been measured as a function of electrolyte concentration up to 1M (mol/l) at room temperature of 25 °C. Plots of these data are shown in Figure 1.5a and 1.5b for 1:1 electrolytes and electrolytes containing multivalent ions respectively. For higher concentration electrolyte aqueous solution, Abramzon and Gaukhberg [31], and Svenningsson *et al*. [32] reported their experimental measurement of surface tension at room temperature up to 5M. Matubayasi *et al*. [33] and Ikeda *et al.* [34] measured the surface tension of NaCl aqueous solution for various NaCl concentrations at different temperatures. Their experiment results suggested that the surface tension of NaCl aqueous solution increases with the increase of NaCl concentration and the decrease of temperature, as shown in Figure 1.6a and 1.6b respectively.

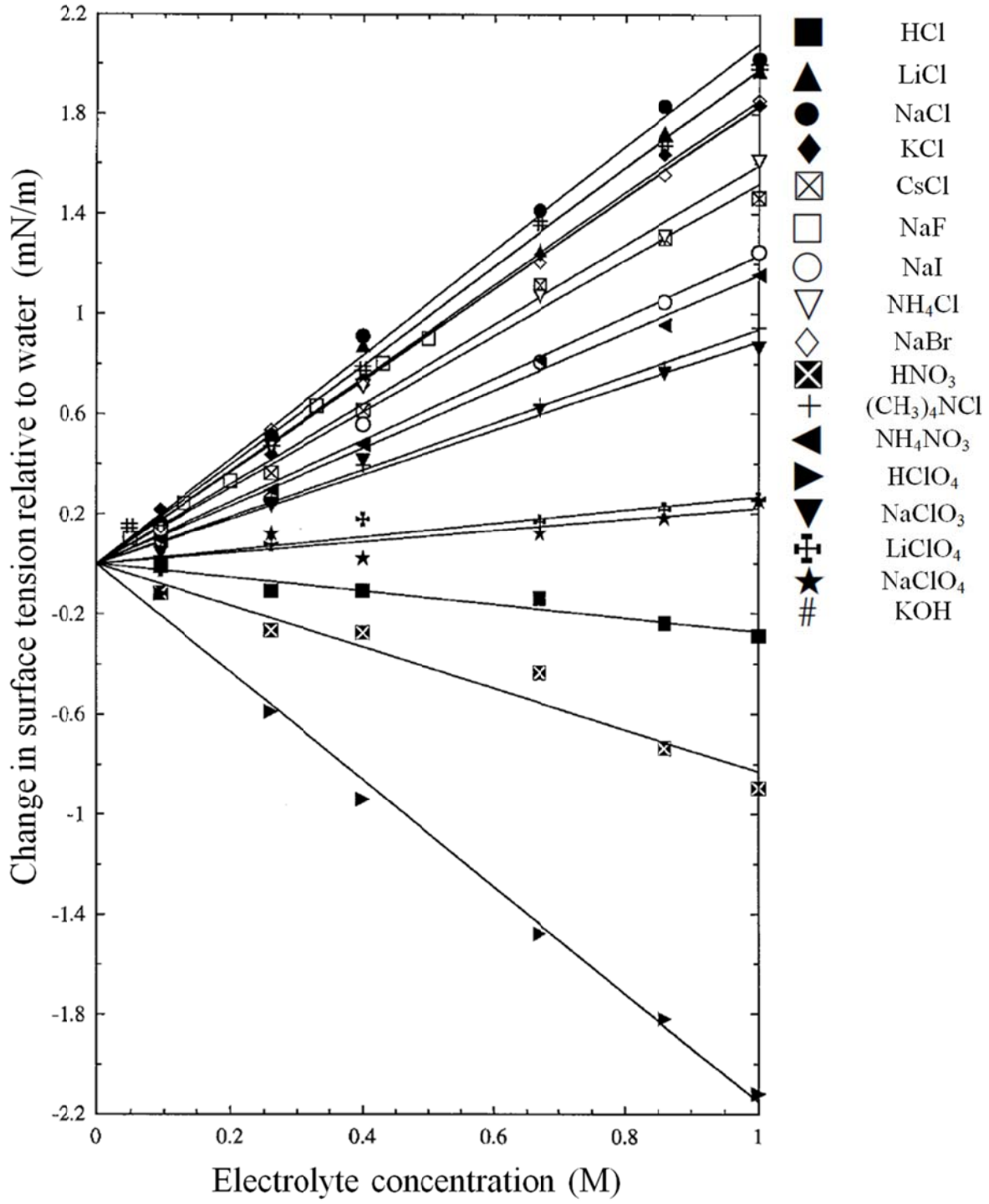

Figure 1.5a Effect of 1:1 electrolyte concentration on the change in surface tension relative to water reported by Weissenborn and Pugh [30]

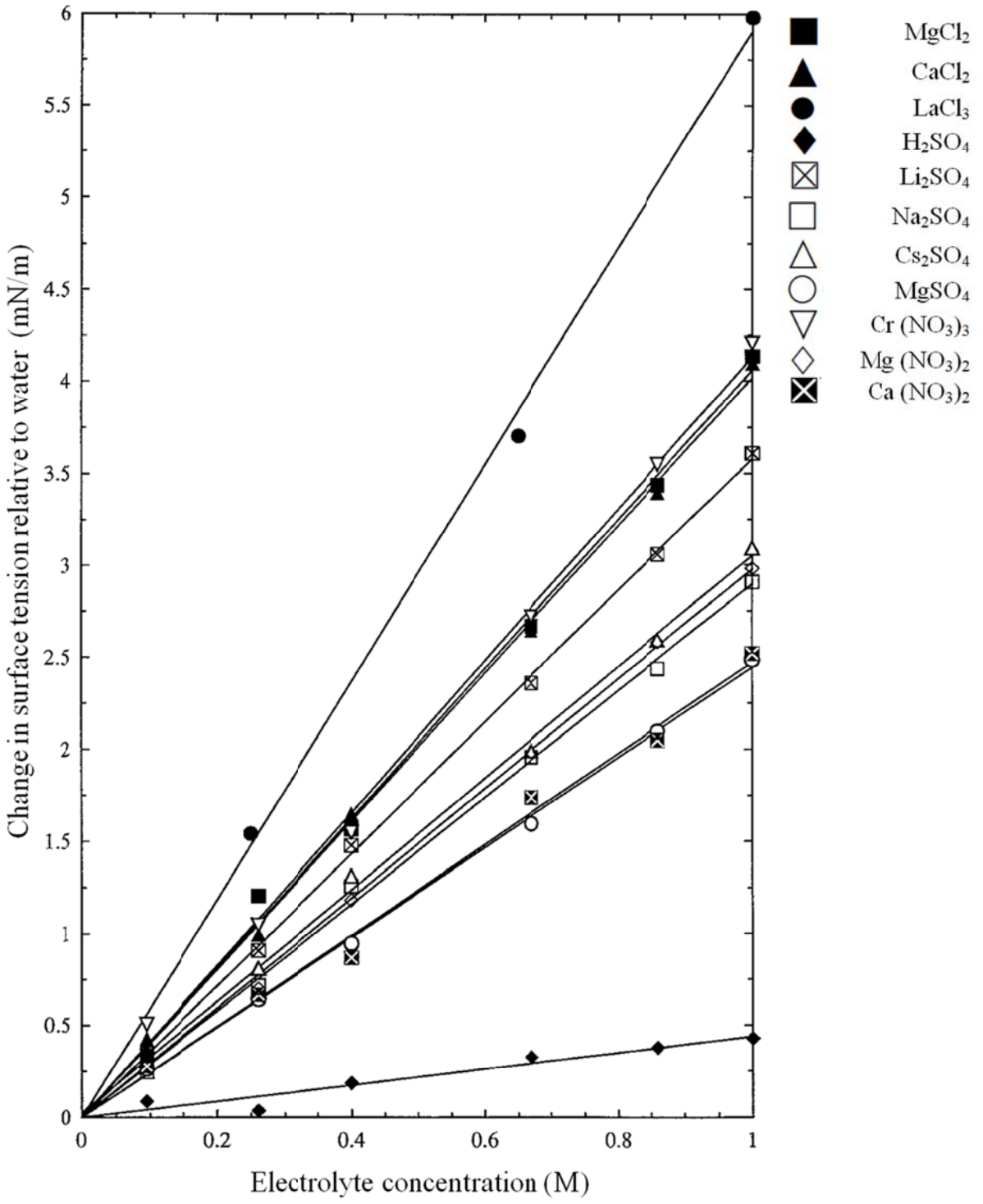

Figure 1.5b Effect of electrolyte concentration on the change in surface tension relative to water for electrolytes containing multivalent ions. Reported by Weissenborn and Pugh [30]

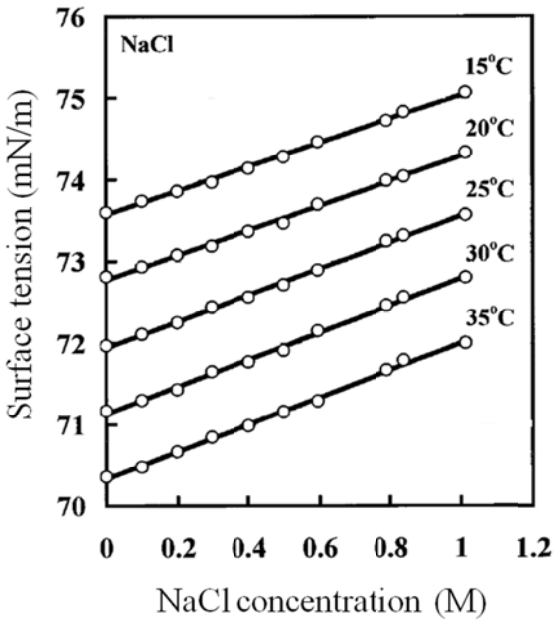

Figure 1.6a Surface tension of NaCl aqueous solution at constant temperatures [33]

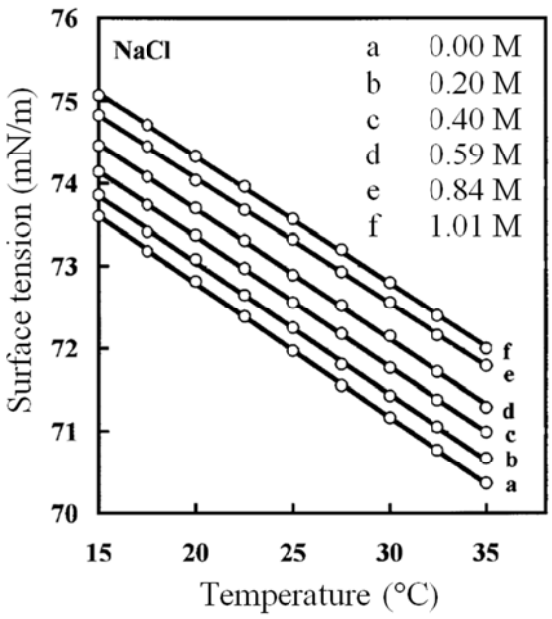

Figure 1.6b Surface tension of NaCl aqueous solution at constant concentrations [33]

Theoretical analysis by Gibbs [35] suggested that the change in surface tension of aqueous solutions upon the addition of electrolyte can be explained by the negative or positive adsorption of ions from the vapor-liquid interfacial region. Gibbs in his treatment of vapor-liquid interfaces did not explicitly address their internal structure. Instead, he introduced the notion of a dividing surface which separates the two bulk phases and accounts for the physical properties of the interface through defining excess quantities, such as the surface excess mass. In this treatment, he derived the well-known Gibbs adsorption equation:

$$\Gamma_A = -\left(\frac{C_A}{RT}\right)\left(\frac{\partial \sigma}{\partial C_A}\right)_T \tag{1.18}$$

In this equation, species A is an electrolyte solute that exhibits ideal mixture behavior in aqueous solution. Γ_A is the surface excess mass of species A, the excess of per unit area of the vapor-liquid interfacial region over what would be present if the concentration in the center core liquid region prevailed all the way through the interfacial region. C_A is the mean concentration of the electrolyte solute, R is the ideal gas constant, T is the system temperature, and σ is the surface tension. It can be seen from Equation 1.18 that if the surface tension σ increases as the electrolyte concentration C_A increases, $(\partial\sigma/\partial C_A)_T$ is positive and Γ_A is negative, meaning the repulsion or negative adsorption of ions from the vapor-liquid interfacial. This behavior of ion

distribution and its relation with the surface tension are examined in details in our study of MD simulations.

Bubble coalescence

Because the critical thickness of a free liquid film is generally in the order of nano-meters, direct experiment measurements of the critical thickness and its variation are hard to achieve without the help of complex optical and electronic auxiliary systems. An alternative experiment method to study the effect of the electrolyte concentrations on film stability is to observe the variation of the probabilities of bubble merging in different electrolyte aqueous solutions.

A bubble merging experiment platform normally consists of three parts: a container filled by electrolyte aqueous solution at specified concentrations; a mechanism generating bubbles in the solution with constant speed and bubble size; an observing system that helps count the percentage of bubble coalescence. It is reasonable to assume that the separations of bubbles, i.e. the thicknesses of the separating film between bubble pairs, distribute randomly within a relatively small range, given that the experiment conditions are fixed. Therefore, the extent of bubbling merging is a good indicator for the stability of separating films: a high probability of bubble merging means the low stability of the solution film, and vice verse.

In the experiment of Lessard and Zieminski [36], the percentage of bubble coalescence in pure water without the addition of electrolyte is 100%, and the coalescence percentage drops to 50% in 0.175M NaCl aqueous solution. At NaCl concentration of 0.25M, the coalescence percentage further reduces to 10%. They also reported three experiments on sea water at three temperatures, showing that with the increase of temperature from 6 °C to 31°C, the percentage of coalescence increase from 12% to 50%. Aguilera *et al* [37] reported similar experiments for NaCl aqueous solutions from 0.001M to 0.145M concentration at room temperature of 25 °C. Their experiment results show 100% coalescence percentage for pure water, 50% coalescence percentage in 0.1M NaCl aqueous solution, and 0% coalescence percentage in 0.145M NaCl aqueous solution. In Aguilera's work [37], they also cited the experiment results from Liendo [38] and compared with their own results, as shown in Figure 1.7.

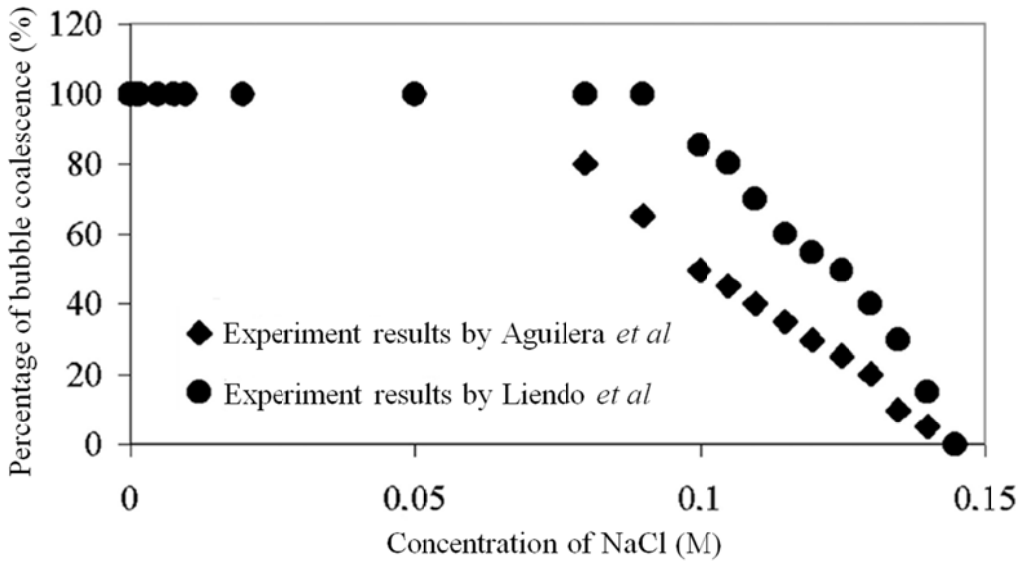

Figure 1.7 Bubble merging experiments for NaCl aqueous solution at room temperature by Aguilera [37] and Liendo [38]

§ 1.5 OVERVIEW OF THIS REPORT

The research described in this report specifically studied the free liquid film stability and the effects of system variables on stability, such as temperature, film size, and the addition of electrolytes. Three strategies are used in tandem in our investigation: new formulations of capillarity theory for free liquid films, MD simulations using similar interaction potentials and bubble merging experiments.

The single-interface molecular theory of capillarity is extended to a full free liquid film (see Figure 1.8). Using the resulting film capillarity theoretical model in tandem with MD simulations, we explore the thermophysics of vapor-liquid interfacial region and the stability of free liquid films. This hybrid approach has the advantage that the molecular capillarity theory, although limited in accuracy, provides explicit relations among the parameters that affect the film structure and stability, while the MD simulations allow more detailed exploration of film structure and stability without invoking the idealizations in the capillarity theory model. In addition, the film molecular capillarity theory developed in this study has two enhancements over conventional capillarity theory. The first is that it incorporates a Redlich–Kwong fluid property framework, which provides a better fit to saturation properties than the van der Waals properties used in classical capillarity theory. The second is that we have used a modified version of the SPC/E potential function model in the statistical thermodynamics property formulation for water to better account for its polar molecule effects. Bubble merging experiment method is used and experiment results are interpreted in a more explicit way to validate the conclusions reached

by our theoretical model and MD simulations. Three fluid systems will be examined in our investigation: argon, water, and electrolyte aqueous solutions. Argon is the simplest fluid to model and provides a basis for comparison of our theoretical framework and MD simulations; water and electrolyte aqueous solutions are studied because they are far more important than argon in current and potential engineering applications. The formulation of the hybrid analysis tools and their application to explore the structure and stability of free liquid films are described in the following chapters.

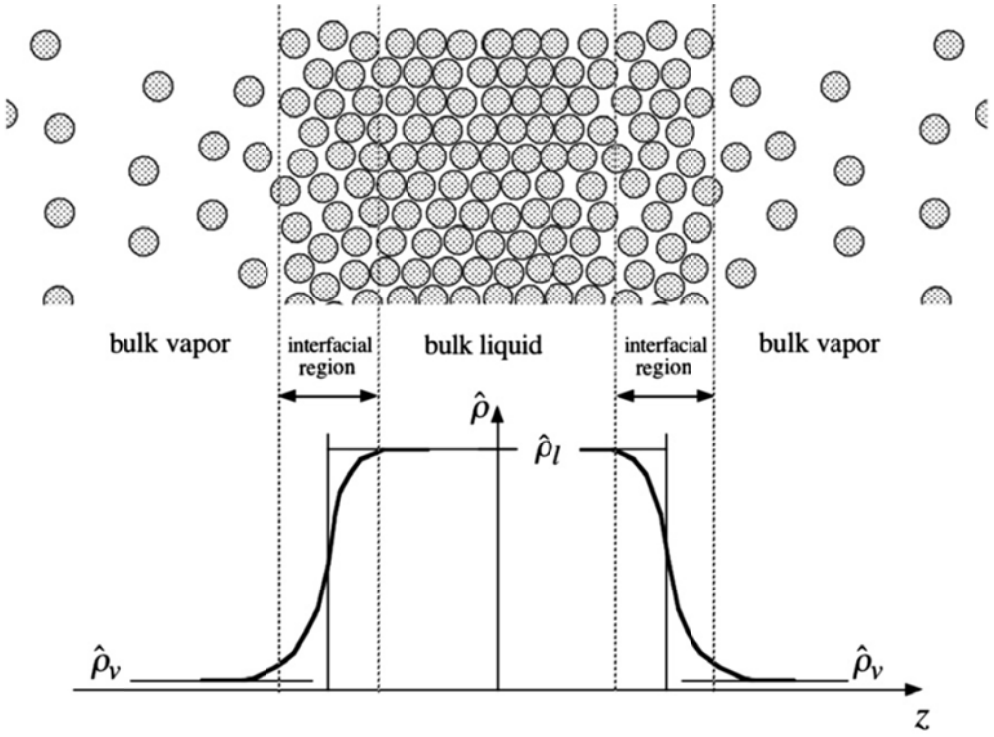

Figure 1.8 System configuration of free liquid film bounded by its vapor on both sides

Chapter 2 develops the film capillarity theoretical model based on Carey's work [14] of a single vapor-liquid interface system. Chapter 3 outlines the techniques used in our MD model construction and simulation implementations. Chapter 4 analyzes the MD simulation results for systems of argon, water and various electrolyte aqueous solutions. Film stability and the surface tension of liquid-vapor interfacial regions are examined in detail. Chapter 5 describes the setup of bubble merging experiments and compares the experiments results with those from theoretical analysis and MD simulations. Finally Chapter 6 summaries conclusions derived from this study.

CHAPTER 2 – FILM CAPILLARITY THEORY FOR FREE LIQUID FILMS

This chapter outlines the development of the film capillarity theoretical model based on Carey's work of a single vapor-liquid interface system. After deriving appropriate partition functions for the thermodynamics systems of argon and water, the interfacial free energy is expressed as a functional, mapping the density function into the interfacial free energy's value. The calculus of variation method is used to obtain the density profile that minimize the interfacial free energy, and based on the density profile derived, the critical thickness is determined using the intrinsic stability analysis. Surface tension variation with the film thickness is discussed, and its impact on film stability is examined.

§ 2.1 PARTITION FUNCTION

As mentioned previously in the introduction chapter, for a system containing a Redlich-Kwong fluid with spatially varying density, Carey [14] derived Equation 1.13 for the partition function. Given a specified fluid, most parameters in the partition function can be easily determined. $\rho"(z)$ in Equation 1.13 is the second derivative of the density variation along z-axis, which needs be solved by using Calculus of Variable method in the following sections, and the parameter κ arises due to the non-uniform density distribution, which can be evaluated by Equation 1.14 as the effective pair-wise intermolecular potential function $\phi(r)$ is provided.

Partition function for monatomic fluid – argon

To calculate κ for monatomic fluid argon, the Lennard-Jones 12-6 potential function (Equation 1.17) is adopted for $\phi(r)$. The upper integral limit r_{max} in Equation 1.14 is set to be ∞, and the lower limit r_{min} is chosen to be the mean separation of the closest molecules in a bulk saturated liquid phase. Modeling the liquid as a three-dimensional cubic array of molecules with nearest neighbors separated by a center-to-center distance of r_{min}, the relationship between the saturated liquid molar density $\hat{\rho}_l$ and r_{min} is:

$$r_{min} = (\hat{\rho}_l N_A)^{-\frac{1}{3}} \tag{2.1}$$

Substituting Equation 1.17 into Equation 1.14 with the two integral limits r_{max} and r_{min} defined above, after integration we obtain:

$$\kappa_{argon} = \frac{9a_a(\hat{\rho}_l N_A)^{\frac{7}{3}} - 63b_a(\hat{\rho}_l N_A)^{\frac{1}{3}}}{21a_a(\hat{\rho}_l N_A)^3 - 63b_a(\hat{\rho}_l N_A)} \tag{2.2}$$

where

$$a_a = 4\epsilon_{lj} r_{lj}^{12} \tag{2.3a}$$

$$b_a = 4\epsilon_{lj} r_{lj}^{6} \tag{2.3b}$$

To get the numerical value of κ_{argon} from Equation 2.2, $\hat{\rho}_l$ must be specified. The Redlich-Kwong fluid property model developed by Carey [14] is used to compute reduced bulk equilibrium properties for the saturated liquid and vapor phases. Resulting values for specific reduced temperatures ($T_r = T/T_c$) are listed in Table 2.1. Saturation densities are computed from these results and the critical constants: $\hat{\rho}_l = \rho_{r,liquid}\hat{\rho}_c$, and $\hat{\rho}_v = \rho_{r,vapor}\hat{\rho}_c$. At the critical point, the properties of argon should satisfy the Redlich-Kwong equation of state, the zero slope and inflection point conditions for isotherms on the $P - v$ diagram, which gives us:

$$P_c = \frac{RT_c}{\hat{v}_c - N_A b_R} - \frac{a_{R0}N_A^2}{T_c^{\frac{1}{2}}\hat{v}_c(\hat{v}_c + N_A b_R)} \tag{2.4a}$$

$$\left(\frac{\partial P}{\partial \hat{v}}\right)_{T_c} = 0 \tag{2.4b}$$

$$\left(\frac{\partial^2 P}{\partial \hat{v}^2}\right)_{T_c} = 0 \tag{2.4c}$$

The resulting three equations 2.4a – 2.4c are solved simultaneously at the experimentally determined T_c and P_c values for argon to obtain the numerical values of Redlich-Kwong

constants a_{R0}, b_R, and the critical density $\hat{\rho}_c$ in Table 2.2. After substituting κ_{argon} and other constants from Table 2.2 into Equation 1.13, the functional dependence of the partition function $\ln(Q)$ on temperature, local equilibrium properties, and the second derivative of the density profile $\rho"(z)$ is defined.

Table 2.1
Reduced saturation liquid and vapor densities based on the Redlich-Kwong model [14]

T_r	0.6	0.65	0.7	0.75	0.8	0.85	0.9
$\rho_{r,liquid}$	3.025	2.898	2.758	2.603	2.428	2.264	1.987
$\rho_{r,vapor}$	0.01172	0.02452	0.04559	0.07793	0.1256	0.1950	0.2980

Table 2.2
Properties and constants used for the partition function of argon

M (kg)	6.633×10^{-26}
ξ	3
σ_s	1
ϵ_{lj} (J)	1.670×10^{-21}
r_{lj} (m)	3.400×10^{-10}
P_c (Pa)	4.86×10^{6}
T_c (K)	150.69
$\hat{\rho}_c$ (mol/m^3)	11644.6
a_{R0} (JK$^{0.5}$m^3)	4.671×10^{-48}
b_R (m^3)	3.707×10^{-29}

Partition function for polyatomic fluid – water

Due to the dipole character of water, the Lennard-Jones 12-6 potential function is not a completely suitable model of molecular interactions for water. In this investigation, we therefore

used the extended simple point charge (SPC/E) potential function from Berendsen *et al.* [39] to provide more accurate predictions of the effects of interactions between water molecules. In the SPC/E potential, a water molecule features a rigid bond length $L_{b,OH}$, a fixed bond angle α_{HH}, and an electrostatic point charge on each atom as shown in Figure 2.1. The potential function $\phi_{i,j}$ between two water molecules i and j is modeled as consisting of two parts: a Lennard-Jones type potential ϕ_{lj}, Equation 2.6, and an electrostatic potential component ϕ_{el}, Equation 2.7, among all three atoms in molecules i and molecule j:

$$\phi_{i,j} = \phi_{lj} + \phi_{el} \tag{2.5}$$

$$\phi_{lj} = 4\epsilon_{spc/e}\left[\left(\frac{r_{spc/e}}{r_{OO}}\right)^{12} - \left(\frac{r_{spc/e}}{r_{OO}}\right)^{6}\right] \tag{2.6}$$

$$\phi_{el} = \frac{1}{4\pi\epsilon_0}\sum_{a=1}^{3}\sum_{b=1}^{3}\frac{q_a q_b}{r_{iabj}} \tag{2.7}$$

here, r_{OO} is the oxygen–oxygen separation between molecules i and molecule j, ϵ_0 is the vacuum permittivity, and q_a and q_b are point charges assigned on specified atoms. Values of these constants are listed in Table 2.3. It is noteworthy that the contribution of induced dipole–dipole interaction has been embedded in the SPC/E model by parameterizations of q_H and q_O [39].

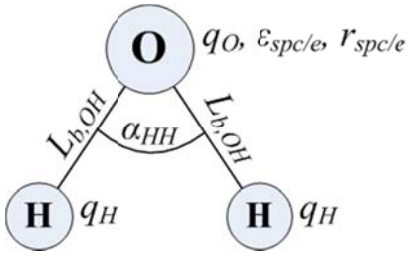

Figure 2.1 The extended simple point charge (SPC/E) model for water molecule

Table 2.3
Properties and constants used for the partition function of water

M (kg)	2.987×10^{-26}
$\theta_{rot,m}$ (K)	22.394
$L_{b,OH}$ (m)	1.00×10^{-10}
α_{HH} (°)	109.47
D_{water} (C·m)	-1.358×10^{-19}
ξ	6
σ_s	2
$\epsilon_{spc/e}$ (J)	1.080×10^{-21}
$r_{spc/e}$ (m)	3.166×10^{-10}
P_c (Pa)	2.218×10^{7}
T_c (K)	650.83
$\hat{\rho}_c$ (mol/m^3)	12296.8
a_{R0} (J·K$^{0.5}$·m^3)	39.7×10^{-48}
b_R (m^3)	3.51×10^{-29}

As shown in Equation 2.7, the electrostatic part of the potential ϕ_{el} requires specifying all nine separations r_{iabj}among all three atoms in molecules i and j. We therefore cannot directly substitute the potential into Equation 1.14 to calculate κ. To deal with this problem, a more suitable expression for ϕ_{el} is needed. Instead of using the columbic type of form in Equation 2.7, we consider ϕ_{el} as the potential energy of one molecule in a field generated by the second molecule. As is well-known from electrostatic theory [40], the field generated by a system of point charges, the second molecule in this case, may be represented as a series expanded in multi-pole moments. If the two molecules are at a separation distance greater than the dimensions of each molecule, the higher order terms which are of small magnitude in the expansion can be neglected, thus giving us a simplified expression of ϕ_{el} in terms of r_{OO} and Ω, the set of Euler's angles between the dipole moments of molecule i and molecule j . Because the molecules are not affected by any external fields in this study, the probability of having different Euler's angles Ω is determined by the Boltzmann factor $e^{-\phi_{el}(r_{OO},\Omega)/(k_BT)}$. Calculating the thermal ensemble average of $<\phi_{el}(r_{OO},\Omega)>_\Omega$ over all possible Ω, we can get the

intermolecular potential function as a function of r_{OO} only, which can then be substituted into Equation 1.14 to calculate κ.

Without loss of generality, the oxygen atom of molecule i is set at the origin of the coordinate system, three atoms of molecule i are located in the plane of $x_1 - O_i - x_2$, the dipole moment of molecule i is pointed in the positive x_1-axis direction, and the separation of oxygen atoms between molecule i and j is along the x_3-axis (see Figure 2.2). If we regard molecule j as the molecule placed in an external electric field $\varphi_i(\vec{r})$ that is generated by a molecule i, ϕ_{el} can be expressed as:

$$\phi_{el} = q_O \varphi_i\left(\overrightarrow{r_{O_j}}\right) + q_H \varphi_i\left(\overrightarrow{r_{H_{j,1}}}\right) + q_H \varphi_i\left(\overrightarrow{r_{H_{j,2}}}\right) \tag{2.8}$$

in which $\overrightarrow{r_{O_j}}$, $\overrightarrow{r_{H_{j,1}}}$ and $\overrightarrow{r_{H_{j,2}}}$ are the position vectors for point charges O_j, $H_{j,1}$and $H_{j,2}$respectively.

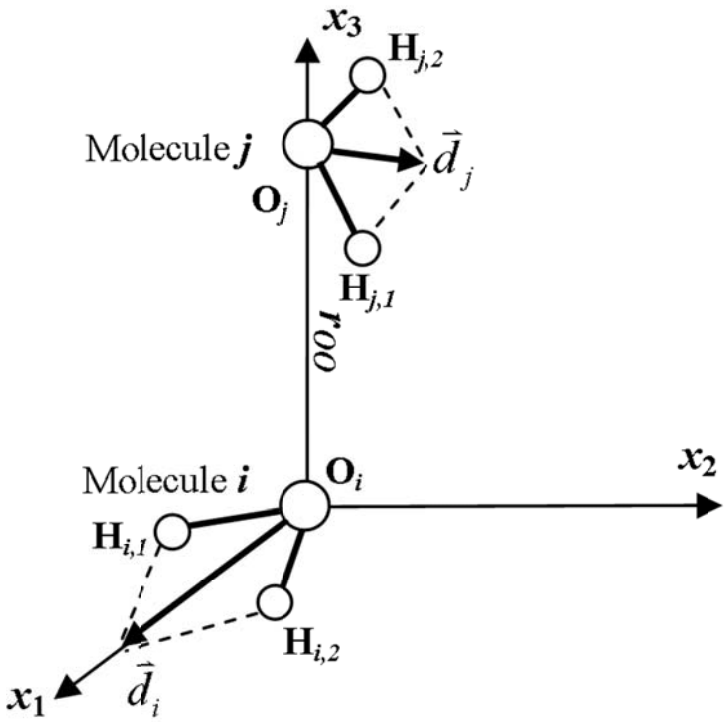

Figure 2.2 Relative positions of two water molecules in Cartesian coordinate system

Assuming the distance between the point-charge-system i and j is much larger than separations within the molecules, we can expand $\varphi_i\left(\overrightarrow{r_{O_J}}\right)$ into a series of multipole moments of molecule i. Neglecting higher order terms, which are of small magnitude, this leads to:

$$\varphi_i\left(\overrightarrow{r_{O_J}}\right) = \frac{q_i}{\left|\overrightarrow{r_{O_J}}\right|} + \frac{\overrightarrow{d_\iota} \cdot \overrightarrow{r_{O_J}}}{\left|\overrightarrow{r_{O_J}}\right|} \tag{2.9}$$

where q_i and $\overrightarrow{d_\iota}$ are the monopole and dipole moments for molecule i given by:

$$q_i = q_O + 2q_H \tag{2.10}$$

$$\overrightarrow{d_\iota} = q_O\overrightarrow{r_{O_\iota}} + q_H\overrightarrow{r_{H_{\iota,1}}} + q_H\overrightarrow{r_{H_{\iota,2}}} \tag{2.11}$$

As for $\varphi_i\left(\overrightarrow{r_{H_{J,1}}}\right)$ and $\varphi_i\left(\overrightarrow{r_{H_{J,2}}}\right)$, since:

$$\left|\overrightarrow{r_{H_{J,1}}} - \overrightarrow{r_{O_J}}\right| \ll \left|\overrightarrow{r_{O_J}}\right| \tag{2.12a}$$

$$\left|\overrightarrow{r_{H_{J,2}}} - \overrightarrow{r_{O_J}}\right| \ll \left|\overrightarrow{r_{O_J}}\right| \tag{2.12b}$$

we can expand them into Taylor series about $\overrightarrow{r_{O_J}}$. Neglecting higher order terms, which are of small magnitude, this leads to:

$$\varphi_i\left(\overrightarrow{r_{H_{J,1}}}\right) = \varphi_i\left(\overrightarrow{r_{O_J}}\right) + \nabla\varphi\left(\overrightarrow{r_{O_J}}\right) \cdot \left(\overrightarrow{r_{H_{J,1}}} - \overrightarrow{r_{O_J}}\right) \tag{2.13a}$$

$$\varphi_i\left(\overrightarrow{r_{H_{J,2}}}\right) = \varphi_i\left(\overrightarrow{r_{O_J}}\right) + \nabla\varphi\left(\overrightarrow{r_{O_J}}\right) \cdot \left(\overrightarrow{r_{H_{J,2}}} - \overrightarrow{r_{O_J}}\right) \tag{2.13b}$$

By substituting Equations 2.13a and 2.13b back into Equation 2.8, the relation for ϕ_{el} is written as:

$$\begin{aligned}\phi_{el} &= \varphi_i\left(\overrightarrow{r_{O_J}}\right)(q_O + 2q_H) + \nabla\varphi_i\left(\overrightarrow{r_{O_J}}\right)\cdot\left[q_H\left(\overrightarrow{r_{H_{J,1}}} - \overrightarrow{r_{O_J}}\right) + q_H\left(\overrightarrow{r_{H_{J,2}}} - \overrightarrow{r_{O_J}}\right)\right] \\ &= \varphi_i\left(\overrightarrow{r_{O_J}}\right)(q_O + 2q_H) + \nabla\varphi_i\left(\overrightarrow{r_{O_J}}\right)\cdot\left[q_O\overrightarrow{r_{O_J}} + q_H\overrightarrow{r_{H_{J,1}}} + q_H\overrightarrow{r_{H_{J,2}}} - (q_O + 2q_H)\overrightarrow{r_{O_J}}\right] \\ &= \varphi_i\left(\overrightarrow{r_{O_J}}\right)q_j + \nabla\varphi_i\left(\overrightarrow{r_{O_J}}\right)\cdot\left[\overrightarrow{d_J} - q_j\overrightarrow{r_{O_J}}\right]\end{aligned} \tag{2.14}$$

in which q_j and $\overrightarrow{d_J}$ are monopole and dipole moments of molecule *j* respectively.

Substituting Equation 2.9 into Equation 2.14 and using the fact that the monopole moments of water q_i and q_j equal zero, we are able to express $\phi_{el}\ as$:

$$\phi_{el} = \frac{\overrightarrow{d_\iota}\cdot\overrightarrow{d_J}}{\left|\overrightarrow{r_{O_J}}\right|^3} - \frac{3\left(\overrightarrow{d_\iota}\cdot\overrightarrow{r_{O_J}}\right)\left(\overrightarrow{d_J}\cdot\overrightarrow{r_{O_J}}\right)}{\left|\overrightarrow{r_{O_J}}\right|^5} \tag{2.15}$$

Based on the position configuration shown in Figure 2.2, we have $\overrightarrow{r_{O_\iota}}$ equals zero and:

$$\overrightarrow{r_{O_J}} = \begin{pmatrix} 0 \\ 0 \\ r_{OO} \end{pmatrix} \tag{2.16}$$

The dipole moment $\overrightarrow{d_\iota}$ is given by:

$$\overrightarrow{d_\iota} = q_O\overrightarrow{r_{O_\iota}} + q_H\left(\overrightarrow{r_{H_{\iota,1}}} + \overrightarrow{r_{H_{\iota,2}}}\right) = 2q_H L_{b,OH}\cos\frac{\alpha_{HH}}{2}\cdot\begin{pmatrix}1\\0\\0\end{pmatrix} \tag{2.17}$$

The dipole moment of $\overrightarrow{d_J}$ is expressed with respect to $\overrightarrow{d_\iota}$ by using the rotation matrix R_M:

$$\overrightarrow{d_J} = R_M \overrightarrow{d_\iota} \tag{2.18}$$

where,

$$R_M = \begin{bmatrix} \cos\beta_1 \cos\beta_2 \cos\beta_3 - \sin\beta_1 \sin\beta_3 & \sin\beta_1 \cos\beta_2 \cos\beta_3 + \cos\beta_1 \sin\beta_3 & -\sin\beta_2 \cos\beta_3 \\ -\cos\beta_1 \cos\beta_2 \sin\beta_3 - \sin\beta_1 \cos\beta_3 & -\sin\beta_1 \cos\beta_2 \sin\beta_3 + \cos\beta_1 \cos\beta_3 & \sin\beta_2 \sin\beta_3 \\ \cos\beta_1 \sin\beta_2 & \sin\beta_1 \sin\beta_2 & \cos\beta_2 \end{bmatrix} \tag{2.19}$$

here, $\Omega = (\beta_1, \beta_2, \beta_3)$, in which $0 \leq \beta_1, \beta_3 \leq 2\pi$, $0 \leq \beta_2 \leq \pi$, are the Euler's angles that describe the mutual orientation between dipole moments $\overrightarrow{d_\iota}$ and $\overrightarrow{d_J}$. Using Equations 2.16-2.18 to simply Equation 2.15, we get the following form of ϕ_{el} as a function of r_{OO} and Ω:

$$\phi_{el}(r_{OO}, \Omega) = -\frac{2\left(2q_H L_{b,OH} \cos\frac{\alpha_{HH}}{2}\right)^2 (\cos\beta_1 \cos\beta_2 \cos\beta_3 - \sin\beta_1 \sin\beta_3)}{r_{OO}^3} \tag{2.20}$$

To eliminate the dependence of ϕ_{el} on Ω , the thermal ensemble average $\langle \phi_{el}(r_{OO}, \Omega) \rangle_\Omega$ is taken over all possible mutual orientations in space. It follows that:

$$\phi_{el}(r_{OO}) = \langle \phi_{el}(r_{OO}, \Omega) \rangle_\Omega = \frac{\int_\Omega \phi_{el}(r_{OO}, \Omega) \cdot e^{-\frac{\phi_{el}(r_{OO}, \Omega)}{k_B T}} d\Omega}{\int_\Omega e^{-\frac{\phi_{el}(r_{OO}, \Omega)}{k_B T}} d\Omega} \tag{2.21}$$

Since in our study $\phi_{el} \ll k_B T$, the Boltzmann exponential term may be approximated by:

$$e^{-\frac{\phi_{el}(r_{OO},\Omega)}{k_B T}} \approx 1 - \frac{\phi_{el}(r_{OO},\Omega)}{k_B T} \tag{2.22}$$

Substituting Equation 2.22 into Equation 2.21 and using $\int_0^{2\pi}\int_0^{\pi}\int_0^{2\pi}[\cdots]d\beta_1 d\beta_2 d\beta_3$ for $\int_\Omega[\cdots]\,d\Omega$, we get the simplified form of ϕ_{el} , which is independent on Ω:

$$\phi_{el}(r_{OO}) = -\frac{3D_{water}^4}{2k_B T \cdot r_{OO}^6} \tag{2.23}$$

in which, D_{water} is the magnitude of water's dipole moment:

$$D_{water} = 2q_H L_{b,OH} \cos\frac{\alpha_{HH}}{2} \tag{2.24}$$

By substituting Equation 2.23 and 2.6 into Equation 2.5, we get the relation for $\phi_{i,j}$ as a function of r_{OO} only:

$$\phi_{i,j}(r_{OO}) = 4\epsilon_{spc/e}\left[\left(\frac{r_{spc/e}}{r_{OO}}\right)^{12} - \left(\frac{r_{spc/e}}{r_{OO}}\right)^{6}\right] - \frac{3D_{water}^4}{2k_B T \cdot r_{OO}^6} \tag{2.25}$$

With $\phi_{i,j}$ depending only on the separation between two oxygen atoms of water molecules, we can now substitute Equation 2.25 into Equation 1.14 to evaluate κ for water. The lower integral limit r_{min} is again determined by Equation 2.1, while the upper limit r_{max} is set to be ∞. Executing the integration using the derived relation for the potential function, the net result of the analysis for water is:

$$\kappa_{water} = \frac{9a_w(\hat{\rho}_l N_A)^{\frac{7}{3}} - 63b_w(\hat{\rho}_l N_A)^{\frac{1}{3}}}{21a_w(\hat{\rho}_l N_A)^3 - 63b_w(\hat{\rho}_l N_A)} \tag{2.26}$$

in which,

$$a_w = 4\epsilon_{spc/e} r_{spc/e}^{12} \tag{2.27a}$$

$$b_w = 4\epsilon_{spc/e} r_{spc/e}^{6} + \frac{3D_{water}^4}{2k_B T} \tag{2.27b}$$

As in the case of argon, $\hat{\rho}_l$ has to be specified for a given temperature to determine a numerical value of κ_{water} from Equation 2.26. Because in Carey's scheme [14] density is set to be uniform in the system for the bulk saturation state (i.e. $\hat{\rho}'$and $\hat{\rho}$" are set to be zero), κ and the potential function will not play a role in the calculation of the saturated liquid density $\hat{\rho}_l$. So, for water, the Redlich–Kwong model predictions of saturation properties, represented in dimensionless form in Table 2.1, are used to determine the saturation liquid density, and the relation for κ_{water}, Equation 2.26, incorporating dipole and van der Waals forces is used to account for density variation $\hat{\rho}$" effects in the capillarity model. By matching water's measured critical temperature T_c and critical pressure P_c, the equation of state, zero slope: $(\partial P/\partial \hat{v})_T = 0$, and inflection point: $(\partial^2 P/\partial \hat{v}^2)_T = 0$ relations are solved simultaneously, yielding the numerical values of Redlich-Kwong constants a_{R0}, b_R, and the critical density $\hat{\rho}_c$ indicated in Table 2.3. After substituting κ_{water} and other constants from Table 2.3 into Equation 1.13 for a given temperature, the log of the partition function $\ln(Q)$ incorporates the effect of the second derivate of the density profile $\rho"(z)$ in a form that facilitates its use in the film molecular capillarity analysis.

§ 2.2 INTERFACIAL VOLUMETRIC FREE ENERGY

Using the definition of free energy per unit volume ψ in Equation 1.15 and the expression of $\ln Q$ given in Equation 1.13, we have:

$$\begin{aligned}\psi = &-\hat{\rho}RT - \hat{\rho}RT \ln\left[\frac{1-\hat{\rho}N_A b_R}{\hat{\rho}N_A \Lambda^3}\right] - \hat{\rho}RT\left[\frac{\xi-5}{2}\ln\pi - \ln\sigma_s\right] \\ &- \frac{\xi-3}{2}\hat{\rho}RT\ln\left(\frac{T}{\theta_{rot,m}}\right) - \frac{a_{R0}N_A\hat{\rho}}{b_R T^{1/2}}\ln(1+\hat{\rho}N_A b_R) \\ &- \frac{a_{R0}N_A\kappa\hat{\rho}"(z)}{2b_R T^{1/2}}\ln(1+\hat{\rho}N_A b_R)\end{aligned} \tag{2.28}$$

in which, R is the universal gas constant, and Λ is defined as:

$$\Lambda = \left[\frac{h^2}{2\pi M k_B T}\right]^{1/2} \tag{2.29}$$

Since in Equation 2.28 only the last term on the right side accounts for the effect of non-uniform density profile, we consider the volumetric free energy ψ consisting of two parts:

$$\psi = \psi_0(\hat{\rho}) - m(\hat{\rho}) \cdot \hat{\rho} \cdot \hat{\rho}'' \tag{2.30}$$

where $\psi_0(\hat{\rho})$ accounts for the uniform density part of ψ:

$$\begin{aligned}\psi_0(\hat{\rho}) = -\hat{\rho}RT - \hat{\rho}RT \ln\left[\frac{1-\hat{\rho}N_A b_R}{\hat{\rho}N_A\Lambda^3}\right] - \hat{\rho}RT\left[\frac{\xi-5}{2}\ln\pi - \ln\sigma_s\right] \\ -\frac{\xi-3}{2}\hat{\rho}RT\ln\left(\frac{T}{\theta_{rot,m}}\right) - \frac{a_{R0}N_A\hat{\rho}}{b_R T^{1/2}}\ln(1+\hat{\rho}N_A b_R)\end{aligned} \tag{2.31}$$

and $m(\hat{\rho}) \cdot \hat{\rho} \cdot \hat{\rho}''$ provides the correction for the effect of non-uniform density distribution, in which $m(\hat{\rho})$ is defined as:

$$m(\hat{\rho}) = \frac{a_{R0}N_A\kappa}{2b_R T^{1/2}}\ln(1+\hat{\rho}N_A b_R) \tag{2.32}$$

We consider here the idealized configuration of a sandwiched liquid film (see Figure 1.8) with a characteristic thickness $\delta_{ml} = \hat{n}''/\hat{\rho}_l$, where $\hat{n}''$ is the moles of fluid per unit area of film and $\hat{\rho}_l$ is the saturation molar density for bulk liquid. Note that this film molar loading thickness quantifies the molar (or mass) loading of the film per unit area. It is the thickness that the film would have if the density everywhere in the film was equal to the saturated bulk liquid value. The half film (centerline to vapor) free energy σ is defined as one half of the system excess free energy (per unit area of interface) above that for step changes in density at the interfaces of $z = -\delta_{ml}/2$ and $z = \delta_{ml}/2$ for the idealized initial state. The half film free energy σ is computed as:

$$\sigma = \frac{1}{2}\left\{\int_{-\infty}^{-\delta_{ml}/2}[\psi(\hat{\rho}) - \psi(\hat{\rho}_v)]dz + \int_{-\delta_{ml}/2}^{\delta_{ml}/2}[\psi(\hat{\rho}) - \psi(\hat{\rho}_l)]dz + \int_{\delta_{ml}/2}^{\infty}[\psi(\hat{\rho}) - \psi(\hat{\rho}_v)]dz\right\} \tag{2.33}$$

in which, the factor of $1/2$ accounts for two identical interfacial regions in this configuration. This can be written in the form:

$$\sigma = \frac{1}{2}\int_{-\infty}^{\infty}[\psi(\hat{\rho}) - \psi_{sla}(\hat{\rho})]dz \tag{2.34}$$

where ψ_{sla} is the straight-line approximation of ψ between saturation vapor and liquid densities as shown in Figure 2.3.

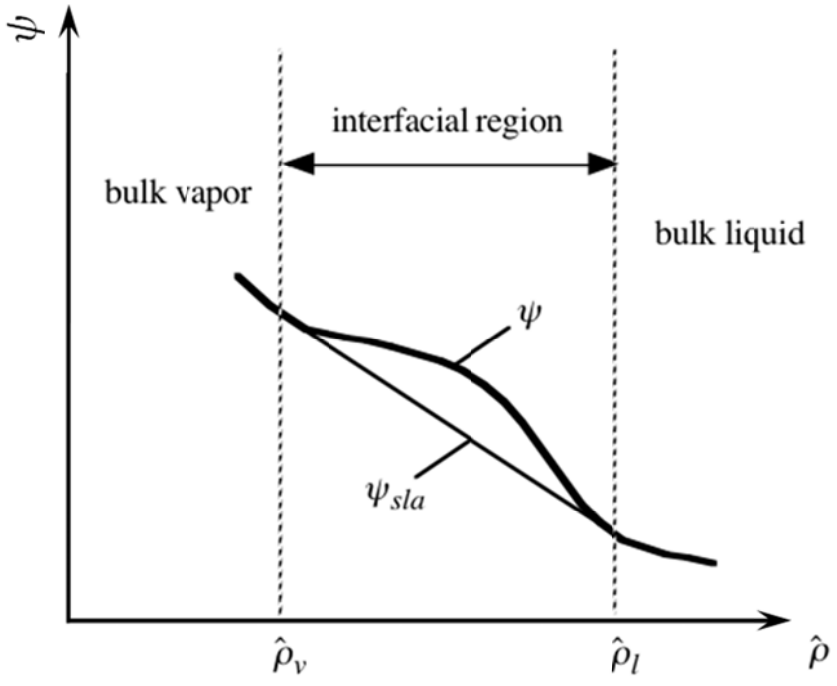

Figure 2.3 Variation of volumetric free energy with molar density.

$$\psi_{sla}(\hat{\rho}) = \psi(\hat{\rho}_v) + \left[\frac{\psi(\hat{\rho}_v) - \psi(\hat{\rho}_l)}{\hat{\rho}_v - \hat{\rho}_l}\right](\hat{\rho} - \hat{\rho}_v) \tag{2.35}$$

Substituting Equation 2.30, Equation 2.31, Equation 2.32 into Equation 2.35, and noticing that for a pure substance the specific Gibbs function $\hat{g} = \hat{f} + P\hat{v}$ is equivalent to the chemical potential $\hat{\mu}$, the expression of ψ_{sla} simplifies to:

$$\psi_{sla} = \psi_0(\hat{\rho}_v) + \hat{\mu}_v(\hat{\rho} - \hat{\rho}_v) \tag{2.36}$$

where, $\hat{\mu}_v$ is the molar chemical potential for saturated vapor. Substituting Equation 2.30, Equation 2.36 back into Equation 2.34, and using the symmetry property of the configuration, we can reorganize Equation 2.34 as:

$$\sigma = \int_{-\infty}^{0} \psi_e(\hat{\rho})dz - \int_{-\infty}^{0} m(\hat{\rho}) \cdot \hat{\rho} \cdot \hat{\rho}"dz \tag{2.37}$$

where, $\psi_e(\hat{\rho})$ is defined as excess volumetric free energy:

$$\psi_e(\hat{\rho}) = \psi_0(\hat{\rho}) - \psi_0(\hat{\rho}_v) - \hat{\mu}_v \cdot (\hat{\rho} - \hat{\rho}_v) \tag{2.38}$$

Two boundary conditions are specified for the density profile $\hat{\rho}(z)$:

$$\hat{\rho}'|_{z=0} = 0 \tag{2.39}$$

$$\hat{\rho}|_{z\to-\infty} = \hat{\rho}_v \tag{2.40}$$

Condition 2.40 implies that:

$$\hat{\rho}'|_{z\to-\infty} = 0 \tag{2.41}$$

The first boundary condition 2.39 comes from the symmetry of the configuration; the second 2.40 and Equation 2.41 come from the requirement that density and density gradient at infinity should not be affected by density variations in the film.

By using boundary conditions Equation 2.39 and 2.41, the expression of interfacial free energy can be further simplified via integration by parts on the second integral term in Equation 2.37 to obtain:

$$\sigma = \int_{-\infty}^{0} \left[\psi_e(\hat{\rho}) + \frac{1}{2}\hat{\rho}'^2 \tilde{m}(\hat{\rho})\right] dz \tag{2.42}$$

where,

$$\tilde{m}(\hat{\rho}) = 2\left[m + \hat{\rho}\,\frac{dm}{d\hat{\rho}}\right] = \frac{a_{R0}N_A^2\kappa}{(1+\hat{\rho}b_R N_A)\cdot T^{1/2}} \tag{2.43}$$

§ 2.3 DETERMINATION OF DENSITY PROFILES

Based on thermodynamic arguments, the equilibrium density profile $\hat{\rho}(z)$ is that which minimizes the half film interfacial free energy σ determined from the integral in Equation 2.42. The density profile $\hat{\rho}(z)$ must also satisfy the three boundary conditions given in Equations 2.39, 2.40 and 2.41. The law of conservation of mass also requires that $\hat{\rho}(z)$ must satisfy the following constraint condition:

$$\int_{-\infty}^{0} (\hat{\rho} - \hat{\rho}_v) dz = \frac{\delta_{ml}}{2} (\hat{\rho}_l - \hat{\rho}_v) \tag{2.44}$$

This formulation defines a classical isoperimetric calculus of variations problem to determine a functional solution minimizing an integral and satisfying a constraint condition. Mathematically, this type problem is solved by converting it to an Euler-Lagrange equation [16]. Introducing the Lagrange multiplier λ, and setting:

$$f(z, \hat{\rho}, \hat{\rho}') = \psi_e(\hat{\rho}) + \frac{1}{2} \hat{\rho}^2 \tilde{m}(\hat{\rho}) \tag{2.45}$$

$$g(z, \hat{\rho}, \hat{\rho}') = \hat{\rho} - \hat{\rho}_v \tag{2.46}$$

we obtain the corresponding Euler-Lagrange equation as:

$$\frac{\partial (f + \lambda \cdot g)}{\partial \hat{\rho}} - \frac{d}{dz} \left[\frac{\partial (f + \lambda \cdot g)}{\partial \hat{\rho}'} \right] = 0 \tag{2.47}$$

Substituting the expressions for f and g (Equation 2.45 and Equation 2.46) into Equation 2.47, we get the following second-order non-linear ordinary differential equation for $\hat{\rho}$:

$$\frac{d\psi_e(\hat{\rho})}{d\hat{\rho}} - \frac{1}{2} \hat{\rho}'^2 \frac{d\tilde{m}(\hat{\rho})}{d\hat{\rho}} - \tilde{m}(\hat{\rho}) \hat{\rho}'' + \lambda = 0 \tag{2.48}$$

This equation can be simplified to a first-order ordinary differential equation by introducing $\hat{\rho}'$ as a new variable and using the identity:

$$\hat{\rho}'' = \hat{\rho}' \frac{d}{d\hat{\rho}} \hat{\rho}' \tag{2.49}$$

This converts Equation 2.48 to:

$$2\frac{d\psi_e}{d\hat{\rho}} - \frac{d}{d\hat{\rho}}(\hat{\rho}'^2\widetilde{m}) + 2\lambda = 0 \tag{2.50}$$

This can be solved by integration using boundary conditions Equation 2.40 and Equation 2.41, yielding the relation:

$$\hat{\rho}' = \left[\frac{2\psi_e + 2\lambda(\hat{\rho} - \hat{\rho}_v)}{\widetilde{m}}\right]^{\frac{1}{2}} \tag{2.51}$$

The Lagrange multiplier λ is a purely mathematical term. But we can relate it to $\hat{\rho}_{cl}$, the local density at the centerline $(z = 0)$ by combining the boundary condition of Equation 2.39 with Equation 2.51 to obtain:

$$\lambda = \frac{\psi_e(\hat{\rho}_{cl})}{\hat{\rho}_v - \hat{\rho}_{cl}} \tag{2.52}$$

With this result, Equation 2.51 can be written as:

$$\hat{\rho}' = \left\{\frac{2\psi_e(\hat{\rho}) - 2\psi_e(\hat{\rho}_{cl})\left[\frac{\hat{\rho} - \hat{\rho}_v}{\hat{\rho}_{cl} - \hat{\rho}_v}\right]}{\widetilde{m}(\hat{\rho})}\right\}^{\frac{1}{2}} \tag{2.53}$$

To determine $\hat{\rho}_{cl}$, the constraint condition equation 2.44 is used:

$$\frac{\delta_{ml}}{2}(\hat{\rho}_l - \hat{\rho}_v) = \int_{-\infty}^{0} (\hat{\rho} - \hat{\rho}_v)\, dz = \int_{z\to-\infty}^{z\to 0} (\hat{\rho} - \hat{\rho}_v)\frac{1}{\hat{\rho}'}\, d\hat{\rho} = \int_{\hat{\rho}\to\hat{\rho}_v}^{\hat{\rho}\to\hat{\rho}_{cl}} (\hat{\rho} - \hat{\rho}_v)\frac{1}{\hat{\rho}'}\, d\hat{\rho}$$
$$= \int_{\hat{\rho}_v}^{\hat{\rho}_{cl}} \left\{ (\hat{\rho} - \hat{\rho}_v) \cdot \left[\frac{\widetilde{m}(\hat{\rho})}{2\psi_e(\hat{\rho}) - 2\left[\frac{\hat{\rho} - \hat{\rho}_v}{\hat{\rho}_{cl} - \hat{\rho}_v}\right]\psi_e(\hat{\rho}_{cl})} \right]^{\frac{1}{2}} \right\} d\hat{\rho} \tag{2.54}$$

Rearranging Equation 2.54, we obtain an equation that dictates $\hat{\rho}_{cl}$:

$$\delta_{ml} = \delta_{equiv}(\hat{\rho}_{cl}) \tag{2.55}$$

where the function on the right hand side has unit of lengths and is a function of $\hat{\rho}_{cl}$:

$$\delta_{equiv}(\hat{\rho}_{cl}) = \frac{2}{\hat{\rho}_l - \hat{\rho}_v} \cdot \int_{\hat{\rho}_v}^{\hat{\rho}_{cl}} \left\{ (\hat{\rho} - \hat{\rho}_v) \cdot \left[\frac{\widetilde{m}(\hat{\rho})}{2\psi_e(\hat{\rho}) - 2\left[\frac{\hat{\rho} - \hat{\rho}_v}{\hat{\rho}_{cl} - \hat{\rho}_v}\right]\psi_e(\hat{\rho}_{cl})} \right]^{\frac{1}{2}} \right\} d\hat{\rho} \tag{2.56}$$

Note that the lower limit on the integral is chosen to exceed $\hat{\rho}_v$ by a small amount $\epsilon_{\hat{\rho}}$ because ψ_e is zero and the integrand is singular at $\hat{\rho}_v$. Likewise, the upper limit is chosen to be no more than $\hat{\rho}_{cl} - \epsilon_{\hat{\rho}}$ because the integrand is singular at $\hat{\rho}_{cl}$. The integrand approaches a well-defined limit as $\epsilon_{\hat{\rho}} \to 0$ because of its asymptotical behavior. Computationally, choosing $\epsilon_{\hat{\rho}}$ to be very small compared to $\hat{\rho}_v$ provides an accurate prediction of this asymptotical value.

In executing this analysis, for a given temperature and film molar loading thickness $\delta_{ml} = \hat{n}''/\hat{\rho}_{cl}$, we first determine the centerline density $\hat{\rho}_{cl}$ by numerically integrating Equation 2.55. Then, by integrating Equation 2.53 numerically with the derived $\hat{\rho}_{cl}$, we obtain the corresponding density profile.

§ 2.4 COMPARISON OF THICK HALF FILM WITH A SINGLE INTERFACE

If we increase the film molar loading thickness δ_{ml} to infinite in our model and only consider half of the system based on the argument of symmetry, the configuration of our model essentially reduces to Carey's single-interface model [14]. In this limit $\delta_{ml} \to \infty$, $\hat{\rho}_{cl} = \hat{\rho}_l$, and the free energy and interfacial region thickness for each half film should then be equivalent to a single interface between two bulk phases under comparable conditions. To calculate the thick film limit values of the non-dimensional interfacial region thickness δ_i/L_i and the non-dimensional surface tension $\sigma/(P_c L_i)$ as $\delta_{ml} \to \infty$ at various temperatures, we first calculate the corresponding asymptotical density profiles. The non-dimensionalization constants used here are the critical pressure P_c and the length scale L_i defined as:

$$L_i = \left(\frac{k_B T_c}{P_c}\right)^{\frac{1}{3}} \tag{2.57}$$

For most fluids, this length scale is close to nanometer. For argon, $L_i = 0.753$ nm, whereas for water $L_i = 0.739$ nm. Invoking the fact that $\hat{\rho}_{cl} = \hat{\rho}_l$ in this limit, after some algebra manipulation of Equation 2.53, we obtain:

$$\hat{\rho}' = \left[\frac{2\psi_e(\hat{\rho})}{\widetilde{m}(\hat{\rho})}\right]^{\frac{1}{2}} \tag{2.58}$$

The density profile is then computed by numerical integration Equation 2.58 for half of the film: $z \in (-\infty, 0)$.

We define z_c as the z coordinate at the centerline of the interface, dictated by:

$$\hat{\rho}(z)|_{z=z_c} = \frac{\hat{\rho}_v + \hat{\rho}_l}{2} \tag{2.59}$$

Following Carey [14], the thickness of the interfacial region δ_i is then defined as:

$$\delta_i = \frac{\hat{\rho}_l - \hat{\rho}_v}{\hat{\rho}'|_{z=z_c}} \tag{2.60}$$

Using density profile results generated by our model together with Equation 2.60 and computed values of the half film free energy, limiting case ($\delta_{ml} \to \infty$) values of δ_i/L_i and $\sigma/(P_c L_i)$ are obtained for water and argon at various T_r. The numerical results of δ_i/L_i and $\sigma/(P_c L_i)$ for argon are exactly the same as those predicted by the model of Carey [14], since the same Lennard-Jones 12-6 potential function is used in both Carey's model and our model. For water, the numerical results are slightly different due to the fact that SPC/E potential function was used in our study. For water, as the temperature approaches the critical point value, δ_i/L_i and $\sigma/(P_c L_i)$ approach the following power law asymptotic variations:

$$\frac{\delta_i}{L_i} = 0.768(1 - T_r)^{-0.591} \tag{2.61}$$

$$\frac{\sigma}{P_c L_i} = 17.8(1 - T_r)^{1.441} \tag{2.62}$$

In contrast, the Redlich-Kwong model developed by Carey [14] predicts that for water as $T_r \to 1$, the power law asymptotic variations of δ_i/L_i and $\sigma/(P_c L_i)$ are:

$$\frac{\delta_i}{L_i} = 0.683(1 - T_r)^{-0.670} \tag{2.63}$$

$$\frac{\sigma}{P_c L_i} = 14.4(1 - T_r)^{1.328} \tag{2.64}$$

Using the same power law function form, we curve-fit the asymptotic variation of NIST recommended surface tension data [41] for water:

$$\frac{\sigma}{P_c L_i} = 20.4(1 - T_r)^{1.441} \tag{2.65}$$

As shown in Figure 2.4, the surface tension variation of water predicted by Equation 2.62, based on SPC/E potential function, compares more favorably to the NIST recommended data than that predicted by Equation 2.64, based on Lennard-Jones potential function.

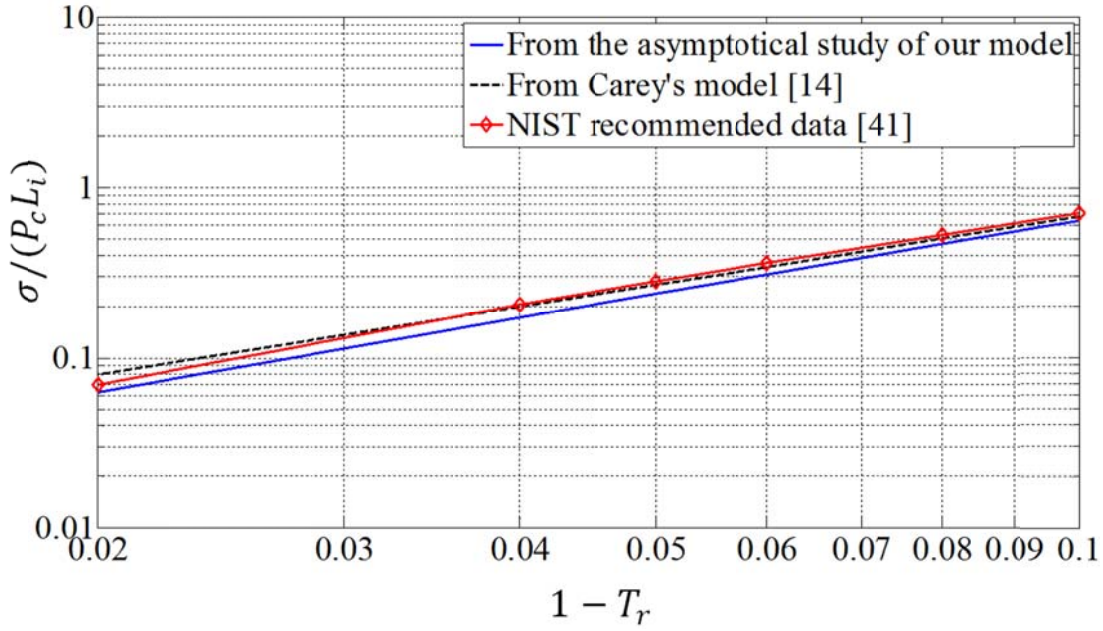

Figure 2.4 Comparison of $\sigma/(P_c L_i)$ for water among this study, Carey's model [14] and NIST data [41]

§ 2.5 EXPLORATION OF INTRINIC STABILITY

Stability analysis is carried out at a specified reduced temperature by comparing the computed density profiles for various values of film molar loading thickness $\delta_{ml} = \hat{n}''/\hat{\rho}_l$ with the density values corresponding to the limits of intrinsic stability. The spinodal limits of intrinsic stability are determined from the Redlich–Kwong equation of state in the manner described by Carey [14]. We postulate here that the model predicts film rupture when the film core lacks intrinsic stability. In this way, the critical thickness δ_c, i.e. the minimum film thickness that will not rupture spontaneously, is determined for the specified temperature. The effect of temperature on stability is studied by using this approach to predict the relationship between the critical thickness and system temperature.

Density profiles and intrinsic stability for argon liquid film at $T_r = 0.6$

Reduced temperature of $T_r = 0.6$ is chosen as an example to illustrate the process of determining the critical thickness δ_c from the density profiles of various values of film molar loading thickness $\delta_{ml} = \hat{n}''/\hat{\rho}_l$.

In using Equation 2.55 to execute the analysis of determining the local density $\hat{\rho}_{cl}$ at the centerline $(z = 0)$ described above, we use argon properties from Table 2.2, together with κ_{argon} from Equation 2.2. The resulting variation of $\hat{\rho}_{cl}$ with film molar loading thickness δ_{ml} indicated by the analysis at $T_r = 0.6$ is plotted in Figure 2.5.

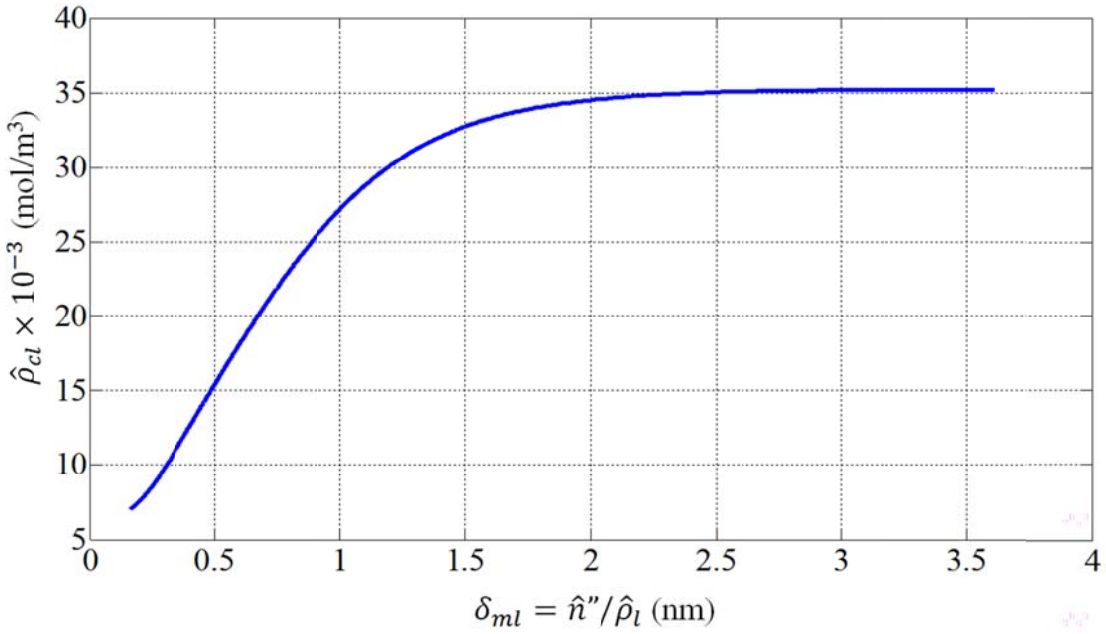

Figure 2.5 Variation of $\hat{\rho}_{cl}$ with $\delta_{ml} = \hat{n}''/\hat{\rho}_l$ for argon at $T_r = 0.6$ predicted by Equation 2.55

Density profiles across the film are determined by numerically integrating Equation 2.53 using the computationally determined values of $\hat{\rho}_{cl}$ for each δ_{ml} value. The resulting density profiles for argon at $T_r = 0.6$ are shown in Figures 2.6 to Figure 2.9 with decreasing δ_{ml} values.

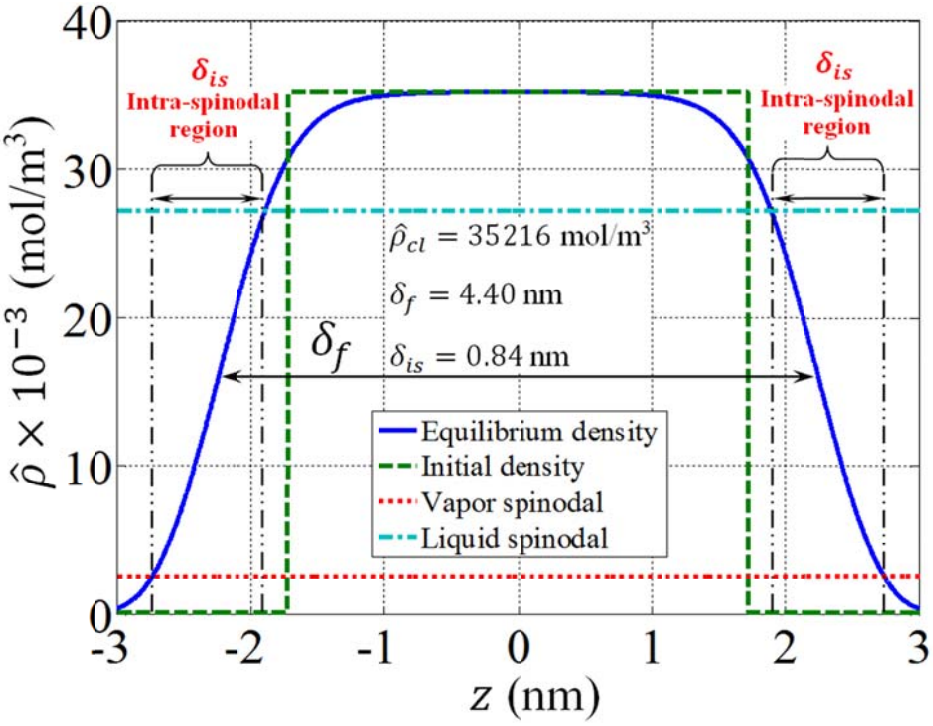

Figure 2.6 Density profile for argon at $T_r = 0.6$, $\delta_{ml} = 3.44$ nm

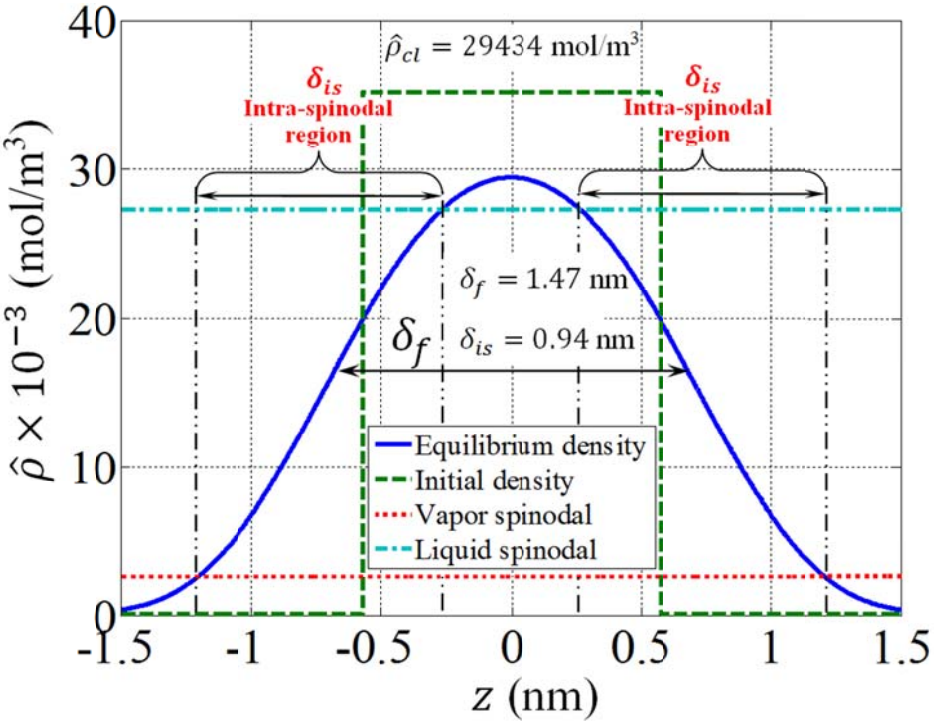

Figure 2.7 Density profile for argon at $T_r = 0.6$, $\delta_{ml} = 1.15$ nm

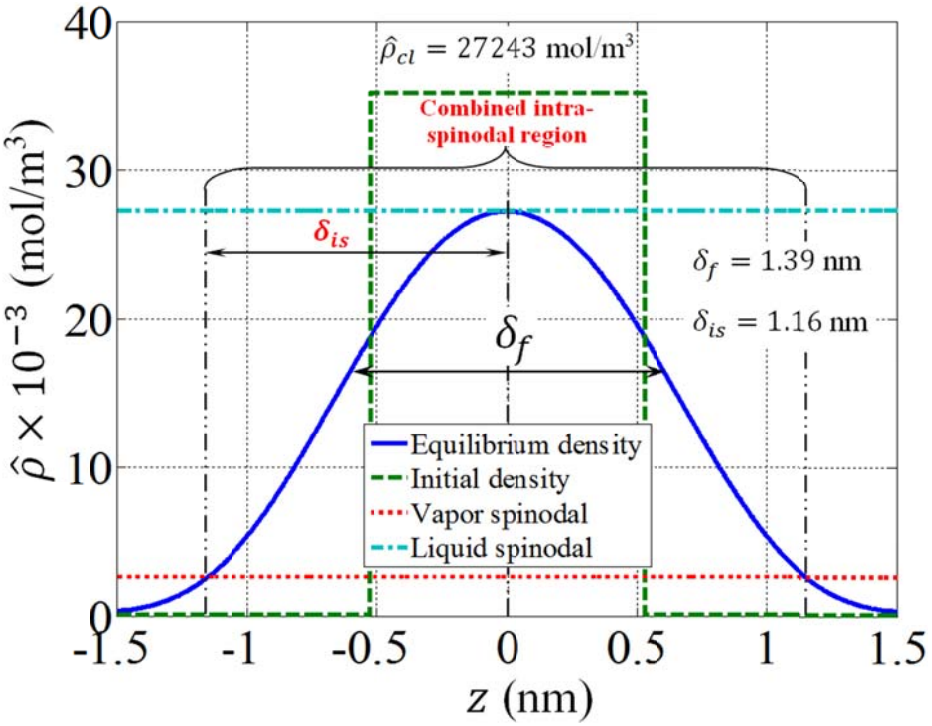

Figure 2.8 Density profile for argon at $T_r = 0.6$, $\delta_{ml} = 1.05$ nm (conditions resulting in incipient loss of film core stability)

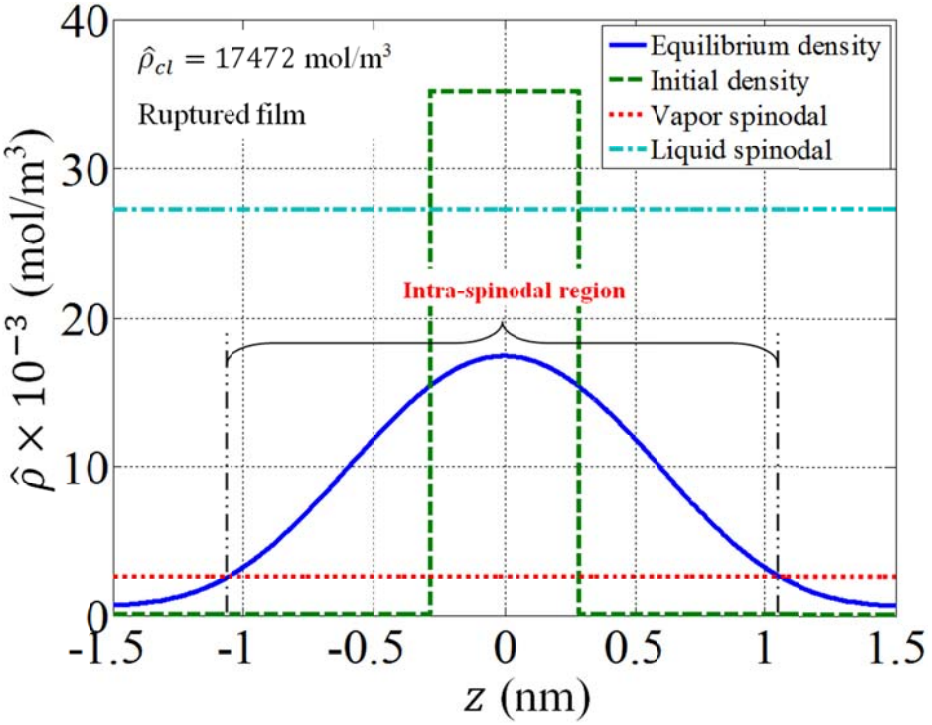

Figure 2.9 Density profile for argon at $T_r = 0.6$, $\delta_{ml} = 0.57$ nm (conditions resulting in ruptured film)

Also shown in some of the above figures are the mean density film thicknesses δ_f for equilibrium film density profiles, and thicknesses of the intra-spinodal sublayers δ_{is}. δ_f is defined as:

$$\delta_f = z_r - z_l \tag{2.66}$$

where, z_l and z_r are the z coordinates at which the local density in the interfacial regions is equal to the mean value of $\hat{\rho}_{cl}$ and $\hat{\rho}_v$:

$$\hat{\rho}(z)|_{z=z_l<0} = \hat{\rho}(z)|_{z=z_r>0} = \frac{\hat{\rho}_v + \hat{\rho}_{cl}}{2} \tag{2.67}$$

In general, δ_f differs from the film molar loading thickness δ_{ml}. The intra-spinodal sublayer thickness δ_{is} is defined as:

$$\delta_{is} = z_{spinodal,l} - z_{spinodal,v} \tag{2.68}$$

where, $z_{spinodal,l}$ and $z_{spinodal,v}$ are the z coordinates at which the local density within the left half of the film ($z < 0$) is equal to the spinodal liquid density $\hat{\rho}_{spinodal,l}$ and the spinodal vapor density $\hat{\rho}_{spinodal,v}$ respectively:

$$\hat{\rho}(z)|_{z=z_{spinodal,l}<0} = \hat{\rho}_{spinodal,l} \tag{2.69a}$$

$$\hat{\rho}(z)|_{z=z_{spinodal,v}<0} = \hat{\rho}_{spinodal,v} \tag{2.69b}$$

The values of δ_f and δ_{is}/L_i predicted by the model analysis are also listed in Table 2.4 for argon.

Based on the series of plots shown from Figure 2.6 to Figure 2.9, some common characteristics of density profiles can be summarized:

1. Density profiles exhibit steep gradient interfacial regions at the edges of the film. The maximum local densities exist at $z = 0$, where centers of initial film regions are located:

$$\hat{\rho}_{max} = \hat{\rho}_{cl} \tag{2.70}$$

2. With the decrease of film molar loading thickness δ_{ml}, the local density at the centerline $\hat{\rho}_{cl}$ decreases.
3. Consistent with Carey's study of the interfacial region between semi-infinite vapor and semi-infinite liquid regions [14], our results also indicate that there are two inner sublayers of the interfacial regions in which local densities are between the spinodal vapor and spinodal liquid densities predicted by the Redlich-Kwong equation of state. Based on classical thermodynamics, these intra-spinodal sublayers are expected to lack stability because the intrinsic stability requirement criterion $(\partial P/\partial \hat{v})_T < 0$ is not satisfied.
4. With the decrease of film molar loading thickness δ_{ml}, the intra-spinodal sublayer thickness δ_{is} increases, meaning that unstable intra-spinodal sublayers on both sides of a film span an increasing fraction of the film. Eventually the unstable sublayers merge and span most of the thickness of the film. This apparent progressive destabilization of the film appears to be a mechanism for film rupture. We therefore take the onset of rupture to correspond to $\hat{\rho}_{cl}$ between the spinodal limits. When this is the case, the core of the film is an intra-spinodal layer, suggesting that the bulk of the film lacks intrinsic stability. For these conditions, δ_{is} and δ_f are not indicated in Figure 2.9.

Here we interpret the thinnest stable film thickness (critical thickness) δ_c, as the value of δ_f corresponding to the incipient merging of the intra-spinodal sublayers from both sides of a film. As shown in Figure 2.8, in terms of density, the merging is equivalent to the decrease of $\hat{\rho}_{cl}$ to the liquid spinodal density $\hat{\rho}_{spinodal,l}$. This dictates the following condition as a means to calculate the critical thickness:

$$\hat{\rho}_{cl} = \hat{\rho}_{spinodal,l} \tag{2.71}$$

Substituting this value of $\hat{\rho}_{cl}$ back into Equation 2.53 and integrating it numerically, we are able to obtain the density profile, from which we determine the mean density film thickness δ_f, i.e., the critical thickness δ_c corresponding to this specified temperature. For the case of argon at $T_r = 0.6$, which we demonstrated here, the critical thickness therefore is indicated in Figure 2.8 as $\delta_c = 1.39$ nm.

With density profiles derived, the half-interface free energy σ for each film molar loading thickness δ_{ml} are calculated by numerical integration on Equation 2.42. Summarized in Table 2.4 are the local density at the centerline $\hat{\rho}_{cl}$, non-dimensional half-interface free energy $\sigma/(P_c L_i)$, non-dimensional intra-spinodal sublayer thickness δ_{is}/L_i, non-dimensional interfacial

region thickness δ_i/L_i (for thick film only, which represents interfaces between bulk phases), and the mean density film thicknesses δ_f.

Table 2.4
Calculated results for argon at $T_r = 0.6$ for four typical δ_{ml} values

δ_{ml} (nm)	3.44	1.15	1.05	0.57
$\hat{\rho}_{cl}$ (mol/m^3)	35,216	29,434	27,243	17,472
$\sigma/(P_c L_i)$	4.84	4.71	4.61	3.78
δ_{is}/L_i	1.12	1.25	1.53	–
δ_i/L_i	1.20	–	–	–
δ_f (nm)	4.40	1.47	1.39	–

Density profiles and intrinsic stability for water liquid film at $T_r = 0.6$

By using water properties from Table 2.3, together with κ_{water} from Equation 2.26, the variation of the local density $\hat{\rho}_{cl}$ at the centerline ($z = 0$) with film molar loading thickness δ_{ml} for water at $T_r = 0.6$, as predicted by Equation 2.55, is plotted in Figure 2.10.

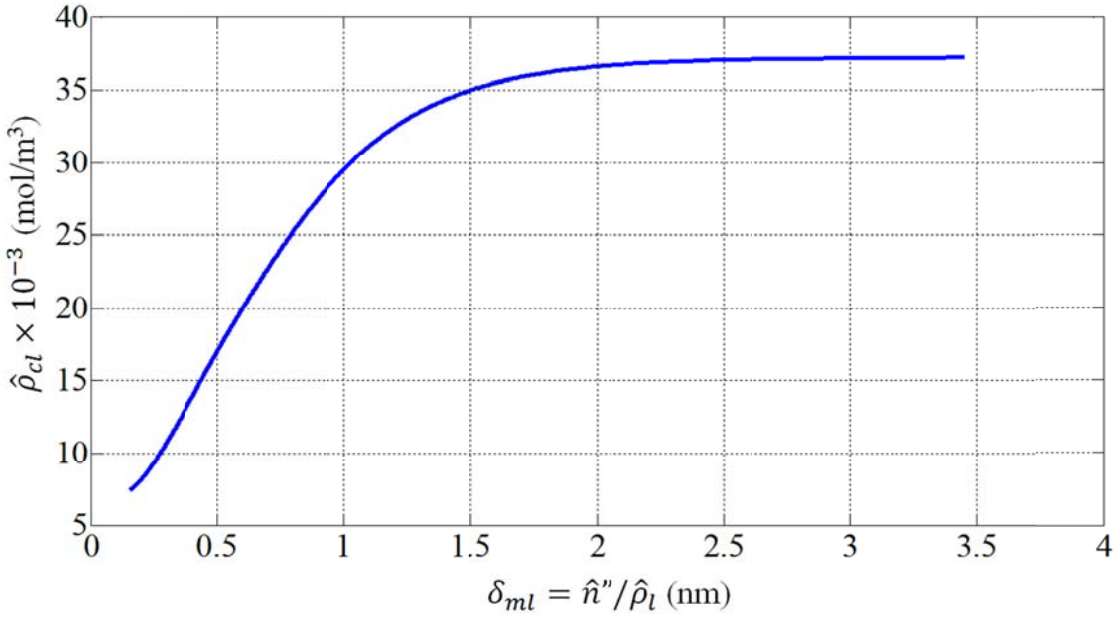

Figure 2.10 Variation of $\hat{\rho}_{cl}$ with $\delta_{ml} = \hat{n}''/\hat{\rho}_l$ for water at $T_r = 0.6$ predicted by Equation 2.55

Density profiles across the film are determined by numerically integrating Equation 2.53 using the computationally determined values of $\hat{\rho}_{cl}$ for each δ_{ml} value. The resulting density profiles for water at $T_r = 0.6$ are shown in Figures 2.11 to Figure 2.14 with decreasing δ_{ml} values.

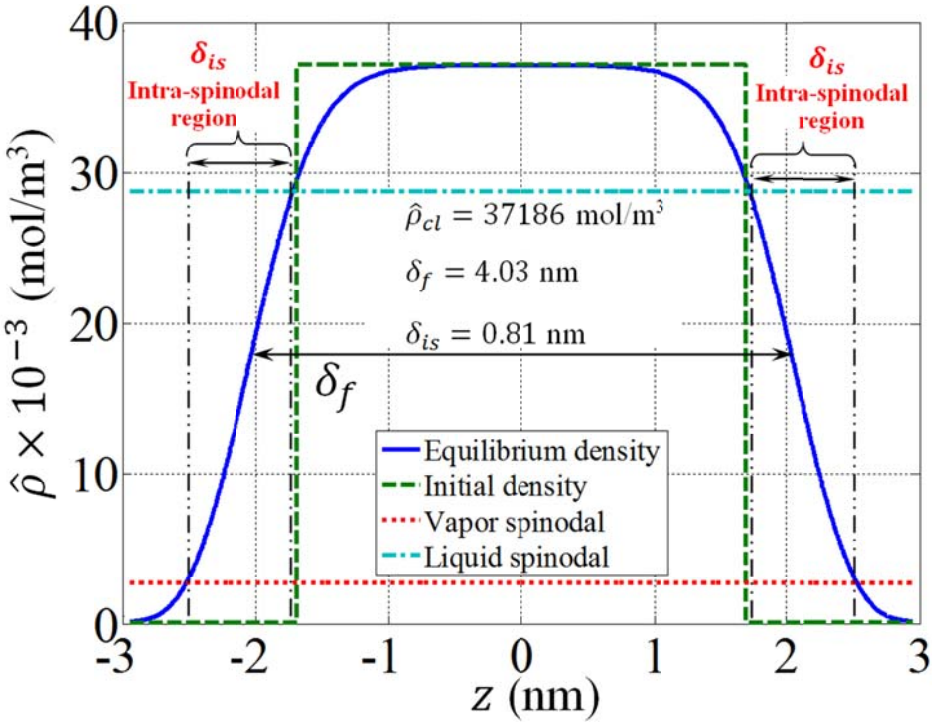

Figure 2.11 Density profile for water at $T_r = 0.6$, $\delta_{ml} = 3.38$ nm

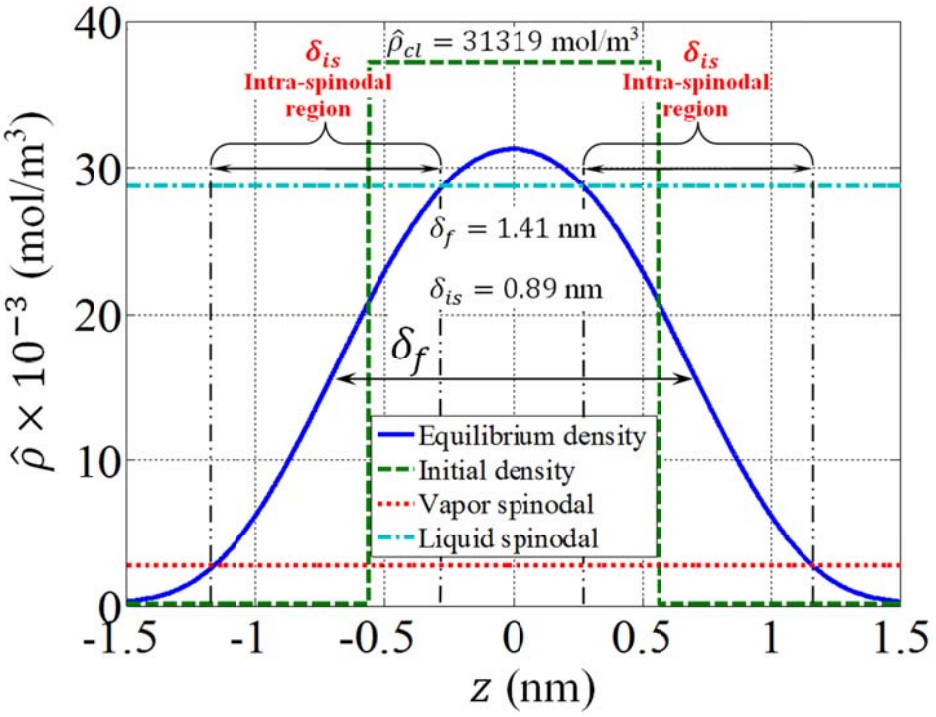

Figure 2.12 Density profile for water at $T_r = 0.6$, $\delta_{ml} = 1.13$ nm

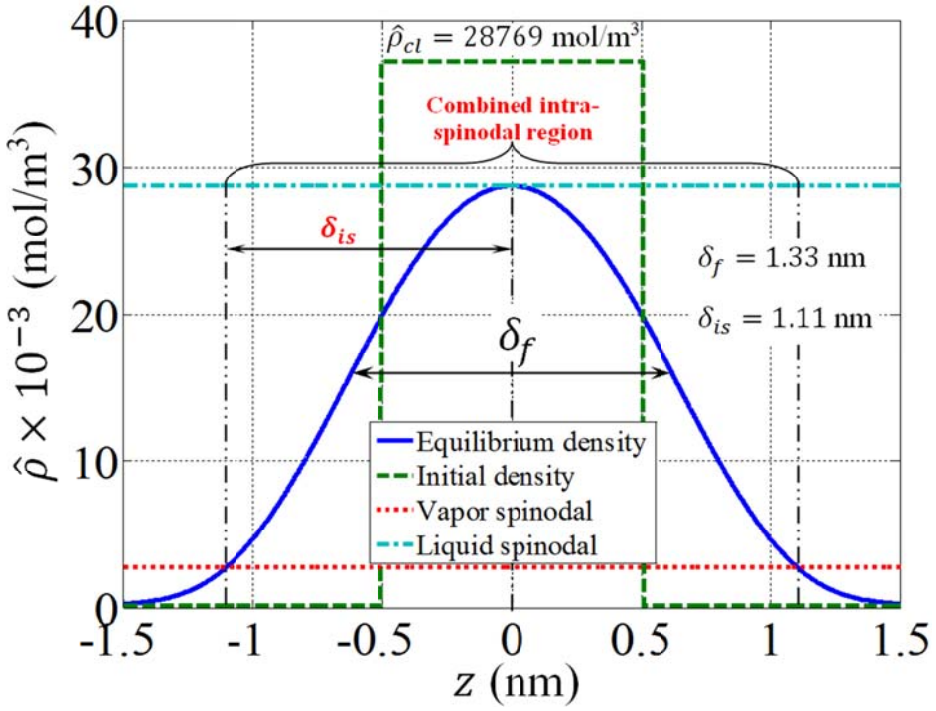

Figure 2.13 Density profile for water at $T_r = 0.6$, $\delta_{ml} = 1.01$ nm (conditions resulting in incipient loss of film core stability)

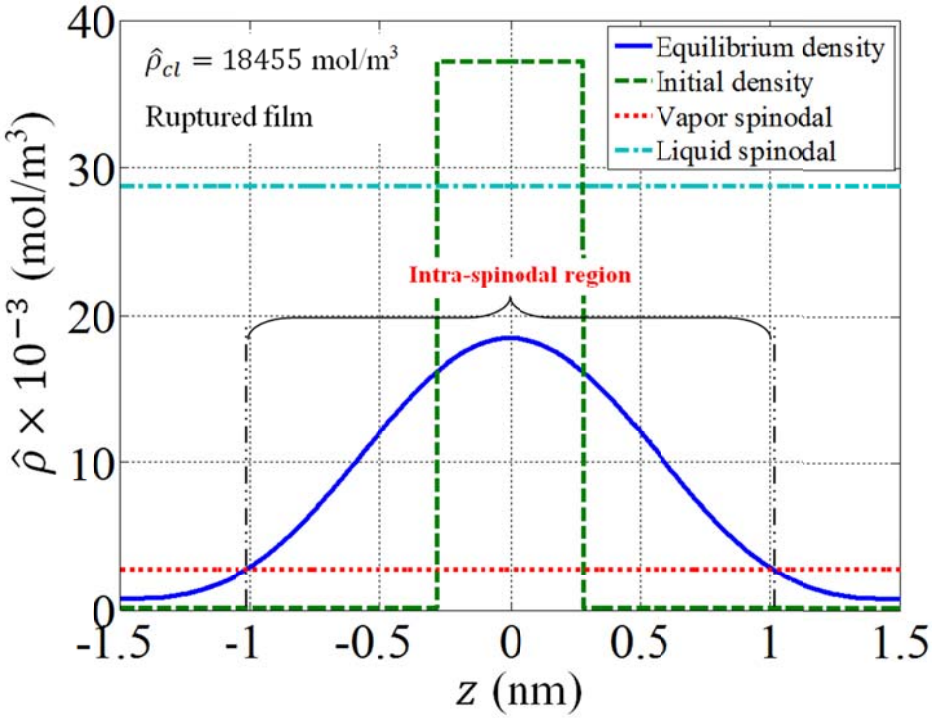

Figure 2.14 Density profile for water at $T_r = 0.6$, $\delta_{ml} = 0.56$ nm (conditions resulting in ruptured film)

The group of density profiles of water showing from Figure 2.11 to 2.14 demonstrates same features as that we summarized for the analysis of argon. As shown in Figure 2.13, using the density condition, Equation 2.71, to calculate the critical thickness, we obtain $\delta_c = 1.33$ nm for water at $T_r = 0.6$.

The half-interface free energy σ for each film molar loading thickness δ_{ml} is calculated by numerical integration on Equation 2.42 after deriving the density profiles. Summarized in Table 2.5 are the local density at the centerline $\hat{\rho}_{cl}$, non-dimensional half-interface free energy $\sigma/(P_c L_i)$, non-dimensional intra-spinodal sublayer thickness δ_{is}/L_i, non-dimensional interfacial region thickness δ_i/L_i (for thick film only, which represents interfaces between bulk phases), and the mean density film thicknesses δ_f for water.

Table 2.5
Calculated results for water at $T_r = 0.6$ for four typical δ_{ml} values

δ_{ml} (nm)	3.38	1.13	1.01	0.56
$\hat{\rho}_{cl}$ (mol/m^3)	37,186	31,319	28,769	18,455
$\sigma/(P_c L_i)$	4.72	4.60	4.47	3.69
δ_{is}/L_i	1.09	1.21	1.49	–
δ_i/L_i	1.30	–	–	–
δ_f (nm)	4.03	1.41	1.33	–

§ 2.6 SURFACE TENSION DEVIATION

As shown in Table 2.4 and 2.5, for both liquid argon films and water films, values of surface tension σ decrease with the decrease of film molar loading thickness δ_{ml}. As the film thickness approaches to the critical thickness, the surface tension value deviates significantly from its bulk value between bulk liquid phase and vapor phase under comparable conditions. This is somewhat analogous to the Tolman length associated with droplets of diminishing size [42], although here the change in surface tension is not due to curvature of the interface, but instead is a consequence of the interaction of the interfacial regions.

Figure 2.15 shows the variation of non-dimensional surface tension $\sigma/(P_c L_i)$ with the mean density film thickness δ_f for both argon and water at $T_r = 0.6$. More values of δ_{ml} are analyzed using the method described in previous section in order to obtain more data points in the plot.

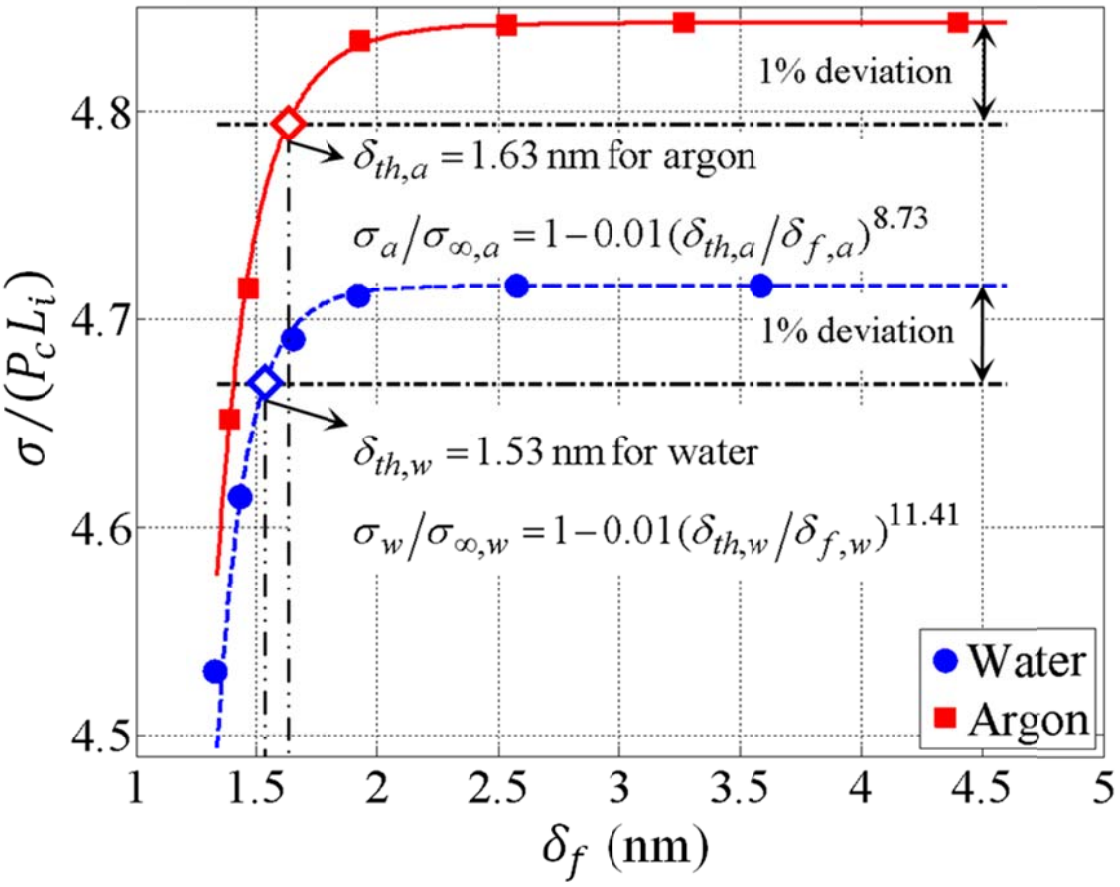

Figure 2.15 Variation of the half-interface free energy with film thickness at $T_r = 0.6$.

We define the threshold film thickness of surface tension deviation δ_{th} at which the half-interface free energy of the film decreases to 1% less than that for a semi-infinite body of liquid. At a reduced temperature of $T_r = 0.6$, the value of δ_{th} for argon is 1.63 nm and for water is 1.53 nm.

The study by Tolman [42] suggests that the deviation of the surface tension σ for a droplet due to its curvature effects can be described by:

$$\frac{\sigma}{\sigma_\infty} = \frac{1}{1 + 2\frac{r_T}{r_d}} = 1 - 2\left(\frac{r_T}{r_d}\right) + o\left(\frac{r_T}{r_d}\right) \tag{2.72}$$

in which, σ_∞ is the surface tension value between a bulk liquid phase and a bulk vapor phase, r_d is the droplet radius, and r_T is the characteristic Tolman length for a specified fluid. Other previous studies suggest that away from the critical point, the Tolman length of a specified fluid is on the order of its effective molecular diameter D. The numerical values of r_T reported in literatures are general in the range of $0.2D$ to $0.7D$. For a Lennard-Jones 12-6 fluid, Haye and Bruin [43] found that r_T/D is close to 0.2 for $0.696 \leq T_r \leq 0.835$. Since argon has an effective diameter of $D_{argon} = 0.188$ nm, this suggests the Tolman length of argon is about 0.038 nm. For water, Pruppacher and Klett [44] recommended a value of 0.157 nm for its Tolman length.

In contrast, the values of the threshold thickness δ_{th} showed in our study, which characterize the deviation of surface tension for a liquid film with thinning film thickness, are an order of magnitude greater than the corresponding effective molecular diameter for both argon and water. Also as shown in Figure 2.15, the dropping of the surface tension for a thinning film occurs more abruptly near the threshold thickness δ_{th} than that of a droplet with diminishing radius described by Equation 2.72. We therefore propose a function form, Equation 2.73, to curve-fit the theoretical predictions of the surface tension variation with thickness for use in further analysis.

$$\frac{\sigma}{\sigma_\infty} = 1 - B\left(\frac{\delta_{th}}{\delta_f}\right)^m \tag{2.73}$$

where, the coefficient $B = 0.01$ is dictated by the definition of δ_{th} described above. Values of the power constants m that best fit the predictions of argon and water at $T_r = 0.6$ are also given in Figure 2.15.

§ 2.7 EFFECT OF TEMPERATURE ON CRITICAL THICKNESS AND SURFACE TENSION

The same procedure for deriving the critical thickness and the surface tension used for both water and argon analysis at $T_r = 0.6$ is applied for other reduced temperatures from $T_r = 0.6$ to $T_r = 0.9$. The resulting variations of δ_c with temperature for argon and water, showing in Figure 2.16, indicate that the critical film thickness for both fluids increases as the system temperature increases.

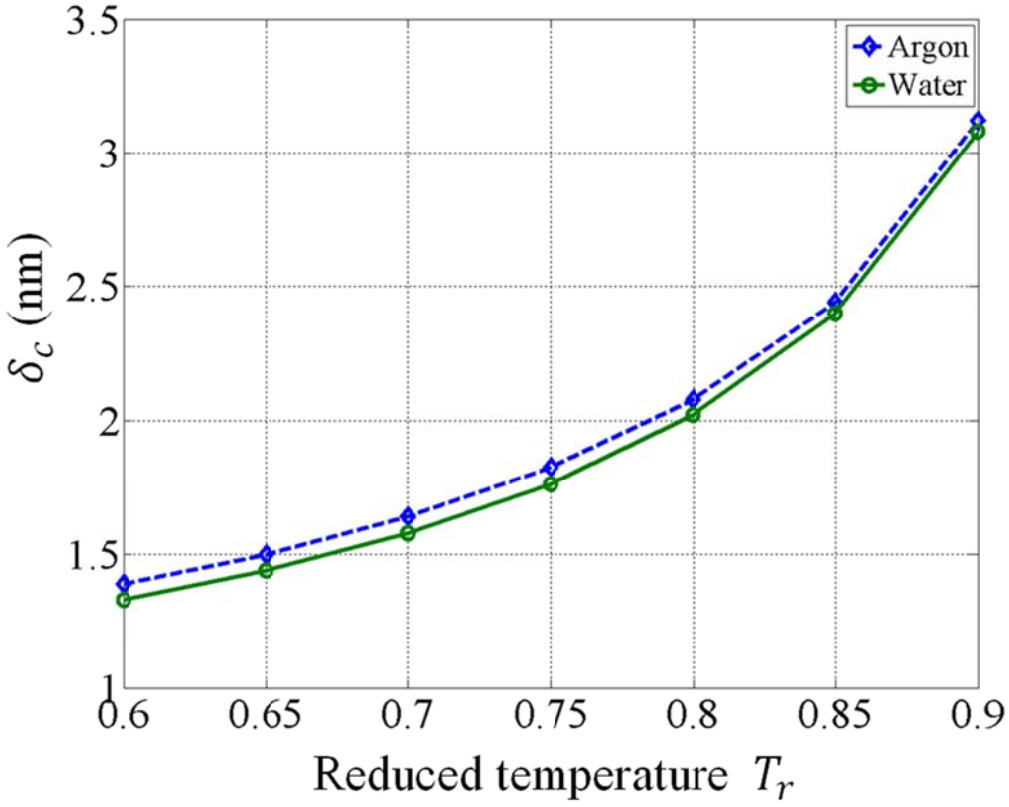

Figure 2.16 Variation of critical thickness δ_c with reduced temperature T_r for argon and water.

At other reduced temperatures, the surface tension values for argon and water films also show significant deviations from their bulk values when the film thickness drops below the threshold film thickness δ_{th}. Using the function form of Equation 2.73, we obtain values of the constants δ_{th} and m that best fit the predictions at different T_r for water and argon, as listed in Table 2.6.

Table 2.6
Surface tension deviation correlation constants at various reduced temperatures

	T_r	0.6	0.65	0.7	0.75	0.8	0.85	0.9
Argon	δ_c (nm)	1.39	1.50	1.64	1.83	2.08	2.44	3.12
	δ_{th} (nm)	1.63	1.76	1.96	2.22	2.57	3.06	3.81
	m	8.73	8.92	8.07	8.70	8.51	8.10	10.12
Water	δ_c (nm)	1.33	1.44	1.58	1.77	2.02	2.40	3.08
	δ_{th} (nm)	1.53	1.69	1.90	2.15	2.51	2.96	3.76
	m	11.41	9.12	8.59	8.09	7.69	8.36	9.48

§ 2.8 MODIFIED WAVE INSTABILITY MODEL

As noted in the introduction, earlier investigations have postulated that onset of film rupture is associated with conditions that result in amplifications of waves on the film interface. These wave instability models are based on implicit idealizations that the liquid-vapor interfacial region is a well-defined 2-D surface and the surface tension is a constant, presumably at bulk fluid value for the system temperature. However, the prediction of the film molecular capillarity model developed here indicates that the interfacial region between two phases has finite thickness, within which there is an intra-spinodal sublayer that lacks the intrinsic stability. As the film thickness decreases, the unstable intra-spinodal sublayers on both sides of a film span and interact with each other, causing a significant deviation of surface tension from its bulk value when the film thickness drops below the threshold film thickness δ_{th}. Eventually the unstable sublayers merge and destabilize the entire film core region, which can be a different mechanism for the onset of film rupture.

Therefore, we propose to extend the wave instability model of Vrij [4] in the following way to count for the effects of interactions between interfacial regions and the surface tension deviation with thinning film thickness. Assuming Equation 1.4 applies at the critical thickness, and substituting our curve-fit Equation 2.73 for the surface tension σ, we obtain the following relation for the critical thickness δ_c:

$$\delta_c = \left(\frac{A_H L^2}{4\pi^3 \sigma_\infty}\right)^{0.25} \left[1 - B\left(\frac{\delta_{th}}{\delta_c}\right)^m\right]^{-0.25} \tag{2.74}$$

Equation 2.74 can be solved iteratively to determine δ_c at different temperatures.

As shown in Equation 1.4 and Equation 2.74, both the original wave instability model of Vrij [4] and the modified wave instability model with surface tension correction account for the effect of the lateral dimension L of the liquid film on film stability. Because the lateral film size L is an upper bound to the wavelength of perturbing wave components that can exist on a film surface in wave instability models, the greater L is, the less stable a film will be, resulting the increase of critical thickness δ_c with the increase of L. In the film molecular capillarity model developed here, however, because intrinsic stability of the liquid in the film is independent on its lateral extent, the film's lateral dimension L does not affect the impact of this mechanism on film instability and rupture.

The variations of δ_c with L predicted by the original (uncorrected) and corrected versions of Vrij's wave instability model [4] are shown in Figure 2.17 and 2.18 for argon and water at $T_r = 0.6$ respectively. The Hamaker constant A_H in Equation 1.4 and Equation 2.74 is calculated by [45]:

$$A_H = \frac{3}{4} k_B T \left(\frac{\epsilon_{dielectric,v} - \epsilon_{dielectric,l}}{\epsilon_{dielectric,v} + \epsilon_{dielectric,l}}\right)^2 + \frac{3h\nu_e}{16\sqrt{2}} \cdot \frac{(n_v^2 - n_l^2)^2}{(n_v^2 + n_l^2)^{1.5}} \tag{2.75}$$

where, $\epsilon_{dielectric,v}$ and $\epsilon_{dielectric,l}$ are dielectric constants for saturated vapor and liquid, respectively [46,47], n_v and n_l are the refractive index for saturated vapor and liquid, respectively [47,48], and ν_e is the main electronic absorption frequency (typically 3×10^{15} s^{-1} for various materials [45]).

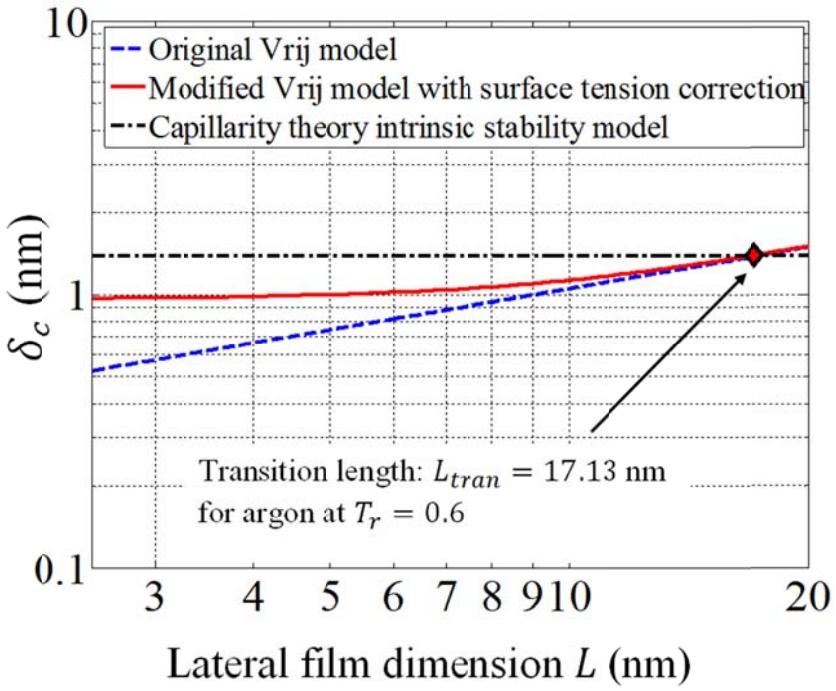

Figure 2.17 The transition lateral film dimension L_{tran} for argon at $T_r = 0.6$.

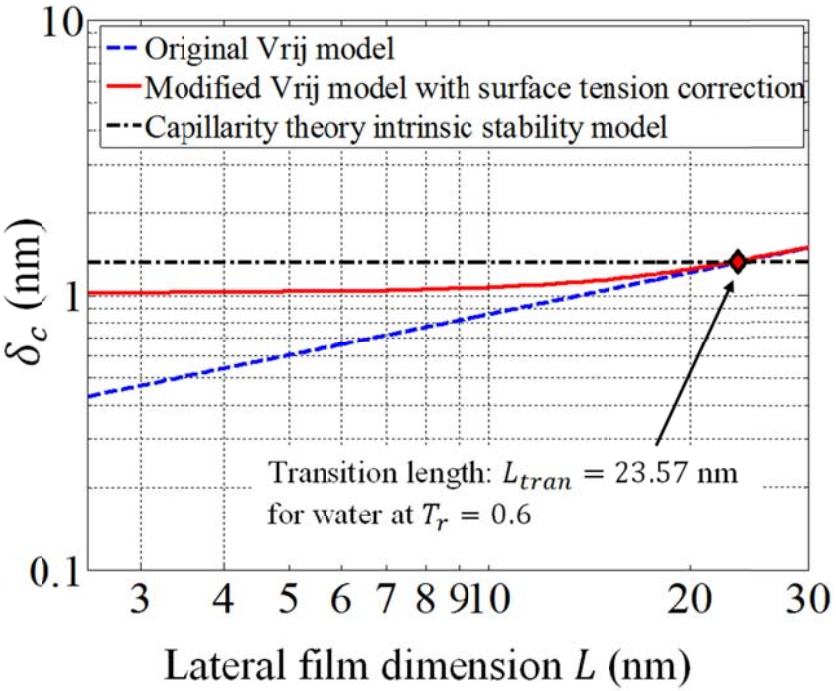

Figure 2.18 The transition lateral film dimension L_{tran} for water at $T_r = 0.6$.

The original Vrij's wave instability model predicts that the critical thickness δ_c is proportional to the square root of the lateral film dimension L, as indicated by Equation 1.4, therefore variations of δ_c with L are shown as inclined lines in the log-log plots of Figure 2.17 and 2.18 for argon and water. The prediction by the modified Vrij's wave instability model with surface tension correct shows less dependence of the critical thickness δ_c on the lateral film dimension L for small values of L, suggesting in this regime wave instability has less impact on the film stability than the interaction between interfacial regions does.

Also shown in Figure 2.17 and 2.18 is the characteristic transition length L_{tran}, at which lateral film dimension the critical thickness δ_c predicted by the wave instability model is the same as that predicted by our film molecular capillarity model. It can be seen that above the lateral size transition value L_{tran}, the critical film thickness predicted by the wave instability model are greater than that predicted by our capillarity model for the intrinsic stability mechanism. This implies that for $L > L_{tran}$, as a film becomes thinner it would become wave unstable first. For films with lateral extents smaller than L_{tran}, the critical film thickness for intrinsic stability is larger than that for wave instability, implying that as the film becomes thinner for this regime, it will likely rupture due to lack of intrinsic stability before wave instability occurs. The transition value of L_{tran} for the corrected wave instability model is slightly smaller than that for the original model of Vrij for constant surface tension. Since the corrected wave instability model takes both the wave instability and the interaction between interfacial regions into account and shows the consistent physics in its prediction of δ_c variation with L, we conclude that its predictions of L_{tran} are more accurate. The values of L_{tran} for argon and water are 17.13 nm and 23.57nm respectively.

Note that L_{tran} can be predicted by combining the critical thickness prediction of our film capillarity model with the corrected wave model, Equation 2.74. Figure 2.19 shows the variation of L_{tran} predicted in this way for water and argon. This plot implies that film rupture due to the lack of intrinsic stability in the film will likely be important only when the film has lateral dimensions less than 10 nm. While this is unlikely in macroscopic systems, for films in nano-channels, or films modeled with MD simulations of small lateral extent, the intrinsic stability mechanism may play a role in film rupture.

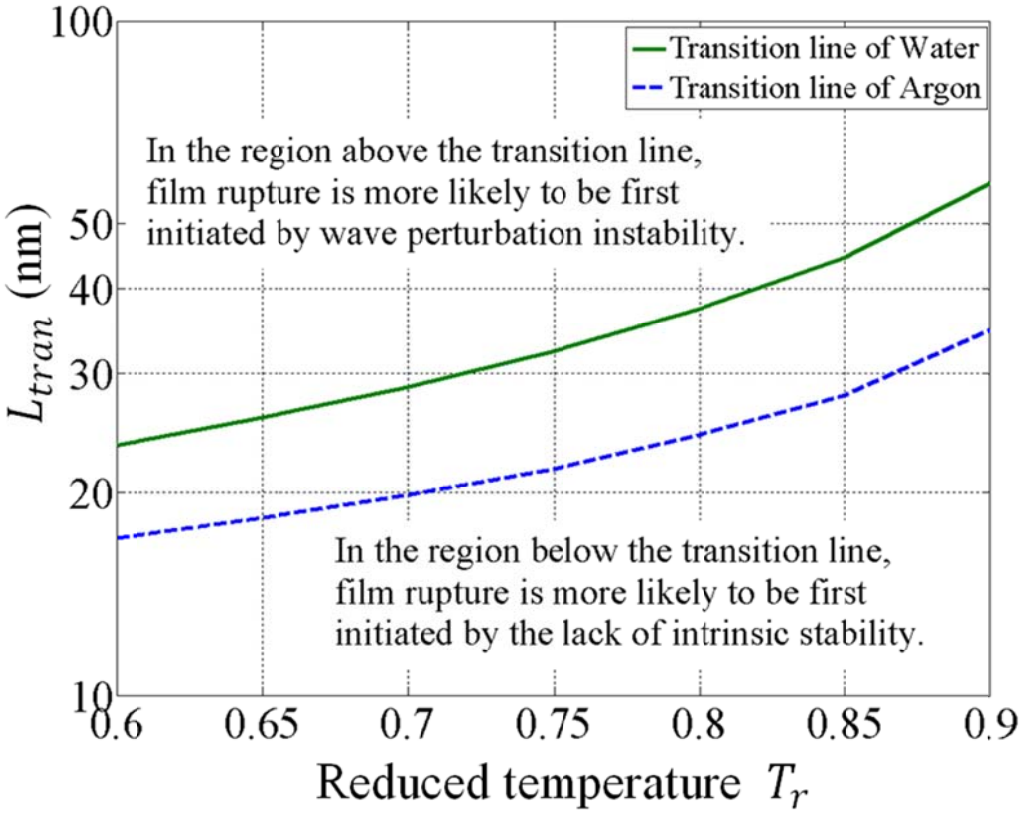

Figure 2.19 Variation of the transition lateral film dimension L_{tran} with reduced temperature T_r.

§ 2.9 SUMMARY

It has demonstrated in this chapter that the viability of extending classical molecular capillarity theory to a full free liquid film. This extension has been formulated for molecules that are well-modeled by a Lennard-Jones interaction potential, and applied to argon liquid films. We have also developed the extension of capillarity theory to liquid water films by incorporating an averaged form for the SPC/E interaction potential which accounts for the dipole character of water. This new approach to modeling liquid water films predicts half film excess free energy values for thick films that agree well with NIST recommended values of interfacial tension between bulk liquid and vapor water phases.

The capillarity theory provides closed form relations that predict the relationships among parameters that govern the film structure and thermophysical behavior and specifically the critical film thickness corresponding to incipient film rupture for a thinning film.

The prediction that surface tension diminishes as the film thickness decreases below a threshold value of film thickness is a key outcome of our model analysis. Although for argon and water at $T_r < 0.9$, the film thickness must drop to less than a few nanometers for surface tension reduction to be significant, this effect can be important, however, as the liquid film thins towards conditions for onset of rupture, or for bubbles of small physical size in, for example, nano-structured boiling surfaces. Therefore we propose that wave instability theory should be modified to account for the effects of surface tension reduction with film thickness in this range.

CHAPTER 3 – MD SIMULATIONS TECHNIQUES AND IMPLEMENTATIONS

This chapter outlines the techniques used in our MD model construction and simulation implementations. The initial conditions and the boundary conditions are first discussed. Potentials used for argon, water, and electrolyte aqueous solutions as well as the implementations of potentials in simulations are examined in details. Algorithms to advance the system in time and the simulation equilibrium criteria are provided subsequently. At the end of this chapter, methods of deriving macroscale statistical thermodynamic properties from MD simulations, such as the mean density and ion concentration profiles, pressure and surface tension, are presented to prepare for the next chapter's stability analysis of thin liquid films.

§ 3.1 POSITION INITIALIZATION

In order to investigate the stability of a liquid film, the MD system modeled in our simulations features two liquid-vapor interfacial regions, as shown in Figure 3.1.

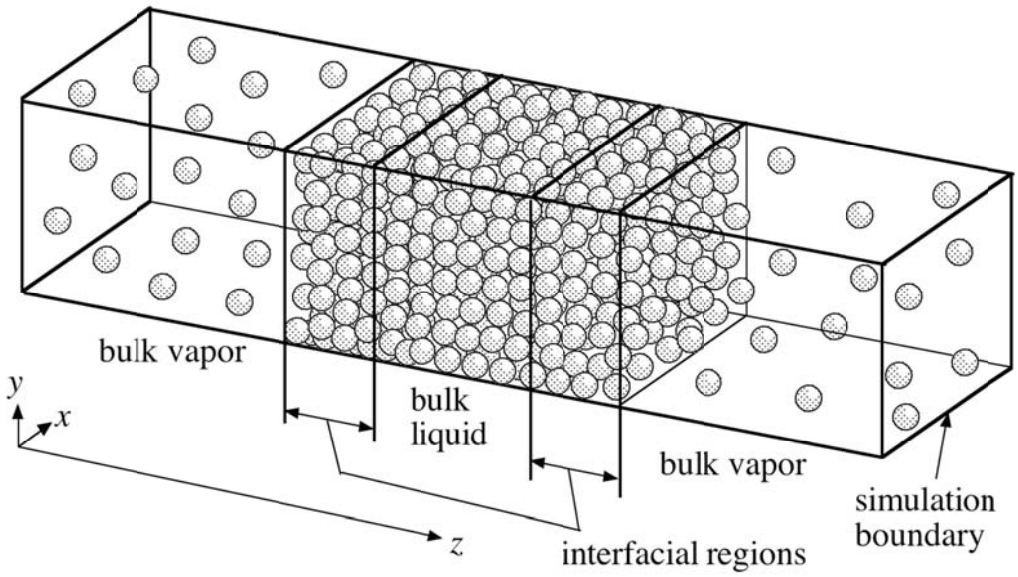

Figure 3.1 System illustration of liquid film bounded by its vapor on both sides

Initial configuration for monatomic fluid – Argon

A liquid argon film is initially positioned between two vapor phases via a face-centered-cubic (f.c.c) lattice structure, as shown in Figure 3.2. The dimension of each liquid or vapor lattice cell ($L_{lattice,l}$ or $L_{lattice,v}$) is determined respectively by the bulk liquid or bulk vapor molar density value at the specified temperature as:

$$L_{lattice,l} = \left(\frac{4}{\hat{\rho}_l N_A}\right)^{\frac{1}{3}} \tag{3.1a}$$

$$L_{lattice,v} = \left(\frac{4}{\hat{\rho}_v N_A}\right)^{\frac{1}{3}} \tag{3.1b}$$

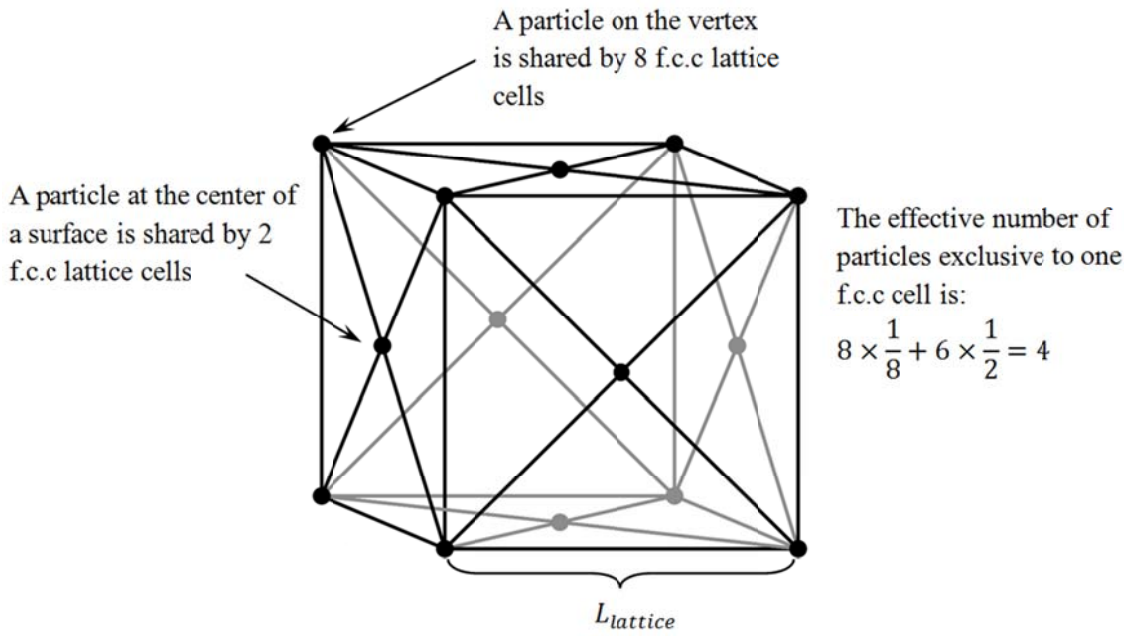

Figure 3.2 Face-centered-cubic (f.c.c) lattice structure used in the initial configuration

The numbers of liquid f.c.c lattice cells in x, y and z directions are represented by $n_{x,l}$, $n_{y,l}$ and $n_{z,l}$ respectively. $n_{x,l}$ and $n_{y,l}$ are set equal to represent the lateral size $L_{x,y}$ of a square segment of liquid film, which is also the lateral dimension of the simulation domain , as Equation 3.2:

$$L_{x,y} = n_{x,l} \times L_{lattice,l} \tag{3.2}$$

The number of vapor f.c.c lattice cells in x and y directions $n_{x,v}$ and $n_{y,v}$ are determined from the lateral size of the simulation domain $L_{x,y}$ as:

$$n_{x,v} = n_{y,v} = \left\lfloor \frac{L_{x,y}}{L_{lattice,v}} \right\rfloor \tag{3.3}$$

$n_{z,l}$, the number of liquid f.c.c lattice cells in z direction, dictates the characteristic molar loading thickness δ_{ml} of the liquid film:

$$\delta_{ml} = \frac{\hat{n}''}{\hat{\rho}_l} = n_{z,l} \times L_{lattice,l} \tag{3.4}$$

The dimension in the z direction for each side of the vapor phase, $L_{z,v}$, is set as $2 \times L_{x,y}$ in order to ensure independence of each liquid film in simulations with the periodic boundary condition. The number of vapor f.c.c lattice cells in z direction $n_{z,v}$ for each side of the vapor phase is determined as:

$$n_{z,v} = \left\lfloor \frac{2 \times L_{x,y}}{L_{lattice,v}} \right\rfloor \tag{3.5}$$

Therefore, the total simulation domain length in the z direction is:

$$L_z = (n_{z,l} + 4n_{x,l})L_{lattice,l} \tag{3.6}$$

Figure 3.3 provides a snapshot of the initial configuration for an argon MD simulation of 1188 molecules ($n_{x,l} = n_{y,l} = 7, n_{z,l} = 6$) at reduced temperature $T_r = 0.6$.

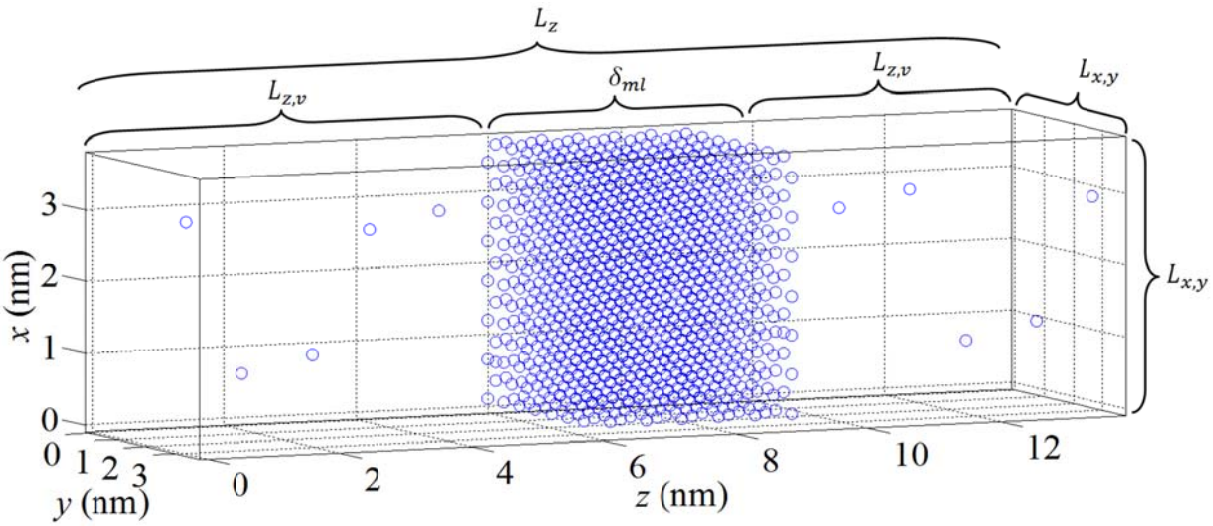

Figure 3.3 The initial configuration of argon MD simulation at $T_r = 0.6$ with 1188 molecules

Initial configuration for polyatomic fluid – Water

Centers of mass of water molecules are initially positioned in f.c.c lattice structures, in the same way as that for argon. For each water molecule, we use its center of mass as the origin and set the local molecular coordinate frame $\left(\overrightarrow{E_1}, \overrightarrow{E_2}, \overrightarrow{E_3}\right)$ as shown in Figure 3.4.

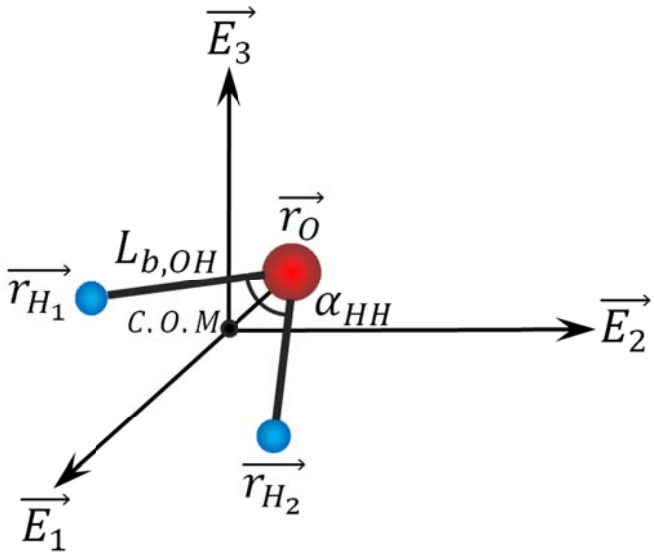

Figure 3.4 The local molecular coordinate frame with the molecular center of mass at origin.

Using the bond length $L_{b,OH}$ and bond angle α_{HH}, we are able to specify position vectors for the oxygen atom and two hydrogen atoms in this local molecular coordinate frame as:

$$\overrightarrow{r_{O,local}} = -\frac{1}{3}L_{b,OH}\cos\left(\frac{\alpha_{HH}}{2}\right)\cdot\overrightarrow{E_1} + 0\cdot\overrightarrow{E_2} + 0\cdot\overrightarrow{E_3} \tag{3.7a}$$

$$\overrightarrow{r_{H1,local}} = \frac{2}{3}L_{b,OH}\cos\left(\frac{\alpha_{HH}}{2}\right)\cdot\overrightarrow{E_1} - L_{b,OH}\sin\left(\frac{\alpha_{HH}}{2}\right)\cdot\overrightarrow{E_2} + 0\cdot\overrightarrow{E_3} \tag{3.7b}$$

$$\overrightarrow{r_{H2,local}} = \frac{2}{3}L_{b,OH}\cos\left(\frac{\alpha_{HH}}{2}\right)\cdot\overrightarrow{E_1} + L_{b,OH}\sin\left(\frac{\alpha_{HH}}{2}\right)\cdot\overrightarrow{E_2} + 0\cdot\overrightarrow{E_3} \tag{3.7c}$$

Each water molecule is then given a random initial orientation by choosing three random Euler's angles $\Omega = (\alpha_1, \alpha_2, \alpha_3)$ as shown in Figure 3.5 for a 3-1-3 configuration. The Euler's angles are used to rotate the local molecular coordinate frame $(\overrightarrow{E_1}, \overrightarrow{E_2}, \overrightarrow{E_3})$ into the global coordinate frame $(\overrightarrow{e_1}, \overrightarrow{e_2}, \overrightarrow{e_3})$.

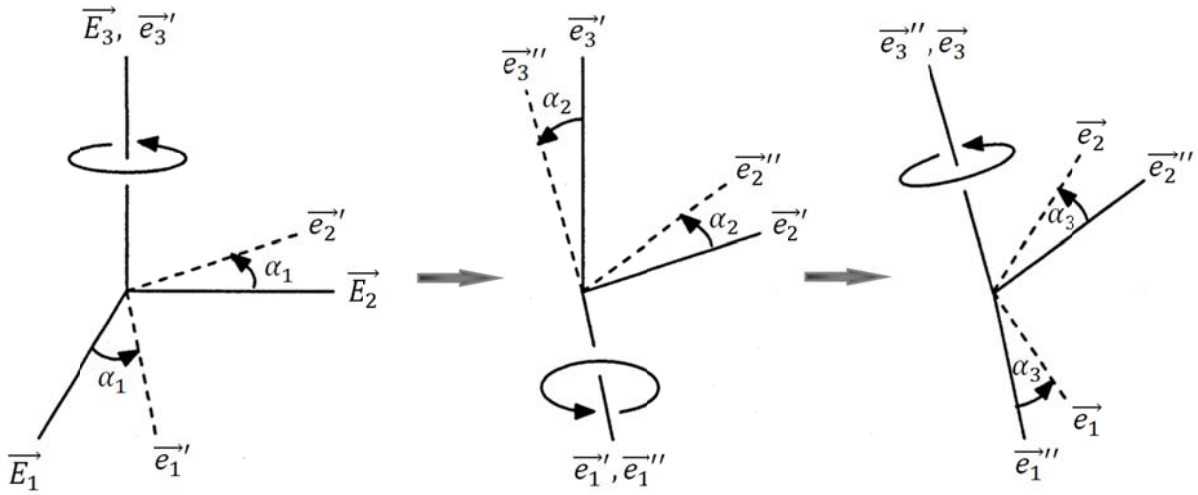

Figure 3.5 3-1-3 Euler's angle orientation of molecules using angles α_1, α_2 and α_3.

The rotational matrix [49] for applying the Euler's angles is given by:

$$Q = \begin{bmatrix} \cos\alpha_3 \cos\alpha_1 - \cos\alpha_2 \sin\alpha_1 \sin\alpha_3 & \cos\alpha_3 \sin\alpha_1 + \cos\alpha_2 \cos\alpha_1 \sin\alpha_3 & \sin\alpha_3 \sin\alpha_2 \\ -\sin\alpha_3 \cos\alpha_1 - \cos\alpha_2 \sin\alpha_1 \cos\alpha_3 & \cos\alpha_1 \cos\alpha_2 \cos\alpha_3 - \sin\alpha_3 \sin\alpha_1 & \cos\alpha_3 \sin\alpha_2 \\ \sin\alpha_2 \sin\alpha_1 & -\sin\alpha_2 \cos\alpha_1 & \cos\alpha_2 \end{bmatrix} \tag{3.8}$$

Applying the rotational matrix to the molecular coordinate frame gives a global position vector to each atom as:

$$\overrightarrow{r_{ia,global}} = \overrightarrow{r_{i,c.o.m}} + Q \cdot \overrightarrow{r_{ia,local}} \tag{3.9}$$

where, $\overrightarrow{r_{ia,global}}$ and $\overrightarrow{r_{ia,local}}$ are the position vector of atom a of molecule i in the global coordinate frame $(\overrightarrow{e_1}, \overrightarrow{e_2}, \overrightarrow{e_3})$ and the local molecular coordinate frame $(\overrightarrow{E_1}, \overrightarrow{E_2}, \overrightarrow{E_3})$ respectively, and $\overrightarrow{r_{i,c.o.m}}$ is the center of mass of molecule i in the global coordinate frame.

Figure 3.6 provides a snapshot of the initial configuration for a water MD simulation of 736 molecules ($n_{x,l} = n_{y,l} = 6, n_{z,l} = 5$) at reduced temperature $T_r = 0.65$.

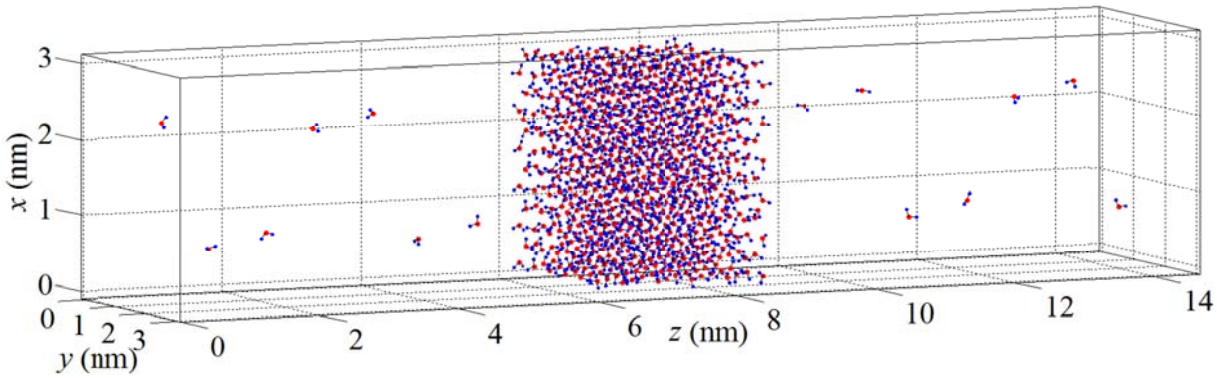

Figure 3.6 The initial configuration of water MD simulation at $T_r = 0.65$ with 736 molecules

Initial configuration for mixtures – Electrolyte aqueous solutions

In MD simulations for electrolyte aqueous solutions, water molecules are set in the same way as that for pure water simulations. Some liquid water lattice cells are randomly chosen to contain dissolved electrolyte ions. For each one of these lattice units, one solute ion (a Na^+ ion or a Cl^- ion for sodium chloride aqueous solution, as an example) is placed at the body center of that cell, as shown in Figure 3.7.

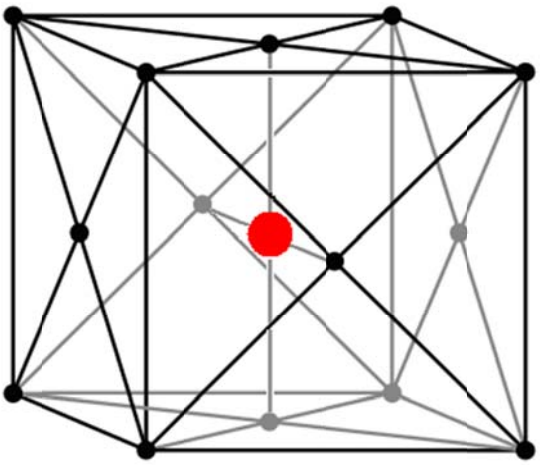

Figure 3.7 F.c.c lattice structure with a solute ion in its body center

As shown in Equation 3.10, the total number of liquid lattice cells $n_{ion-cell}$ having ions is determined by the solute concentration C_{solute} in M (mol/l), and the number of ions in each solute molecule n_{ion}. NaCl, for example, has $n_{ion} = 2$.

$$n_{ion-cell} = 4000 n_{ion} C_{solute} n_{x,l} n_{y,l} n_{z,l} \frac{1}{\hat{\rho}_l} \tag{3.10}$$

Figure 3.8 provides a snapshot of the initial configuration for 0.75 M (mol/l) NaCl aqueous solution MD simulation of 724 water molecules ($n_{x,l} = n_{y,l} = 6, n_{z,l} = 5$) and 15 NaCl solute molecules at reduced temperature $T_r = 0.6$.

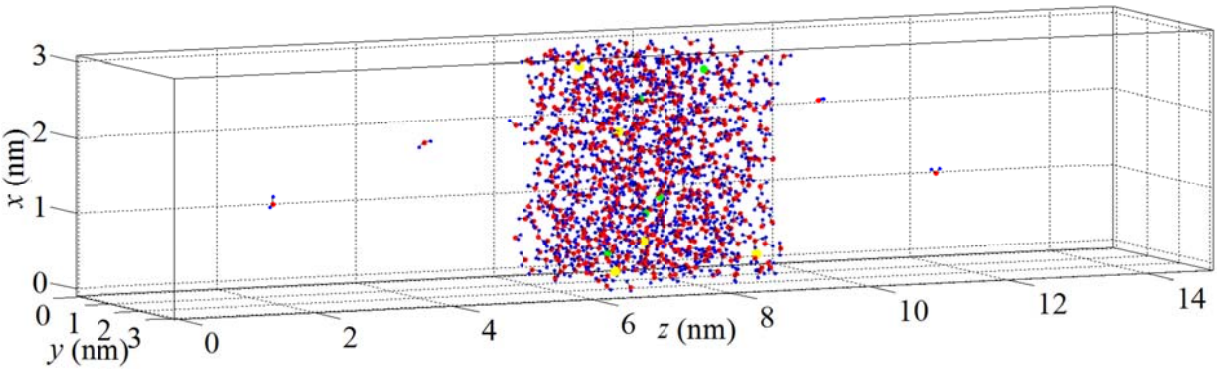

Figure 3.8 The initial configuration of 0.75 M NaCl MD simulation at $T_r = 0.6$. Green particles represent Na^+ ions and yellow particles represent Cl^- ions.

§ 3.2 VELOCITY INITIALIZATION

Velocity initialization is based on the Maxwell-Boltzmann distribution from kinetic theory and a technique developed by Box and Muller [50].

Velocity initialization for monatomic molecules and ions

For monatomic molecules and ions, we consider only the translational velocities. The Maxwell-Boltzmann velocity distributions in x, y and z directions are given by:

$$f(v_x) = \frac{1}{c_T\sqrt{2\pi}} e^{-\frac{v_x^2}{2c_T^2}} \tag{3.11a}$$

$$f(v_y) = \frac{1}{c_T\sqrt{2\pi}} e^{-\frac{v_y^2}{2c_T^2}} \tag{3.11b}$$

$$f(v_z) = \frac{1}{c_T\sqrt{2\pi}} e^{-\frac{v_z^2}{2c_T^2}} \tag{3.11c}$$

where, $f(v_x)dv_x$ is the probability that the x component of velocity lies between v_x and $v_x + dv_x$, and c_T is a characteristic velocity, defined as:

$$c_T = \sqrt{\frac{k_B T}{m}} \tag{3.12}$$

and m is the mass of the particle.

To apply this distribution in MD program, the following procedure is followed:

1. Generating two random number R_1 and R_2 in the range of [0,1]
2. Calculate two intermediate parameters ζ and θ as:

$$\zeta = \sqrt{-2\ln R_1} \tag{3.13}$$

$$\theta = 2\pi R_2 \tag{3.14}$$

3. Calculate the x and y components of velocity as:

$$v_x = \zeta c_T \cos\theta \tag{3.15}$$

$$v_y = \zeta c_T \sin\theta \tag{3.16}$$

4. Repeat step 1 through step 3 to determine v_z, neglecting the second component of the velocity in step 3.

Velocity initialization for polyatomic molecules

For polyatomic molecules, the translational component of velocity is initialized by the same method that is described above. The rotational kinetic energy of the molecule is determined by the rotational Boltzmann distribution [51]:

$$f(\epsilon_{rot}) = \frac{2\sqrt{\epsilon_{rot}}}{\sqrt{\pi}(k_B T)^{3/2}}\, e^{-\epsilon_{rot}/(k_B T)} \tag{3.17}$$

where ϵ_{rot} is the rotational energy, and $f(\epsilon_{rot})d\epsilon_{rot}$ is the fraction of molecules with rotational energies between ϵ_{rot} and $\epsilon_{rot} + d\epsilon_{rot}$.

To apply this distribution in MD program, the following flow chart of Figure 3.9 is used to determine the value of ϵ_{rot}.

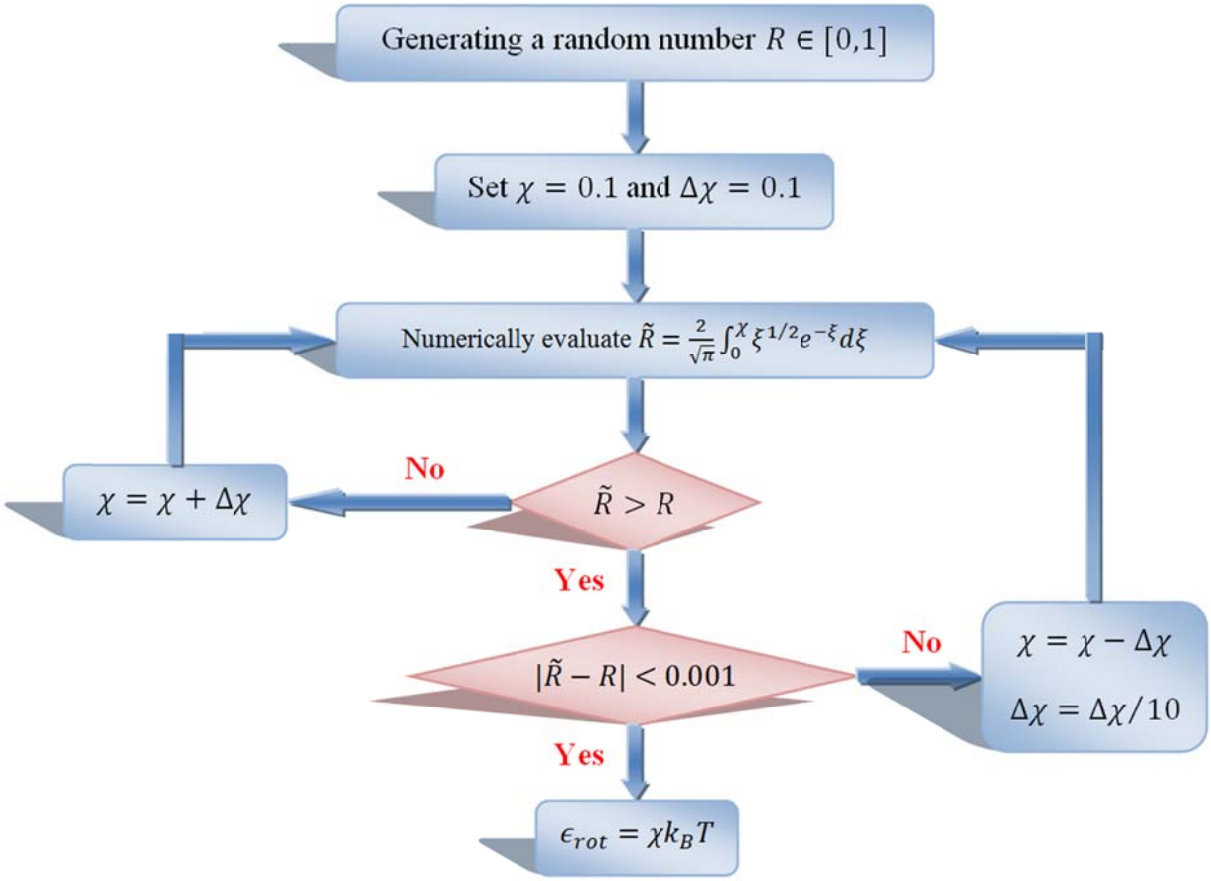

Figure 3.9 The flow chart used to determine the rotational kinetic energy of polyatomic molecule

Upon determining ϵ_{rot}, random numbers are assigned to determine the direction in which the rotational energy is applied. The rotational velocity in that direction is expressed as:

$$\omega_{\xi} = \sqrt{\frac{2\epsilon_{rot}}{I_{\xi\xi}}} \quad \xi = \{x, y, \text{or } z\} \tag{3.18}$$

in which, ξ represent the x, y or z direction, and $I_{\xi\xi}$ is the moment of inertia in the direction chosen.

§ 3.3 PERIODIC BOUNDARY CONDITION

Periodic boundary condition is applied by constructing infinite arrays of replicated simulation domains in x, y and z directions throughout space. Every particle in the original simulation domain has mirror image counterparts in all other replicated simulation domains, and changes in the original simulation domain are matched exactly in all other replica domains. As illustrated in Figure 3.10, any particle leaving one side of a simulation domain is automatically replaced by its counterpart in a neighboring domain entering through the opposite side. Consequently, the original simulation domain is devoid of any boundaries, and surface effects are eliminated.

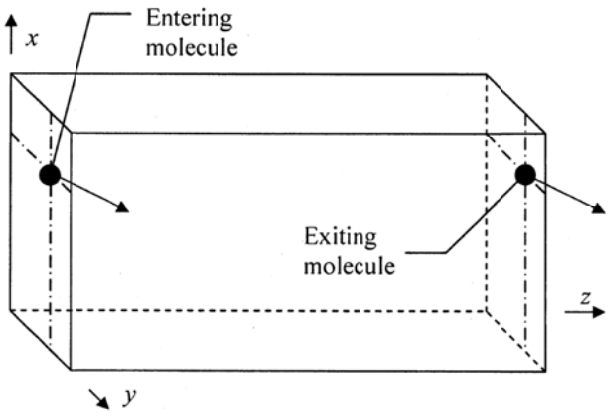

Figure 3.10 Schematic for periodic boundary condition

§ 3.4 POTENTIAL FUNCTIONS

Inter-particle potential functions are the core of MD simulations. The force upon an atom, a molecule, or an ion is determined by the potential function and the position configuration of the system in current time step, as:

$$\overrightarrow{F_i(\tau)} = -\sum_{j\neq i}^{N} \nabla\phi_{ij} \tag{3.19}$$

The Lennard-Jones 12-6 potential form is used for argon, and the extended simple point charge (SPC/E) potential form is used for water and ions. It should be noted that all potential models are empirical in nature, and their parameters are originally derived to match the interatomic radial distribution functions of experiment data as closely as possible.

Potential function for argon

The Lennard-Jones 12-6 potential function applied in MD simulations for argon is the same as that used in our film capillarity theory model, Equation 1.17, with the energy and length parameters, ϵ_{lj} and r_{lj}, from Table 2.2. The corresponding force vector on molecule i from the interaction with molecule j is:

$$\overrightarrow{F_{ij}} = -\frac{\overrightarrow{r_{ij}}}{r_{ij}}\frac{d\phi_{ij}}{dr_{ij}} = 24\frac{\epsilon_{lj}}{r_{lj}^2}\left(\frac{r_{lj}}{r_{ij}}\right)^8\left[2\left(\frac{r_{lj}}{r_{ij}}\right)^6 - 1\right]\overrightarrow{r_{ij}} \tag{3.20}$$

in which, r_{ij} is the distance between molecule i and j:

$$r_{ij} = \left|\overrightarrow{r_{ij}}\right| \tag{3.21}$$

The total potential energy of a system of N molecules is stated as:

$$U = \frac{1}{2}\sum_{i=1}^{N}\sum_{j\neq i}^{N}\phi_{ij} = 2\epsilon_{lj}\sum_{i=1}^{N}\sum_{j\neq i}^{N}\left[\left(\frac{r_{lj}}{r_{ij}}\right)^{12} - \left(\frac{r_{lj}}{r_{ij}}\right)^{6}\right] \tag{3.22}$$

However, because the periodic boundary condition is imposed on the MD simulations, the intermolecular interactions have to include not only those among the N molecules in the original simulation domain, but also those among the infinite array of periodic images. In order to avoid this difficulty, the potential cutoff method and the minimum image convention are used in simulations.

Since the short-range Lennard-Jones 12-6 potential of Equation 1.17 decays rapidly for distances beyond $3r_{lj}$, the cutoff radius is set as $r_{cut} = 3r_{lj}$. To calculate the interactions of molecule i, we use its position as the origin and draw a sphere of radius r_{cut}. Depending on the location of molecule i, the sphere may contain regions in both the original simulation domain and the replica simulation domains. Molecule i only interacts with other molecules falling within the sphere, either real molecules in the original simulation domain, or image molecules in the replica simulation domain. Interactions with molecules or image molecules outside of the sphere are neglected.

However, it should be noted that although the interactions beyond cutoff radius are insignificant, the inherent discontinuity of this cutoff method leads to a resultant impulse on the molecules near the cutoff distance, which may disrupt the simulation as reported in the studies of Mecke et *al*. [52] and Trokhymchuk and Alejandre [53]. Therefore, the force-shift truncation [54-57] is adopted in our MD simulations to implement the potential cutoff as:

$$\phi_{ij,f-s} = \phi_{ij} - \left(\phi_{ij}\right)_{r_{ij}=r_{cut}} - \left(\frac{d\phi_{ij}}{dr_{ij}}\right)_{r_{ij}=r_{cut}}\left(r_{ij} - r_{cut}\right) \tag{3.23}$$

$$\overrightarrow{F_{IJ,f-s}} = -\frac{\overrightarrow{r_{IJ}}}{r_{ij}}\frac{d\phi_{ij,f-s}}{dr_{ij}} = -\frac{1}{r_{ij}}\left[\frac{d\phi_{ij}}{dr_{ij}} - \left(\frac{d\phi_{ij}}{dr_{ij}}\right)_{r_{ij}=r_{cut}}\right]\overrightarrow{r_{IJ}} \tag{3.24}$$

The force-shift modified potential function $\phi_{ij,f-s}$ and force $\overrightarrow{F_{IJ,f-s}}$ both approach exactly zero at the cutoff distance, as $r_{ij} \to r_{cut}$.

Potential function for water and ions

The extended simple point charge (SPC/E) potential form is used for interactions among water molecules and various ions:

$$\phi_{i,j} = 4\epsilon_{spc/e,w-w}\left[\left(\frac{r_{spc/e,w-w}}{r_{ij}}\right)^{12} - \left(\frac{r_{spc/e,w-w}}{r_{ij}}\right)^{6}\right] + \frac{1}{4\pi\epsilon_0}\sum_{a=1}^{3}\sum_{b=1}^{3}\frac{q_a q_b}{r_{iabj}} \tag{3.25}$$

$$\phi_{i,\alpha} = 4\epsilon_{spc/e,w-ion}\left[\left(\frac{r_{spc/e,w-ion}}{r_{i\alpha}}\right)^{12} - \left(\frac{r_{spc/e,w-ion}}{r_{i\alpha}}\right)^{6}\right] + \frac{1}{4\pi\epsilon_0}\sum_{a=1}^{3}\frac{q_a q_\alpha}{r_{ia\alpha}} \tag{3.26}$$

$$\phi_{\alpha,\beta} = 4\epsilon_{spc/e,ion-ion}\left[\left(\frac{r_{spc/e,ion-ion}}{r_{\alpha\beta}}\right)^{12} - \left(\frac{r_{spc/e,ion-ion}}{r_{\alpha\beta}}\right)^{6}\right] + \frac{1}{4\pi\epsilon_0}\frac{q_\alpha q_\beta}{r_{\alpha\beta}} \tag{3.27}$$

in these relations, i, j represent water molecules, α, β represent ions, and subscripts a and b varying from 1 to 3 sequentially represent H-O-H atoms within water molecules. Also, ϵ and r with subscripts spc/e, and w or ion are respectively the energy parameter and length parameter in the SPC/E type interaction potentials, and ϵ_0 is the vacuum permittivity. In these relations, r with subscripts i, j, a, b, α or β is the distance between two interacting particles. If one of the interacting particles is a water molecule without the subscript a or b specifying an atom, the distance is measured based on the oxygen atom in that water molecule. q is the point charge assigned to a specified atom or ion. Values of these constants used in our MD studies are summarized in Table 3.1 [58-63].

Table 3.1
Constants of SPC/E form potential functions used in MD simulations for water and ions

$r_{spc/e,w-w}$	3.166×10^{-10} (m)	$\epsilon_{spc/e,w-w}$	1.080×10^{-21} (J)
$r_{spc/e,Na^+-Na^+}$	2.350×10^{-10} (m)	$\epsilon_{spc/e,Na^+-Na^+}$	9.033×10^{-22} (J)
$r_{spc/e,Ca^{2+}-Ca^{2+}}$	3.029×10^{-10} (m)	$\epsilon_{spc/e,Ca^{2+}-Ca^{2+}}$	8.657×10^{-22} (J)
$r_{spc/e,Cl^--Cl^-}$	4.400×10^{-10} (m)	$\epsilon_{spc/e,Cl^--Cl^-}$	6.957×10^{-22} (J)
$r_{spc/e,I^--I^-}$	4.168×10^{-10} (m)	$\epsilon_{spc/e,I^--I^-}$	8.661×10^{-22} (J)
$r_{spc/e,(ClO_4)^--(ClO_4)^-}$	3.604×10^{-10} (m)	$\epsilon_{spc/e,(ClO_4)^--(ClO_4)^-}$	1.060×10^{-21} (J)
$r_{spc/e,w-Na^+}$	2.758×10^{-10} (m)	$\epsilon_{spc/e,w-Na^+}$	9.915×10^{-22} (J)
$r_{spc/e,w-Ca^{2+}}$	3.097×10^{-10} (m)	$\epsilon_{spc/e,w-Ca^{2+}}$	9.727×10^{-22} (J)
$r_{spc/e,w-Cl^-}$	3.783×10^{-10} (m)	$\epsilon_{spc/e,w-Cl^-}$	8.877×10^{-22} (J)
$r_{spc/e,w-I^-}$	3.667×10^{-10} (m)	$\epsilon_{spc/e,w-I^-}$	9.729×10^{-22} (J)
$r_{spc/e,w-(ClO_4)^-}$	3.385×10^{-10} (m)	$\epsilon_{spc/e,w-(ClO_4)^-}$	1.070×10^{-21} (J)
$r_{spc/e,Na^+-Cl^-}$	3.375×10^{-10} (m)	$\epsilon_{spc/e,Na^+-Cl^-}$	7.995×10^{-22} (J)
$r_{spc/e,Na^+-I^-}$	3.259×10^{-10} (m)	$\epsilon_{spc/e,Na^+-I^-}$	8.847×10^{-22} (J)
$r_{spc/e,Na^+-(ClO_4)^-}$	2.977×10^{-10} (m)	$\epsilon_{spc/e,Na^+-(ClO_4)^-}$	9.816×10^{-22} (J)
$r_{spc/e,Ca^{2+}-Cl^-}$	3.714×10^{-10} (m)	$\epsilon_{spc/e,Ca^{2+}-Cl^-}$	7.807×10^{-22} (J)
q_H	0.4238 (e)	q_O	-0.8476 (e)
q_{Na^+}	1 (e)	$q_{Ca^{2+}}$	2 (e)
q_{cl^-} / q_{I^-}	-1 (e)	$q_{(ClO_4)^-}$	-1 (e)

As seen in Equation 2.35-2.37, the electrostatic portion of the SPC/E potential does not decay as rapidly as the Lennard-Jones potential (as r^{-1} versus r^{-6}). Therefore, the electrostatic potential cannot be truncated simply by the cutoff radius r_{cut}. Instead, the Ewald summation technique [64, 65 and 23], is applied in our MD simulations for handling the long-range interactions.

In the Ewald summation technique, a shielding charge distribution is placed on top of the point charges to reduce the error of the columbic potential and force calculation at the cutoff radius. The charge density of the shielding charge converted the dependence of the real-space potential to $\mathrm{erfc}(r)/r$, which decayed much more rapidly than the r^{-1} relationship in the original potential function. To neutralize the introduced shielding charge distribution, a compensating charge distribution is also added to the simulation. The periodicity of the compensating charge due to the periodic boundary condition allows for it to be handled by a Fourier analysis over the reciprocal lattices generated from repeating the simulation domain in all directions. Therefore, we divide the columbic potential into four components:

$$\phi_{columbic} = \phi^r + \phi^f - \phi^s - \phi^m \tag{3.28}$$

in which, ϕ^r is the potential induced by the coupling of the original point charges and the shielding charge distribution and is calculated in real-space; ϕ^f is the Fourier component stemming from the compensating charge distribution; the Fourier calculation of ϕ^f includes the self-interacting term ϕ^s among the compensating charge distribution, which is therefore subtracted from the overall potential; similarly, since ϕ^f also includes the interactions among the compensating charge distribution and the original point charges on the same molecule, this intra-molecular component ϕ^m is subtracted in Equation 3.28. Expressions of these four terms used in MD simulations are given as:

$$\phi^r = \frac{1}{4\pi\epsilon_0}\sum_{i=1}^{N}\sum_{a=1}^{N_{atom}}\sum_{j>i}^{N}\sum_{b=1}^{N_{atom}}\frac{q_{ia}q_{jb}}{r_{iabj}}\mathrm{erfc}\left(\kappa_w r_{iabj}\right) \tag{3.29}$$

$$\phi^f = \frac{1}{4\pi\epsilon_0}\cdot\frac{2\pi}{V}\cdot\sum_{k\neq 0}Q(k)\left|S\left(\vec{k}\right)\right|^2 \tag{3.30}$$

$$\phi^s = \frac{1}{4\pi\epsilon_0}\cdot\frac{\kappa_w}{\sqrt{\pi}}\cdot\sum_{i=1}^{N}\sum_{a=1}^{N_{atom}}q_{ia}^2 \tag{3.31}$$

$$\phi^m = \frac{1}{4\pi\epsilon_0}\cdot\frac{1}{2}\cdot\sum_{i=1}^{N}\sum_{a=1}^{N_{atom}}\sum_{b\neq a}\frac{q_{ia}q_{ib}}{r_{iab}}\mathrm{erfc}(\kappa_w r_{iab}) \tag{3.32}$$

where,

$$Q(k) = \frac{1}{k^2} e^{-\frac{k^2}{4\kappa_w^2}} \tag{3.33}$$

$$S(\vec{k}) = \sum_{i=1}^{N} \sum_{a=1}^{N_{atom}} q_{ia} e^{\mathrm{i}\cdot\vec{k}\cdot\overrightarrow{r_{ia}}} \tag{3.34}$$

From Equation 3.19, the corresponding force due the electrostatic portion of potential is then obtained as:

$$\overrightarrow{F_{ia}} = \overrightarrow{F_{ia}^{r}} + \overrightarrow{F_{ia}^{f}} \tag{3.35}$$

in which, $\overrightarrow{F_{ia}^{r}}$ and $\overrightarrow{F_{ia}^{f}}$ are the force components calculated in the real-space and the Fourier-space respectively:

$$\overrightarrow{F_{ia}^{r}} = \frac{q_{ia}}{4\pi\epsilon_0} \sum_{j\neq i}^{N} \sum_{b=1}^{N_{atom}} \frac{q_{jb}}{r_{iabj}^3} \left[\frac{2}{\sqrt{\pi}} \kappa_w r_{iabj} e^{-\kappa_w^2 r_{iabj}^2} + \mathrm{erfc}\left(\kappa_w r_{iabj}\right) \right] \overrightarrow{r_{iabj}} \tag{3.36}$$

$$\overrightarrow{F_{ia}^{f}} = -\frac{q_{ia}}{4\pi\epsilon_0} \frac{4\pi}{V} \sum_{k\neq 0} Q(k)\, \mathrm{Im}\left(e^{-\vec{k}\cdot\overrightarrow{r_{ia}}} S(\vec{k}) \right) \vec{k} \tag{3.37}$$

Note that the self-interacting term in Equation 3.28 does not provide an additional force on the molecules since its gradient is zero.

Above equations (Equation 3.29 to 3.37) use water molecules as examples to illustrate the MD implementation of the electrostatic portion of Equation 3.25. q_{ia} and $\overrightarrow{r_{ia}}$ are the charge value and position vector for atom a of water molecule i. For the electrostatic portions of Equation 3.26 and 3.27 (for interactions between water molecules and ions, and interactions among ions), q_{ia} and $\overrightarrow{r_{ia}}$ are replaced by q_α and $\overrightarrow{r_{\alpha\beta}}$ respectively to represent their counterparts of ions.

The vector $\vec{k}$ is the reciprocal lattice vector used in the Fourier space calculation:

$$\vec{k} = \frac{2\pi n_x}{L_x}\vec{x} + \frac{2\pi n_y}{L_y}\vec{y} + \frac{2\pi n_z}{L_z}\vec{z} \tag{3.38}$$

where, $\vec{x}$, $\vec{y}$ and $\vec{z}$ are unit vectors in the principal Cartesian directions, and n represents the number of repeated cells in a given direction. k in Equation 3.29-3.37 is the magnitude of $\vec{k}$: $k = |\vec{k}|$.

κ_w in Equation 3.29-3.37 is the shielding charge width, one of the key control parameters in the Ewald summation technique. κ_w together with the real-space cutoff radius r_{cut} and the Fourier cutoff number n_{cut} control the speed of convergence and the calculation accuracy in both the real-space and the Fourier-space in MD simulations. The process of determining these three parameters is discussed in detail by Frenkel and Smit [64], Kolafa and Perram [66].

For our non-cubic MD simulation configuration, the most accurate possible value for the real-space cutoff radius r_{cut} is half of the minimum length of the simulation domain:

$$r_{cut} = \frac{L_{min}}{2} = \frac{L_{x,y}}{2} \tag{3.39}$$

Frenkel and Smit [64] provided a relation for the value of κ_w that minimizes the computational cost:

$$\kappa_w = \frac{1}{L}\left(\frac{\tau_r \pi^3 N}{\tau_f}\right)^{1/6} \tag{3.40}$$

where, τ_r and τ_f are the computational time for each real-space and Fourier-space calculation respectively. In our simulations, $k_w = 5.6/L$ is found by Equation 3.40 to optimize the calculation speed.

Kolafa and Perram [66] discussed that the increase of calculation accuracy in Fourier-space decreases the accuracy in the real-space. Using the error analysis method, they proposed a relation among r_{cut}, κ_w and n_{cut} to balance the calculation accuracies in both spaces:

$$\kappa_w r_{cut} = \frac{\pi n_{cut}}{\kappa_w L} \tag{3.41}$$

Therefore, we can determine the Fourier cutoff number n_{cut} from r_{cut} and κ_w as:

$$n_{cut} = \frac{\kappa_w^2 L r_{cut}}{\pi} \tag{3.42}$$

Substituting the Fourier cutoff number n_{cut} into Equation 3.38, we obtain the magnitude of cutoff vector as:

$$k_{cut} = \frac{2\pi n_{cut}}{L} \tag{3.43}$$

In each step of MD simulations, the magnitudes of the Fourier vectors of reciprocal lattice points $|\vec{k}|$ are compared with k_{cut}. Only vectors of $|\vec{k}| < k_{cut}$ are considered in the energy calculation.

§ 3.5 ADVACING ALGORITHMS AND SIMULATION STAGES

In MD simulations, positions and velocities of all molecules are updated at each time step based on the applied intermolecular potentials. Algorithms of advancing the simulation in time adopted in our study are the velocity Verlet algorithm [67] for monatomic molecules and ions, and the RATTLE algorithm [68] for polyatomic molecules.

The velocity Verlet algorithm for monatomic molecules and ions

The major advantage of the velocity Verlet algorithm comparing to the original Verlet and the leap-frog Verlet algorithms is the ability to control the particles' velocities directly at each time step. It also contains less inherent numerical errors than the original Verlet algorithm, and conserves energy as well as the other two methods. Therefore, the velocity Verlet algorithm is applied in our MD simulations for monatomic molecules and ions.

The algorithm is implemented via the flow chart shown in Figure 3.11 for each particle in the system.

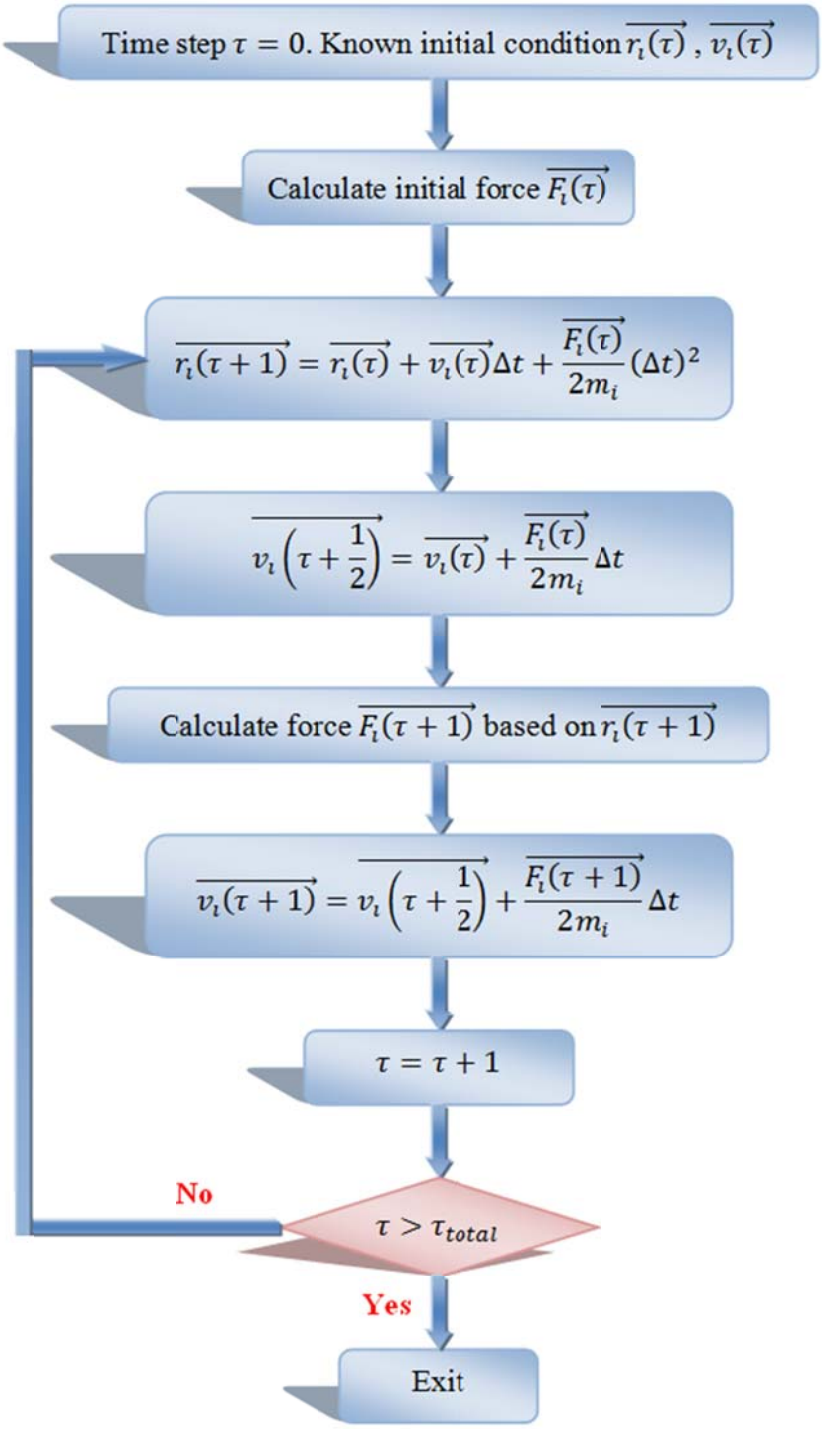

Figure 3.11 The flow chart of the velocity Verlet algorithm. Subscript *i* represents each monatomic molecule or ion in the simulation

The RATTLE algorithm for polyatomic molecules

Atoms in polyatomic molecules (water) feel both interatomic and constraint forces. Calculations of constraint force are difficult and computationally expensive. Therefore, the RATTLE algorithm is used for polyatomic molecules in order to avoid calculating constraint forces. The original version of SHAKE algorithm was devised by Ryckaert *et al*. [69] corresponding to the leap-frog Verlet algorithm. RATTLE was developed by Andersen [68] as an adaptation of the SHAKE algorithm to the velocity Verlet algorithm.

The RATTLE algorithm is implemented via the flow chart shown in Figure 3.12 for each water molecule in the system.

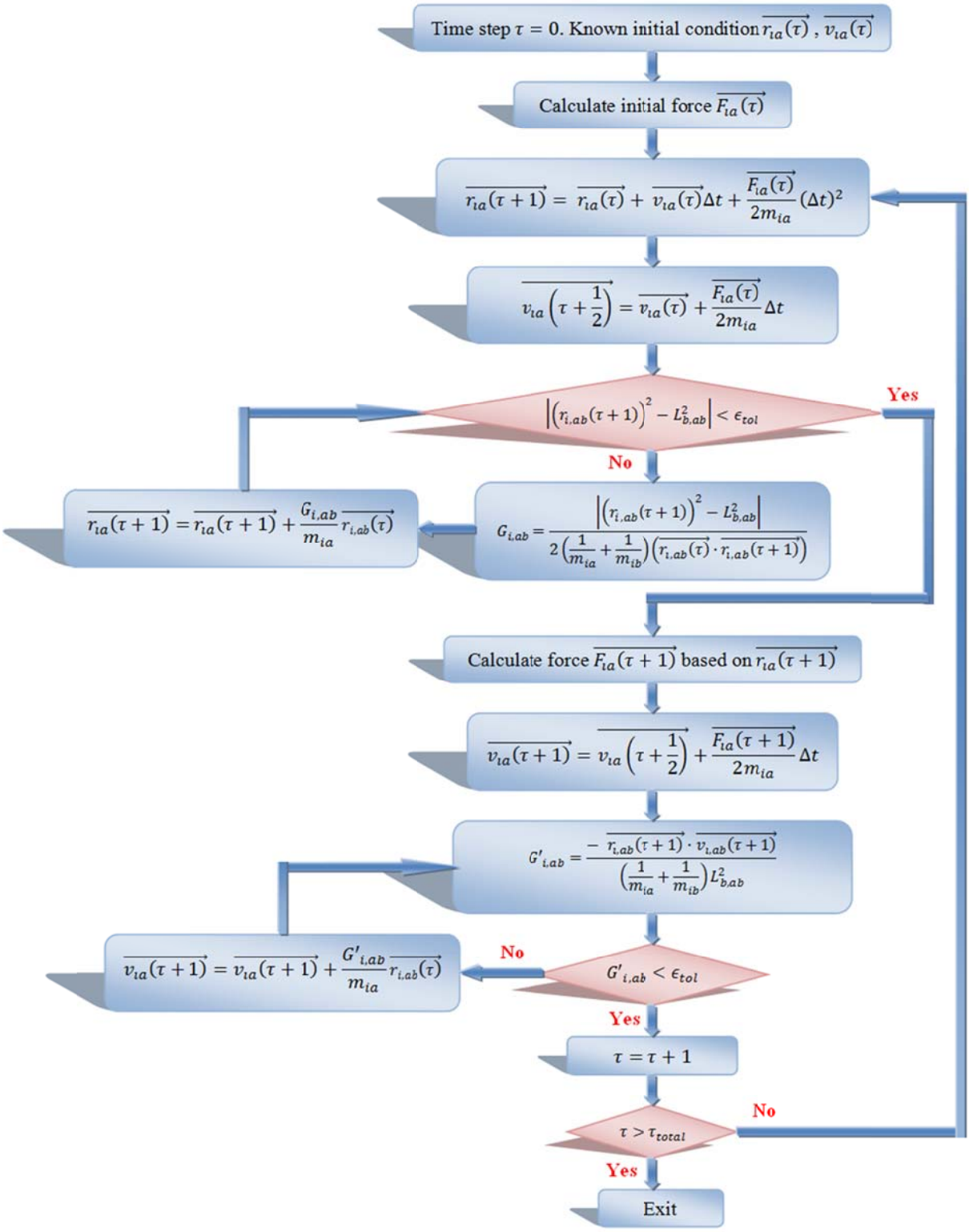

Figure 3.12 The flow chart of the RATTLE algorithm. Subscript i represents a molecule, a and b represent atoms in the molecule, and ϵ_{tol} is the specified tolerance.

Simulation stages

Although the molecular configuration is initialized such that the liquid and vapor regional densities match those for the bulk phases, the system did not begin in equilibrium. Therefore, before simulation results are collected, several simulation stages are taken to allow the system reaching equilibrium.

As shown in Figure 3.13, the total number of simulation steps is 80,000 and the system advances in time by 5 stages: the initial relaxation stage (stage I) of 1000 steps for releasing the extra potential energy in the initial lattice structure, the heating stage (stage II) of 19,000 steps for taking the system from an initially low temperature (10% of the desired temperature) to the target temperature, the constant temperature stage (stage III) of 10,000 steps using velocity rescaling to maintain the system temperature, the second relaxation stage (stage IV) of 20,000 steps with the temperature maintenance turning off, and the data collecting stage (stage V) of 30, 000 steps. The time step Δt is set as 5 fs except for the initial relaxation stage, which uses a time step of 0.5 fs to allow liquid molecules or ions to initially adjust in small steps. Interfacial free energy and statistical system temperature determined from systems statistics are monitored over time and mean values of both were steady during the statistical data collection stage of the simulation, indicating that the simulated system had reached thermodynamic equilibrium. Figure 3.14 shows the equilibrium statistical system temperature and interfacial free energy variations with time steps in a MD simulation for 0.36 M NaCl aqueous solution at $T_r = 0.65$.

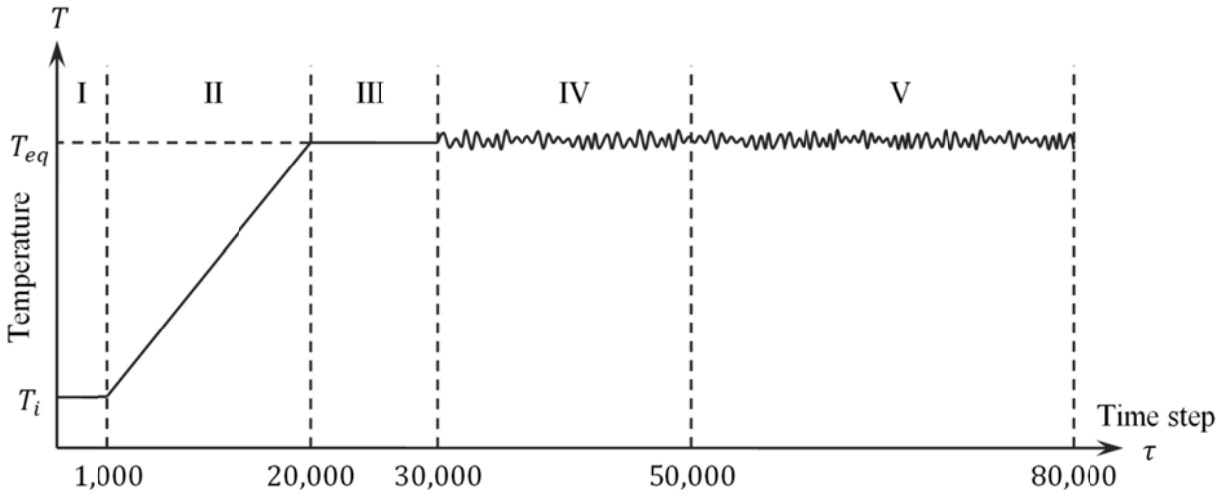

Figure 3.13 Schematic of various simulation stages

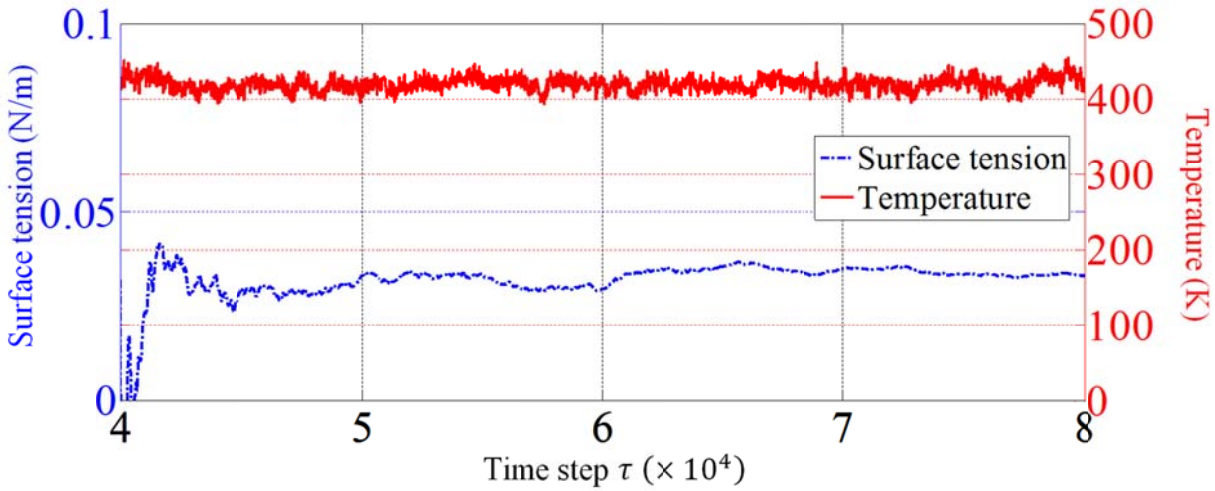

Figure 3.14 Surface tension and statistical temperature variations with time steps for a MD simulation (0.36 M NaCl aqueous solution with $n_{z,l} = 4$ at $T_r = 0.65$) reaching equilibrium.

Velocity and position adjustments

The velocity rescaling is used to control system temperature, either increasing the system temperature in simulation stage II, or maintain the constant temperature in stage III. The concept behind the velocity rescaling method lies in the kinetic theory definition of temperature:

$$\sum_{i=1}^{N} \frac{1}{2} m_i |\vec{v_i}|^2 = KE = \frac{\zeta}{2} N k_B T \tag{3.44}$$

where, ζ is the number of degrees of freedom for the simulating particle. The value of ζ for argon, water, ion are 3, 6 and 3 respectively. Therefore, at any instant in the simulation, the statistical system temperature is calculated by:

$$T_{calc} = \frac{1}{\zeta N k_B} \sum_{i=1}^{N} m_i |\vec{v_i}|^2 \tag{3.45}$$

To rescale the particle velocities such that they conform to a desired temperature $T_{desired}$, Equation 3.46 is applied to alter the velocities:

$$\overrightarrow{v_{i,adjusted}} = \vec{v_i}\sqrt{\frac{T_{desired}}{T_{calc}}} \tag{3.46}$$

Besides the velocity adjustment for the purpose of temperature control, the particles' position vectors need be adjusted for all simulation stages in order to remove the velocity bias. The random velocity distribution ideally provides no net momentum of the liquid layer in the z direction. However, the finite size of the simulation domain may accumulate the velocity bias from each time step, resulting in a small amount of z directional momentum. In order to ensure that the liquid film region remains in the center of the simulation domain, which is very important in the data collecting stage as we obtain results of density or ion concentration profiles, the particles' position vectors are adjusted at each time step.

Because the number of particles in the liquid region is much greater than that in the vapor region, we can safely approximate that the center of mass of the liquid film is equal to that of the entire simulation domain, which may be calculated as:

$$C.O.M_{z,calc}(\tau) = \frac{1}{N}\sum_{i=1}^{N} z_i\,(\tau) \tag{3.47}$$

For fixing the liquid film at the center of the simulation domain, the desired center of mass for the entire system should maintain the same as that from the previous time step:

$$C.O.M_{z,desired}(\tau) = C.O.M_z(\tau - 1) = \frac{1}{N}\sum_{i=1}^{N} z_i(\tau - 1) \tag{3.48}$$

Applying the position adjustment equally among all simulating particles to obtain the desired system center of mass, each position vector is altered according to Equation 3.49:

$$z_{i,adjusted}(\tau) = z_i(\tau) + \left(C.O.M_{z,desired}(\tau) - C.O.M_{z,calc}(\tau)\right) = z_i(\tau) + \frac{1}{N}\left(\sum_{i=1}^{N} z_i(\tau-1) - \sum_{i=1}^{N} z_i(\tau)\right) \quad (3.49)$$

§ 3.6 THERMODYNAMIC PROPERTIES CALCULATION

Several thermodynamic properties are collected during the data collecting stage for the purpose of film stability analysis, such as the local mass density, the local ion concentration, and surface tension. Some properties, like temperature, system total energy, are monitored in all simulation stages in order to make the program running smoothly. The statistical thermodynamics methods for calculating these properties based on MD simulation data are presented in this section.

Local mass density and ion concentration calculations

After equilibrium is reached, the simulation domain is divided into 100 bins along the z-axis (normal to the film interface), as shown in Figure 3.15. The local mass density data and the local ion concentration data (for electrolyte aqueous solutions) are collected in each bin at every step in the data collecting stage. The mass density of a bin k at time step τ, denoted as $\rho_{m,k}(\tau)$, is determined from the number of molecules in the bin $N_{m,k}(\tau)$ and the bin's volume V_k:

$$\rho_{m,k}(\tau) = \frac{mN_{m,k}(\tau)}{V_k} \quad (3.50)$$

where m is the molecular mass. For a polyatomic molecule, the position of the center of mass of that molecule is used to decide whether it belongs to the bin k or not. The time average local mass density $\rho_{m,k}$ is then calculated as the mean of $\rho_{m,k}(\tau)$ values over all time steps of the data collecting stage:

$$\rho_{m,k} = \langle \rho_{m,k}(\tau) \rangle_{\tau \in [50000,\ 80000]} \quad (3.51)$$

The ion concentration of the bin k at time step τ, denoted as $C_{i,k}(\tau)$, is determined in the similar way:

$$C_{i,k}(\tau) = \frac{N_{i,k}(\tau)}{1000 N_A V_k} \tag{3.52}$$

in which $N_{i,k}(\tau)$ is the number of ions in the bin k at time step τ. The time average local ion concentration is then calculated as:

$$C_{i,k} = \langle C_{i,k}(\tau) \rangle_{\tau \in [50000,\ 80000]} \tag{3.53}$$

The importance of minimizing system velocity bias discussed in the previous section is seen in the dividing of the domain into bins. Since positions of bins are fixed, erroneous data will be collected if the liquid region is to propagate in the z-direction as the simulation advancing in time.

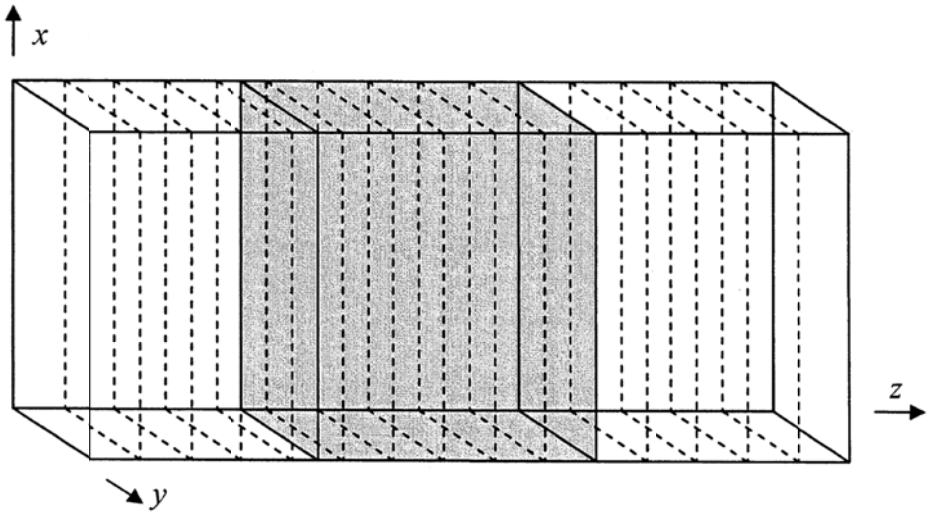

Figure 3.15 Density and ion concentration data collection bins in the simulation domain

Pressure and surface tension calculation for argon

The pressure for a monatomic fluid is calculated from the intermolecular forces and the system kinetic energy by [70]:

$$P = \frac{1}{3V}\sum_{i=1}^{N} m_i|\overrightarrow{v_i}|^2 + \frac{1}{3V}\sum_{i=1}^{N}\sum_{j>i}^{N} \overrightarrow{F_{ij}} \cdot \overrightarrow{r_{ij}} \tag{3.54}$$

Note that for an ideal gas, the intermolecular forces are zero everywhere except when the intermolecular distance is zero. Therefore, the dot product in the second term is zero everywhere. This modification, couple with Equation 3.45 for temperature, gives the well-known expression for an ideal gas,

$$PV = Nk_BT \tag{3.55}$$

In some MD simulation cases, values of local pressure are more concerned than the total pressure given by Equation 3.54. To obtain local pressure values, the simulation domain is divided into 100 bins along the z-axis (normal to the film interface), the same way as that used in collecting local density data shown in Figure 3.15. The expression used to calculate the local pressure $P(k)$ of bin k is proposed by Weng *et al*. [22] as:

$$P(k) = \frac{1}{3V_k}\sum_{i\,\in\,bin\,k} m_i|\overrightarrow{v_i}|^2 + \frac{1}{3V_k}\sum_{i=1}^{N}\sum_{j>i}^{N} f_{ijk}\overrightarrow{F_{ij}} \cdot \overrightarrow{r_{ij}} \tag{3.56}$$

The coefficient f_{ijk} represents the portion of the interaction between molecules i and j that falls in bin k. Figure 3.16 illustrate the determination of f_{ijk} in various scenarios:

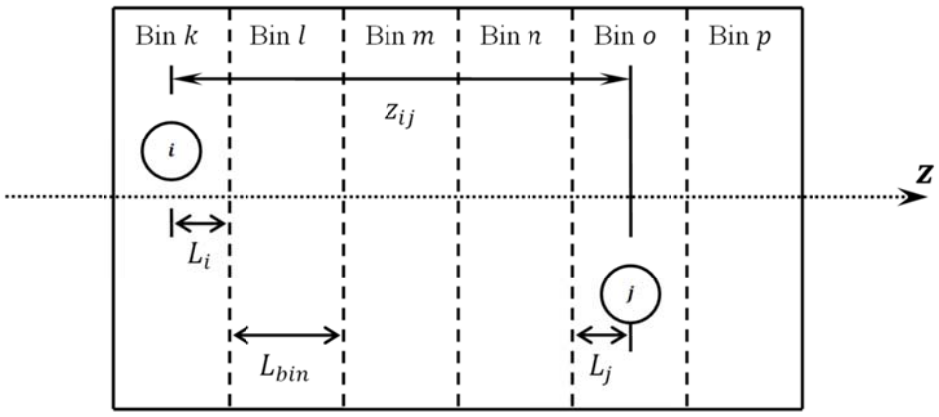

Figure 3.16 Determination of f_{ijk} for local pressure calculation

For the case of molecules i and j lying in the same bin k, all interactions between i and j lies in bin k and $f_{ijk} = 1$. For the case of molecules i and j lying in different bins, as shown in Figure 3.16, the pressure induced by the interaction between i and j is divided equally among bins according to the portion of the bin that is involved in the interaction. For example, bin k has $f_{ijk} = L_i/z_{ij}$; bin o has $f_{ijo} = L_j/z_{ij}$; bin m has $f_{ijm} = L_{bin}/z_{ij}$; and for bin p, since the connecting line between i and j does not cross it, f_{ijp} is assigned value of zero. This method provides more precise evaluations of local pressure values than the conventional method, in which if molecules i and j appears in different bins, half of the pressure calculated by Equation 3.54 is applied to each bin.

The surface tension values are calculated by the Virial method, integrating the difference between local normal and tangential pressure components through the entire simulation domain:

$$\sigma = \frac{1}{2}\int_{-\infty}^{\infty} [P_n(z) - P_t(z)]\ dz = \frac{1}{2}\sum_{k=1}^{100} [P_n(k) - P_t(k)] \tag{3.57}$$

The factor $1/2$ is applied since two liquid-vapor interfaces exist in our MD simulations.

The local pressure tensor is broken down into Cartesian components using the form:

$$P_\xi(k) = \frac{1}{V_k}\sum_{i\,\in\,bin\ k} m_i v_{i,\xi}^2 + \frac{1}{V_k}\sum_{i=1}^{N}\sum_{j>i}^{N} f_{ijk} F_{ij,\xi} r_{ij,\xi} \quad \xi = \{x, y, \text{or } z\} \tag{3.58}$$

Since in our MD simulation configurations, the normal to the film interface is in z direction, the normal pressure component points in the z direction and the tangential pressure component is the average of x and y direction pressure values. Therefore, $P_n(k)$ and $P_t(k)$ in Equation 3.57 are calculated as:

$$P_n(k) = \frac{1}{V} \sum_{i \in bin\ k} m_i v_{i,z}^2 + \frac{1}{V} \sum_{i=1}^{N} \sum_{j>i}^{N} f_{ijk} F_{ij,z} r_{ij,z} \tag{3.59}$$

$$P_t(k) = \frac{1}{2V} \sum_{i \in bin\ k} m_i \left(v_{i,x}^2 + v_{i,y}^2\right) + \frac{1}{2V} \sum_{i=1}^{N} \sum_{j>i}^{N} f_{ijk} \left(F_{ij,x} r_{ij,x} + F_{ij,y} r_{ij,y}\right) \tag{3.60}$$

Pressure and surface tension calculation for water and electrolyte aqueous solutions

In our MD simulations, the center-of-mass approximation proposed by Ciccotti [71] is used for polyatomic fluid, water. In this approximation, all interatomic forces are assumed to act on the center of mass of the molecule. The calculation for pressure using this approximation is:

$$P = \frac{1}{3V} \sum_{i=1}^{N} m_{m,i} \left|\overrightarrow{v_{m,i}}\right|^2 + \frac{1}{3V} \sum_{i=1}^{N} \sum_{j>i}^{N} \left(\sum_{a=1}^{N_{atom}} \sum_{b=1}^{N_{atom}} \overrightarrow{F_{iabj}} \cdot \overrightarrow{r_{iabj}} \right) \tag{3.61}$$

where $m_{m,i}$ is the molecular mass and $\overrightarrow{v_{m,i}}$ is the center of mass velocity vector for molecule i; $\overrightarrow{r_{ij}}$ is the vector between the centers of mass of molecule i and j, and $\overrightarrow{F_{iabj}}$ is the force vector between atom a on molecule i and atom b on molecule j.

Incorporation of the Ewald sum technique into Equation 3.61 is required in order to handle the electrostatic portion of interactions. Alejandre *et al.* [23] provided relations for the columbic contribution to pressure in the Cartesian coordinate system:

$$P_\xi = \frac{1}{8\pi\epsilon_0 V}\sum_{i=1}^{N}\sum_{a=1}^{N_{atom}}\sum_{j\neq i}^{N}\sum_{b=1}^{N_{atom}} q_{ia}q_{jb}\left[\frac{2}{\sqrt{\pi}}\kappa_w r_{iabj}e^{-\kappa_w^2 r_{iabj}^2} + \mathrm{erfc}\left(\kappa_w r_{iabj}\right)\right]\frac{r_{ij,\xi}r_{iabj,\xi}}{r_{iabj}^3}$$
$$+\frac{1}{4\pi\epsilon_0}\frac{2\pi}{V^2}\sum_{k\neq 0} Q(k)\left|S\left(\vec{k}\right)\right|^2\left(1-\frac{2k_\xi^2}{k^2}-\frac{k_\xi^2}{2\kappa_w^2}\right) \qquad (3.62)$$
$$-\frac{1}{V}\sum_{i=1}^{N}\sum_{a=1}^{N_{atom}}\left[\left(\overrightarrow{r_{ia}}-\vec{r}_i\right)\left(\overrightarrow{F_{ia}^f}\right)\right]_\xi \qquad \xi = \{x, y, \text{or } z\}$$

where $Q(k)$, $S\left(\vec{k}\right)$ and $\overrightarrow{F_{ia}^f}$ are given by Equation 3.33, 3.34 and 3.37 respectively.

Equations 3.61 and 3.62 use water molecules as an example to illustrate the MD implementation of the pressure calculation. For electrolyte aqueous solutions, interactions among water molecules and dissolved ions need be included in Equation 3.61 and 3.62. The subscripts of i, j, a, b are replaced by α, β accordingly to represent the counterparts for ions in the above equations.

Surface tension is calculated using Equation 3.57 in the same manner as for the monatomic system of argon. In MD simulations, the integral in Equation 3.57 is carried out across the simulation domain. Therefore, for simulations which only yield total pressure values without local pressure results in individual bins, the surface tension of Equation 3.57 can be approximated as:

$$\sigma = \frac{1}{2}\left[P_z - \frac{1}{2}\left(P_x + P_y\right)\right] \qquad (3.63)$$

§ 3.7 SUMMARY

In this chapter the fundamentals of MD implementation of a system incorporating liquid-vapor interfacial regions have been discussed. The initialization process provided molecules in a f-c-c lattice structure for both the liquid and vapor regions with velocities matching the Maxwell-Boltzmann distribution. Periodic boundary conditions are applied to eliminate surface effects due to limited dimensions of simulation domain. For monatomic molecule argon, the Lennard-Jones 12-6 potential function is used to calculate the intermolecular interactions. For polyatomic molecule water and various dissolved electrolyte ion, SPC/E type of potential functions are used in MD simulations. The long-range electrostatic portion of SPC/E potential is handled by the

Ewald summation technique in both real-space and Fourier-space. The velocity Verlet and RATTLE algorithms are used to advance the simulation in time for systems with and without intra-molecular constraint forces respectively. This chapter is ended by the discussion of deriving macroscale statistical thermodynamic properties from MD simulations, such as the mean density and ion concentration profiles, pressure and surface tension, based on which the stability of thin liquid film is analyzed.

CHAPTER 4 – STABILITY ANALYSIS BY MD SIMULATIONS

MD simulations of free thin liquid films have been carried out for systems consisting of argon, water and various electrolyte aqueous solutions. The stability of thin liquid films is studied using the thermodynamic intrinsic stability criteria and density profiles derived from MD simulations. Effects of film thickness, system temperature and electrolyte concentration on film stability are investigated by series of MD simulations with specified system variables. Also discussed are the surface tension of liquid-vapor interfacial regions and the relations of surface tension with film thickness, system temperature, electrolyte species and dissolved ion concentration profile.

§ 4.1 DENSITY PROFILES AND CRITICAL THICKNESSES

In the data collecting stage of MD simulations, local density data are collected in each bin at every time step. Time averaged mean values are obtained for each bin at the end of simulations. Figure 4.1, 4.2 and 4.3 show the mean density profiles predicted by the simulations of argon, pure water and 0.38 M (mol/l) NaCl aqueous solution respectively. In these simulations, the system reduced temperature is set as $T_r = 0.6$, the lateral film dimension for argon is fixed as $L_{x,y} = 3.83$ nm ($n_{x,l} = n_{y,l} = 7$), for water and NaCl aqueous solution $L_{x,y} = 2.48$ nm ($n_{x,l} = n_{y,l} = 5$), the film molar loading thickness for argon varies from 0.55 nm to 3.83 nm ($n_{z,l} = 1\sim7$), and for water and NaCl aqueous solution the film molar loading thickness varies from 0.50 nm to 2.48 nm ($n_{z,l} = 1\sim5$), as shown in these Figures respectively.

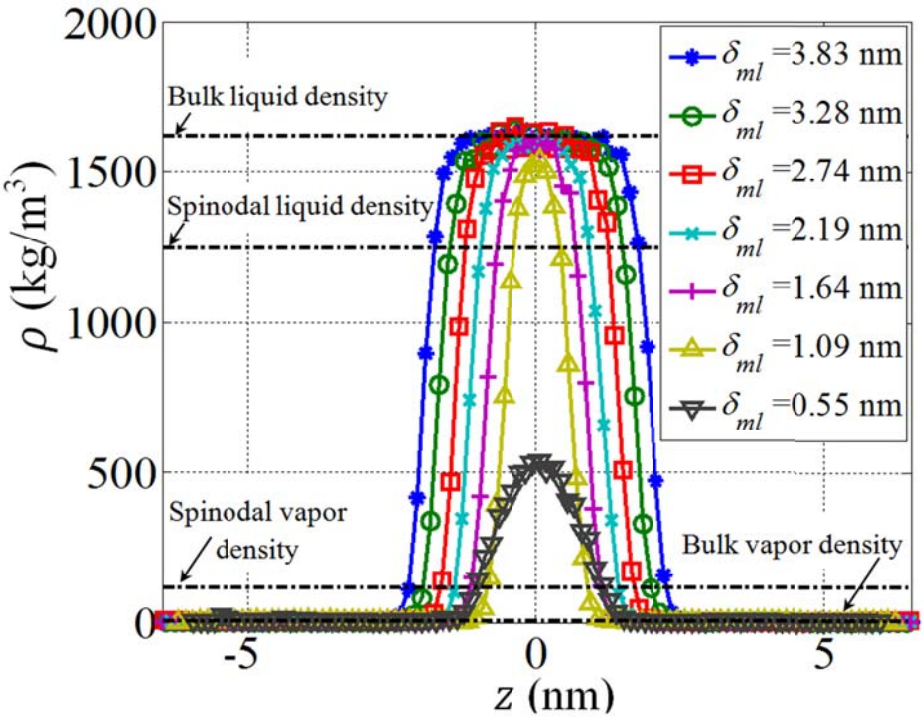

Figure 4.1 Time-averaged density profiles predicted by MD simulations for argon at $T_r = 0.6$

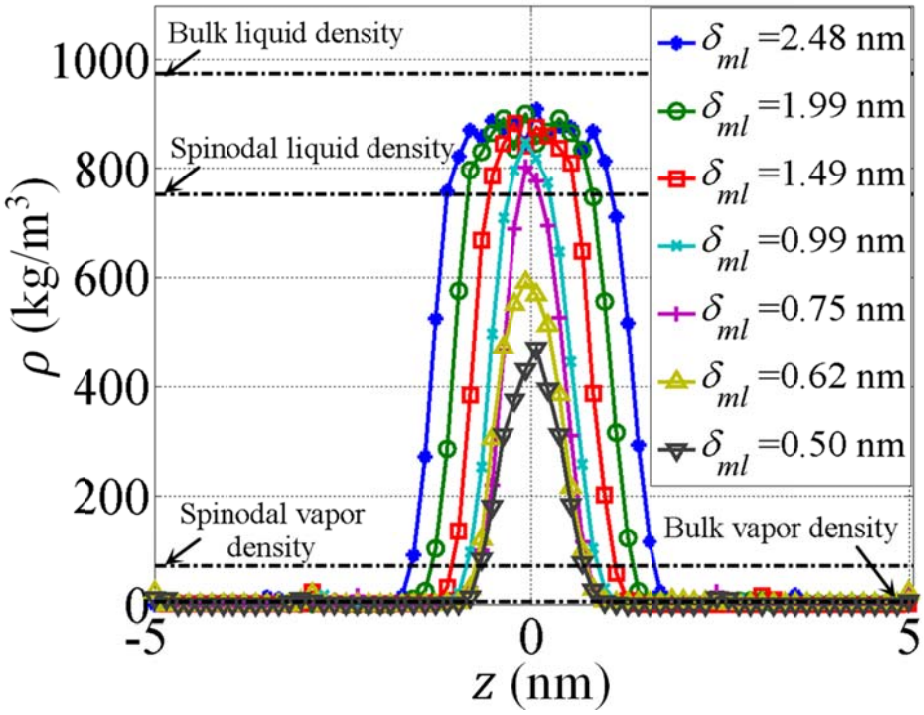

Figure 4.2 Time-averaged density profiles predicted by MD simulations for pure water at $T_r = 0.6$

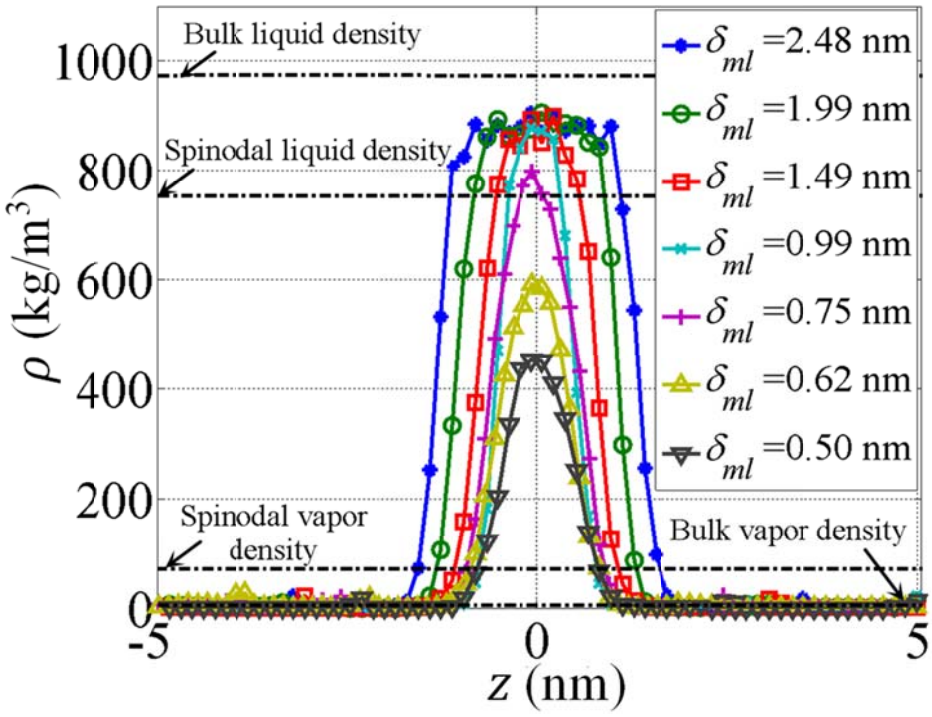

Figure 4.3 Time-averaged density profiles predicted by MD simulations for 0.38 M NaCl aqueous solution at $T_r = 0.6$

The four horizontal lines shown in the above three plots represent bulk liquid density ρ_l, spinodal liquid density $\rho_{spinodal,l}$, spinodal vapor density $\rho_{spinodal,v}$ and bulk vapor density ρ_v from the top to the bottom respectively. The bulk density values and spinodal density values are calculated using the Redlich-Kwong equation of state, as shown in Equation 2.4a. In Figure 4.3, for dilute NaCl solutions, although the presence of Na^+ ions and Cl^- ions has noticeable effect on the density distribution in the system, it shall not significant affect the numerical value of local density in an individual bin. Therefore, density profiles showing in Figure 4.3 only take account of the water molecules, and the bulk densities and spinodal densities calculated by the Redlich-Kwong equation of state for pure water are reasonable estimations for dilute NaCl aqueous solutions as well.

Density profiles derived from MD simulations show inherent fluctuations, however the overall density distributions for argon, pure water and electrolyte dilute aqueous solutions present consistent features as those derived by our film capillarity theoretical model previously. For thick liquid films, density profiles have discernible different regions for the vapor phase, the central liquid phase and liquid-vapor interfaces. In liquid-vapor interfacial regions, density profiles exhibit steep gradient at the edges of the film. Also as shown in Figure 4.1, 4.2 and 4.3, with the decrease of the film molar loading thickness δ_{ml}, the mean density within the central core region $\overline{\rho_{cc}}$ decreases.

In MD models, the definition of the mean film thickness δ_f is based on the density profile as well:

$$\delta_f = z_r - z_l \tag{4.1}$$

where, z_l and z_r are the z coordinates at which the local density in the interfacial region is equal to the mean value of $\overline{\rho_{cc}}$ and ρ_v:

$$\rho(z)|_{z=z_l<0} = \rho(z)|_{z=z_r>0} = \frac{\rho_v + \overline{\rho_{cc}}}{2} \tag{4.2}$$

Comparing the definitions of δ_f in the film capillarity model (Equation 2.66 and 2.67) and in MD simulation model, we notice that $\hat{\rho}_{cl}$ in Equation 2.67 is replaced by $\overline{\rho_{cc}}$ in Equation 4.2. Due to the fluctuating nature of MD simulations, using the mean density of the central core region is more reasonable than using the local density of a single bin containing the center line of simulation domain. In general, δ_f derived from MD simulation results also differ from the film molar thickness δ_{ml}.

Showing in Figure 4.4, 4.5 and 4.6 are the variation of $\overline{\rho_{cc}}$ with the film thickness δ_f for argon, pure water and 0.38 M NaCl aqueous solution respectively. Each data point in Figure 4.4 to 4.6 corresponds to a density profile as those shown in Figure 4.1 to 4.3, and the connecting lines between data points are drawn by curve fitting in order to show the trends of variations.

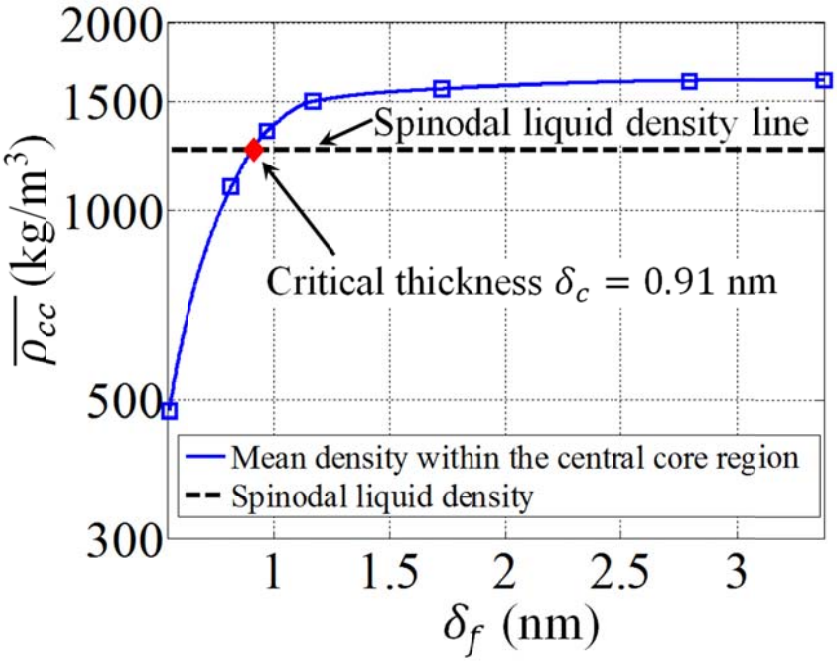

Figure 4.4 Variations of $\overline{\rho_{cc}}$ with δ_f for argon at $T_r = 0.6$

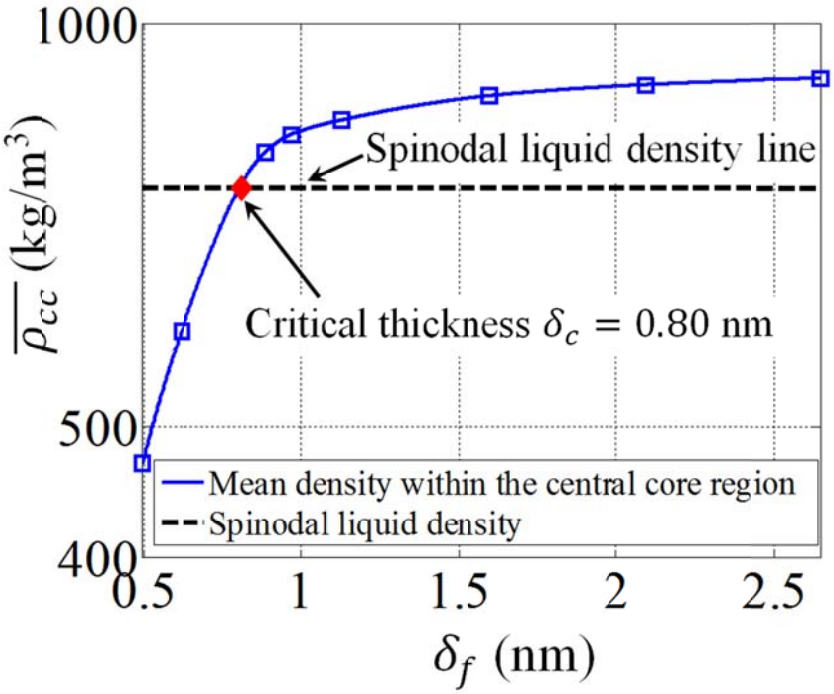

Figure 4.5 Variations of $\overline{\rho_{cc}}$ with δ_f for pure water at $T_r = 0.6$

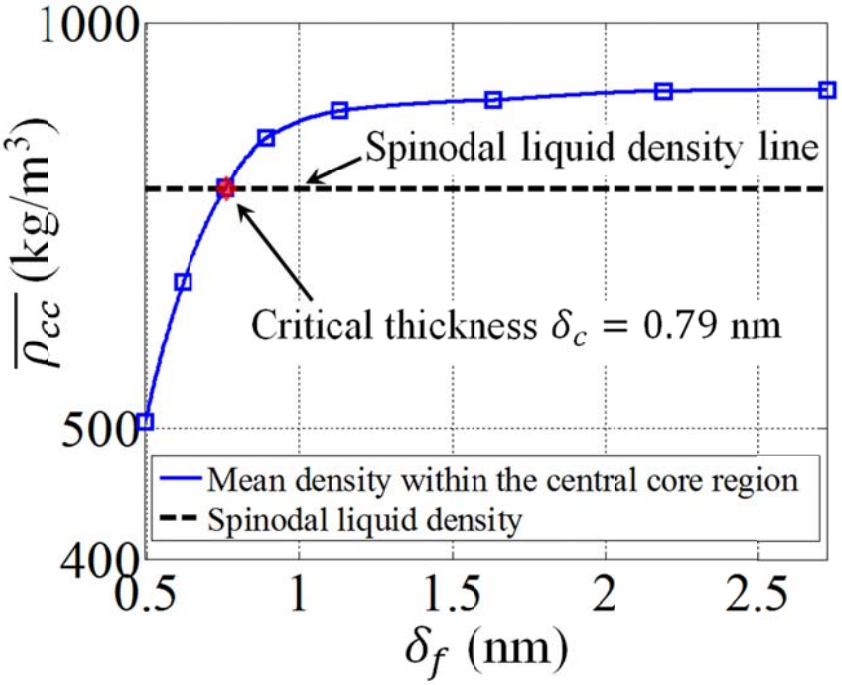

Figure 4.6 Variations of $\overline{\rho_{cc}}$ with δ_f for 0.38 M NaCl aqueous solution at $T_r = 0.6$

As we can observe from the above three plots (Figure 4.4 to 4.6), the mean density within the central core region $\overline{\rho_{cc}}$ decreases with the decrease of film thickness δ_f, and eventually reaches to a level below the spinodal liquid density $\rho_{spinodal,l}$ for all three systems of argon, pure water, and NaCl aqueous solution. Based on thermodynamic intrinsic stability criteria, we know that mean density values between spinodal liquid and spinodal vapor densities are not expected to exist in real systems because the fluid would lack intrinsic stability for such conditions. Therefore, we expect that the liquid film is ruptured if the mean density within the central core region $\overline{\rho_{cc}}$ is less than the spinodal liquid density $\rho_{spinodal,l}$, indicating the initially central liquid region lacks intrinsic stability. The critical thickness δ_c is defined as the value of δ_f corresponding to this density condition:

$$\overline{\rho_{cc}}|_{\delta_f=\delta_c} = \rho_{spinodal,l} \tag{4.3}$$

The cross points of $\overline{\rho_{cc}}$ curve-fitting lines and spinodal liquid density lines showing in Figure 4.4, 4.5 and 4.6 indicate that at reduced temperature of $T_r = 0.6$, $\delta_c = 0.91$ nm for argon liquid film, $\delta_c = 0.80$ nm for pure water liquid film and $\delta_c = 0.79$ nm for 0.38 M NaCl aqueous solutions respectively.

As mentioned in the introduction chapter, an important advantage of MD simulation method is that it can provide direct insight into the behavior of molecules or ions and their interactions. The stability analysis described above is verified by examining snapshots of the molecular behavior in MD simulations. The following Figures from 4.7 to 4.9 show two MD snapshots for systems of argon, pure water and 0.38 M NaCl aqueous solutions respectively, in which one of the snapshots corresponds to $\overline{\rho_{cc}} < \rho_{spinodal,l}$, and the other corresponds to $\overline{\rho_{cc}} > \rho_{spinodal,l}$.

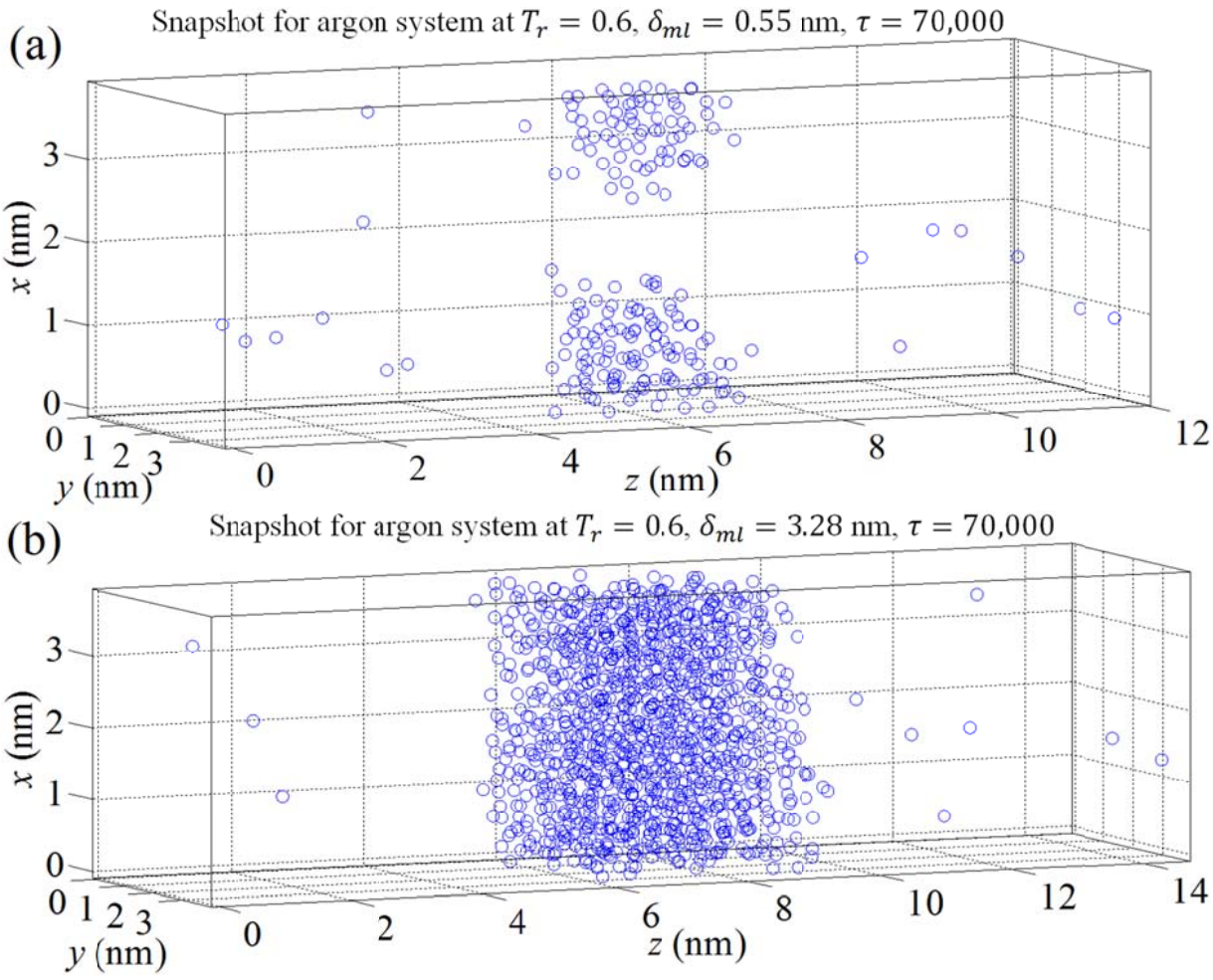

Figure 4.7 Snapshots of molecules in MD simulations of argon: (a) $\overline{\rho_{cc}} < \rho_{spinodal,l}$ (b) $\overline{\rho_{cc}} > \rho_{spinodal,l}$

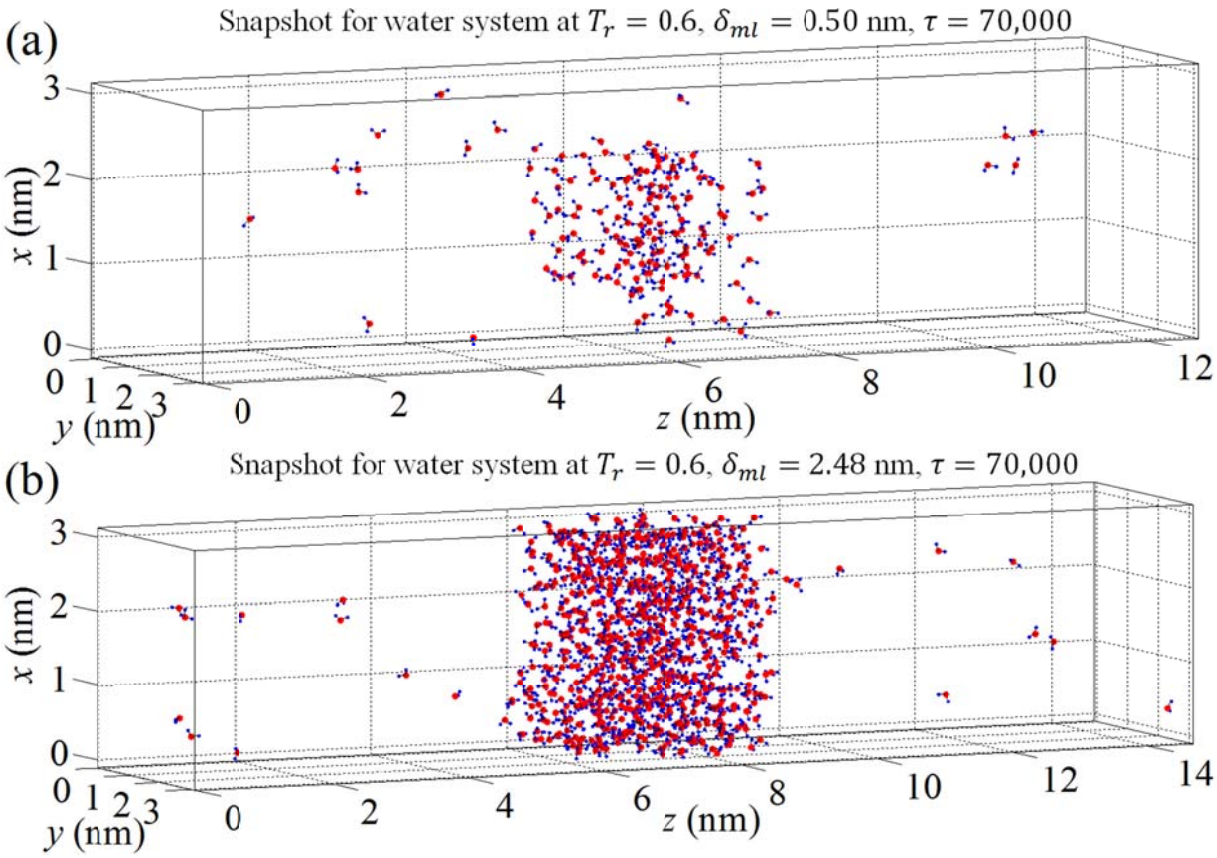

Figure 4.8 Snapshots of molecules in MD simulations of water: (a) $\overline{\rho_{cc}} < \rho_{spinodal,l}$ (b) $\overline{\rho_{cc}} > \rho_{spinodal,l}$

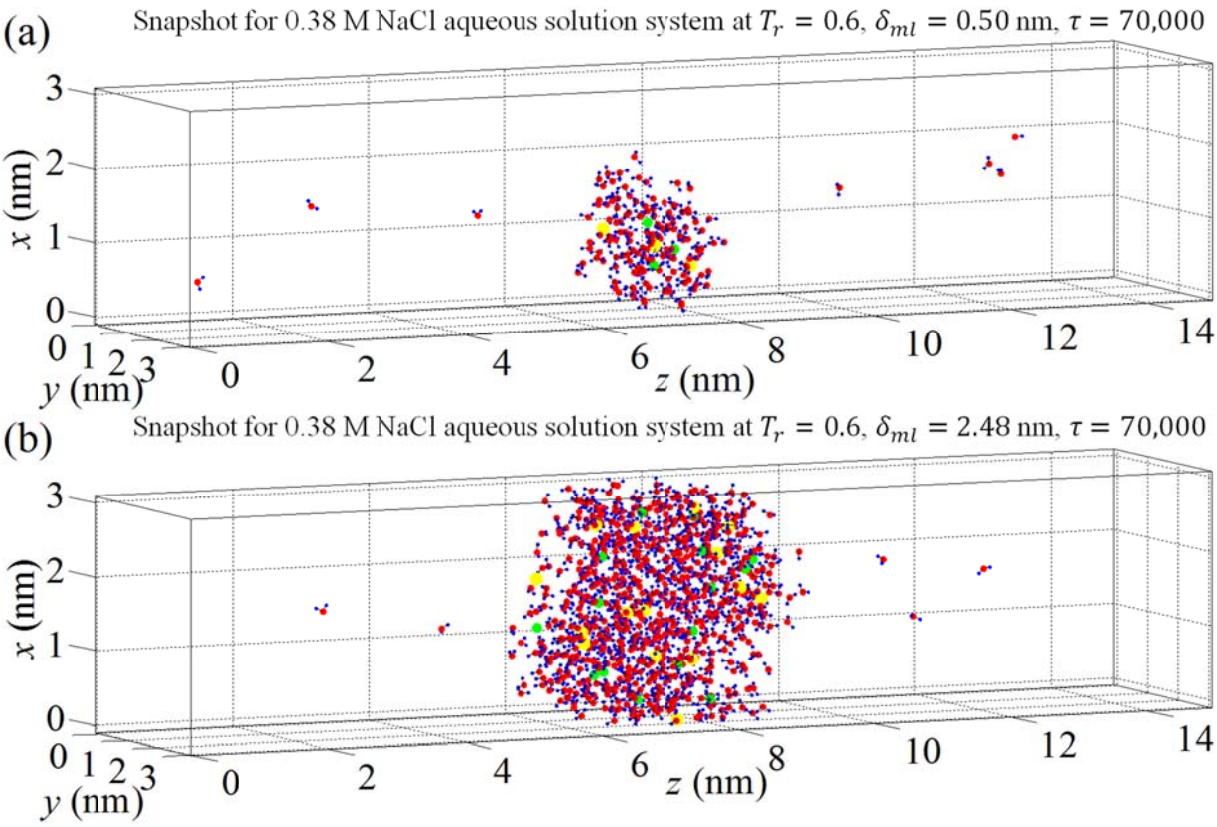

Figure 4.9 Snapshots of molecules and ions in MD simulations of 0.38 M NaCl aqueous solutions: (a) $\overline{\rho_{cc}} < \rho_{spinodal,l}$ (b) $\overline{\rho_{cc}} > \rho_{spinodal,l}$

As suggested by these snapshots, for simulations with $\overline{\rho_{cc}} > \rho_{spinodal,l}$ (Figure 4.7b, 4.8b, 4.9b), films of molecules (including ions for NaCl aqueous solutions) consistently span the lateral extent of the simulation domain, indicating the formation of stable films. For simulations with $\overline{\rho_{cc}} < \rho_{spinodal,l}$ (Figure 4.7a, 4.8a, 4.9a), systems fail to form steady films spanning the lateral dimensions, indicating film ruptures. The behavior of molecules and ions is in agreement with our stability analysis prediction that the film is unstable when the mean density within the central core region is below the liquid spinodal density.

§ 4.2 CRITICAL THICKNESS VARIATION

In previous section, we discussed the effects of the film molar loading thickness δ_{ml} on film stability. The critical thickness δ_c is determined by series of MD simulations at fixed system temperature, specified system composition (i.e. the solute concentrations for electrolyte aqueous solutions), with various values of δ_{ml}. Using the same method, we can obtain the values of

critical thickness for different system temperatures or electrolyte solute concentrations. Since a larger value of critical thickness δ_c indicates that the system is less stable and the film ruptures more easily, we can investigate the effects of temperature and solute concentration on film stability by examining the variations of δ_c with these parameters.

Variations of critical thickness δ_c with system temperature

For systems of argon and pure water, MD simulation are carried out at seven reduced temperatures from 0.6 to 0.9, and for system of 0.38 M NaCl aqueous solution, five reduced temperatures from 0.6 to 0.8 are studied. Shown in Figure 4.10, 4.11 and 4.12 are the variations of δ_c with reduced system temperatures, in which Figure 4.10 and 4.11 are for argon and pure water respectively, and Figure 4.12 is for 0.38 M NaCl aqueous solutions.

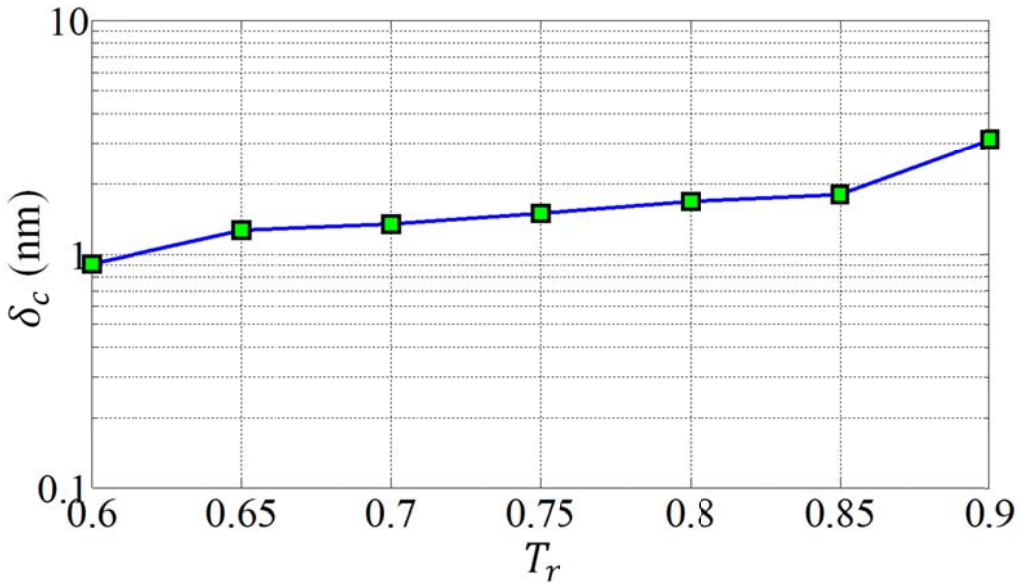

Figure 4.10 Critical thickness variations with reduced system temperature predicted by MD simulations for argon

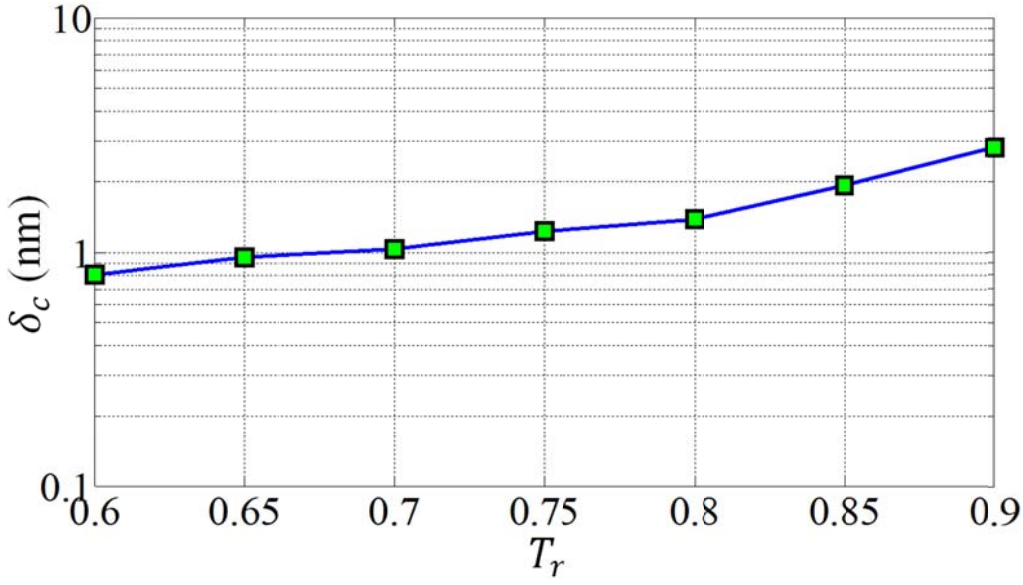

Figure 4.11 Critical thickness variations with reduced system temperature predicted by MD simulations for pure water

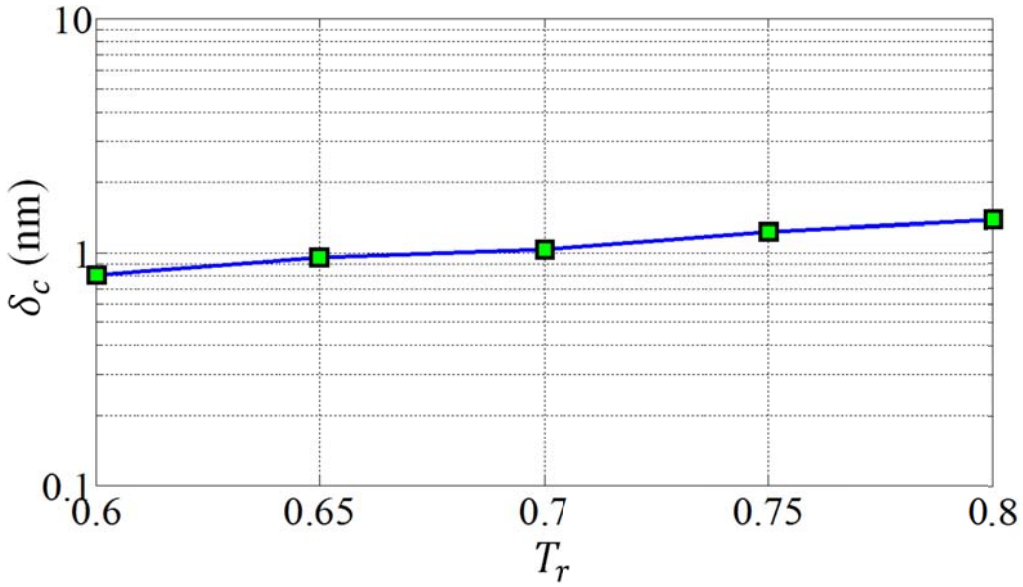

Figure 4.12 Critical thickness variations with reduced system temperature predicted by MD simulations for 0.38 M NaCl aqueous solution

As suggested in these three plots, for systems of argon, water and NaCl aqueous solution, the critical thickness increases with the increase of system temperature, indicating that films are less stable under higher temperatures. This observation is consistent with our expectation and the

results from our film capillarity model. Based on the kinetic theory, at a higher temperature, molecules or ions move more vigorously, which may expand the thickness of liquid-vapor interfacial regions and intensify the interactions between interfacial regions on two sides of the film, resulting in a less stable film.

Variations of critical thickness δ_c with electrolyte concentration

To investigate the effect of electrolyte solute concentration on film stability, 5×5 MD simulations are carried out for NaCl aqueous solutions, in which five NaCl concentrations from 0.38 M to 1.88M and five reduced temperatures from 0.6 to 0.8 are studied. Variations of critical thickness δ_c with NaCl concentrations C_{NaCl} are plotted in Figure 4.13. Each line in this plot represents a specified reduced temperature.

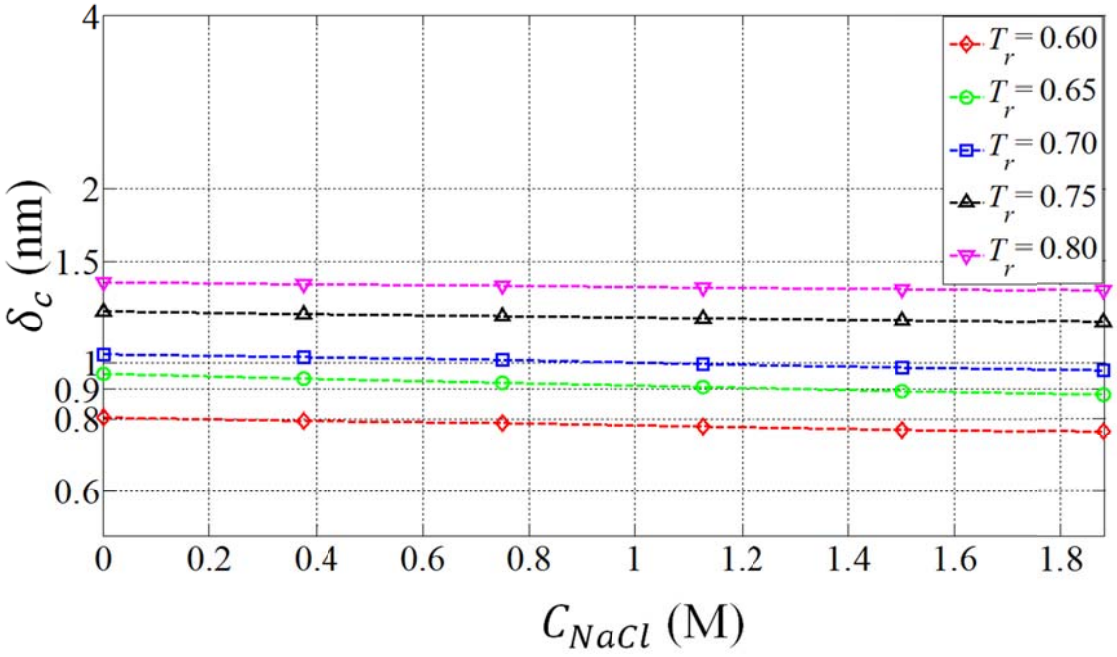

Figure 4.13 Critical thickness variations with electrolyte solute concentration predicted by MD simulations for NaCl aqueous solution at five reduced temperatures

As shown in Figure 4.13, MD simulation results indicate that the increasing NaCl concentration decreases the critical film thickness at fixed temperatures, which in turn suggest that the presence of the Na^+ and Cl^- ions tends to stabilize the liquid film. For bubbles in liquid, this suggests that the presence of dissolved NaCl makes it less likely that adjacent bubbles will merge in two-phase flow or during a boiling process.

From the point of view of the wave instability model [4], the presence of the Na^+ and Cl^- ions tends to enhance the increase of free energy due to the increase of surface area in a perturbing wave and increase the interfacial tension of the solution. Thus, in turn, has the effect of enhancing the stability of the film by reducing the critical film thickness as shown in Equation 1.3 and Equation 2.74. This is also consistent with the conclusions reached by our MD simulation results regarding the impact of dissolved ionic solids on film stability.

Although no theoretical model or explicit experimental data about the critical thickness of NaCl aqueous solution film can be found in literatures, many previous studies showed consistent conclusions that NaCl enhances bubble stability. The observations of Huang and Carey [72], regarding the effect of dissolved salt on the Leidenfrost temperature for water spheroids deposited on a hot aluminum surface, found that addition of dissolved NaCl significantly raised the Leidenfrost temperature, the minimum surface temperature required to sustain film boiling. Theories of the Leidenfrost transition proposed by Bernardin and Mudawar [73,74]) and others are based on the premise that bubble merging under liquid droplet or spheroid masses in contact with a hot surface is the mechanism that dictates the transition from transition boiling to film boiling on the side of the droplet facing the surface. If this theory of the mechanisms is correct, any alteration of the process that tends to suppress bubble merging will push the surface temperature for the onset of film boiling to a higher level. The data obtained by Huang and Carey [72] indicate that the Liedenfrost temperature that defines this transition is increased substantially by the addition of a small amount of dissolved NaCl. Our MD simulation results described here imply that increasing NaCl concentration enhances the stability of the thin liquid film between adjacent bubbles, which makes it more difficult for the bubbles to merge and makes it more difficult to establish a stable vapor film between a liquid spheroid an a heated surface. Therefore the surface temperature must be pushed to a higher level to create circumstance that produced more rapidly growing bubbles to overcome the added resistance of bubble merging by adding NaCl to the water. As shown in Figure 4.13 the critical thickness changes slowly with increasing NaCl concentration. In aqueous solutions with dilute salt concentrations, the effect of dissolved ion on film stability may therefore be low. However, for films between bubbles growing through vaporization, the salt concentration may be locally enhanced, resulting in a stronger stabilizing effect.

§ 4.3 SURFACE TENSION

Surface tension derived from MD simulations is of great importance in our study. The abundant experimental measurement data in literatures make the surface tension an ideal indicator to validate our MD simulation model. Since most of the surface tension data found in literatures were measured for its bulk value at the interface between semi-infinite bulk liquid and semi-infinite bulk vapor phases, values of surface tension from MD simulations to make the comparison are taken from thick film cases, which contain both stable vapor and liquid phases. For examples, at $T_r = 0.6$, $\delta_{ml} = 3.28$ nm case for argon, or $\delta_{ml} = 2.48$ nm case for pure water and NaCl aqueous solution contain both stable vapor and liquid phases as indicated by both the

mean local density profiles (as shown in Figure 4.1 to 4.3) and observations of molecular distributions during the simulations (as shown in Figure 4.7 to 4.9).

Surface tension variations with temperatures

Shown in Figure 4.14 and 4.15 are the surface tension variation with temperature for argon and pure water respectively. In these two figures, the NIST recommend values of surface tension [41] at various system temperatures are also plotted for comparison.

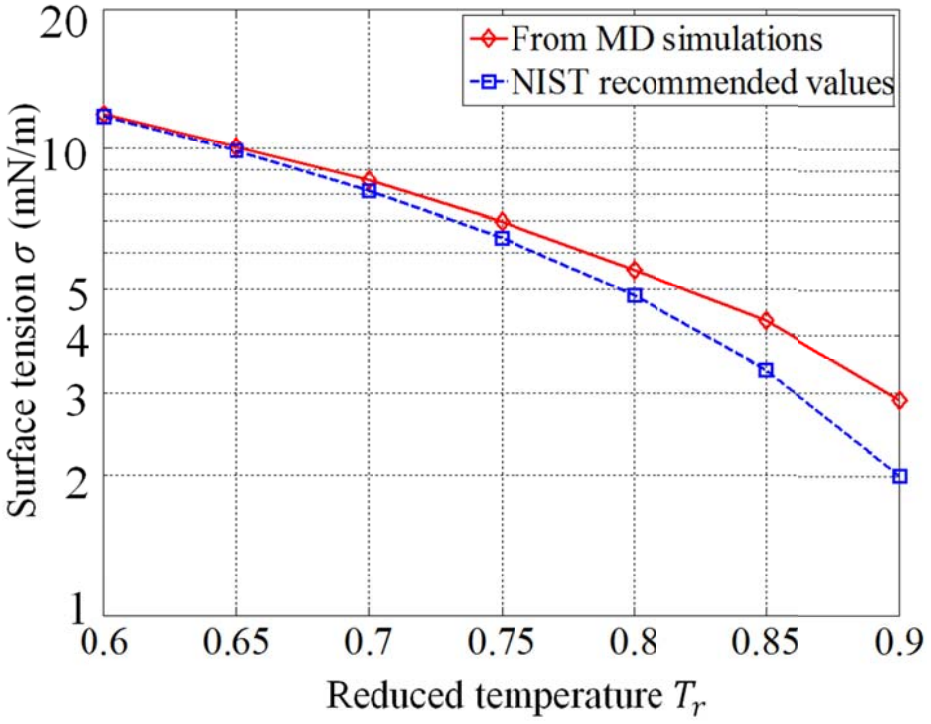

Figure 4.14 Variations of surface tension with reduce temperatures for system of argon

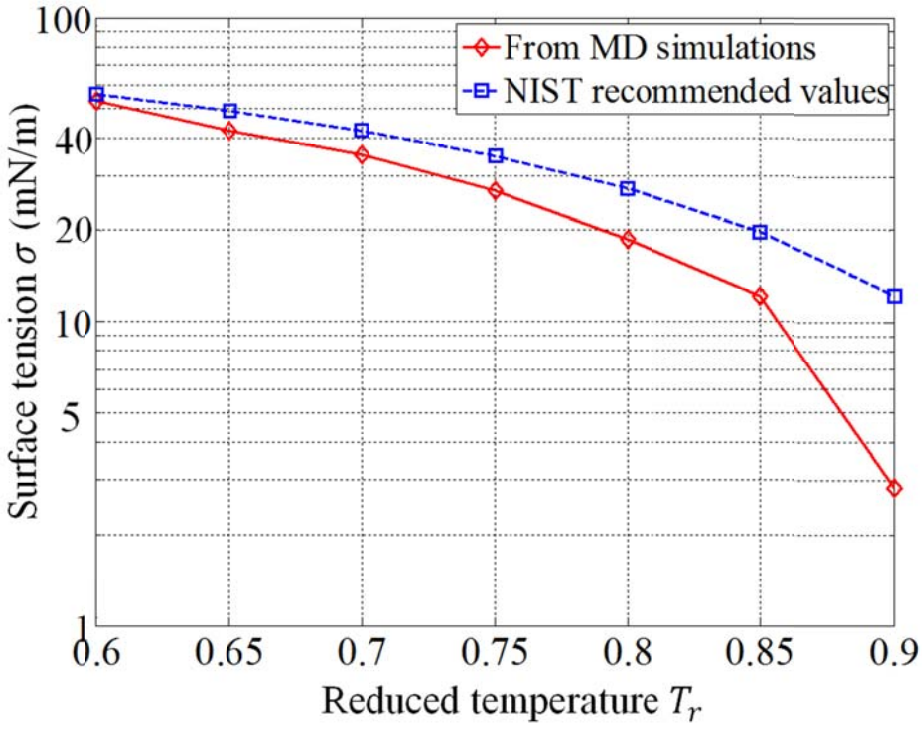

Figure 4.15 Variations of surface tension with reduce temperatures for system of water

Despite of the embedded idealization of potential functions and the inherent error of computing algorithms used in MD simulations, values of surface tension predicted by MD simulations and recommended by NIST [41] are in fair agreement. The numerical differences are generally greater for water than that for argon at the same temperature due to the fact that the SPC/E potential function of water is more complex and computing intensive than the Lennard-Jones potential function used for argon. For both argon and water, surface tension decreases with the increase of system temperature, as we expected.

Surface tension variations with electrolyte solute concentration

Plenty of experimental measurement data are available in literatures to study the effects of dissolved ionic solute on surface tension, including various electrolyte species at different concentrations. Comparisons between the experiment data and the surface tension predicted by MD simulations are shown in Figure 4.16, in which we plot the variation of surface tension with solute concentrations for NaCl, NaI, $NaClO_4$ and $CaCl_2$ aqueous solutions. Since most of the experiments are done under room temperatures of 25 °C, the MD simulations for NaCl, NaI, $NaClO_4$ and $CaCl_2$ aqueous solutions are carried out at reduced temperature of $T_r = 0.46$. The parameters of potential functions of NaI, $NaClO_4$ and $CaCl_2$ are given in Table 3.1. As discussed in the beginning of this section, values of surface tension from MD simulations are taken from

thick film cases ($n_{z,l} = 5$ and $\delta_{ml} = 2.47$ nm), which contain both stable vapor and liquid phases.

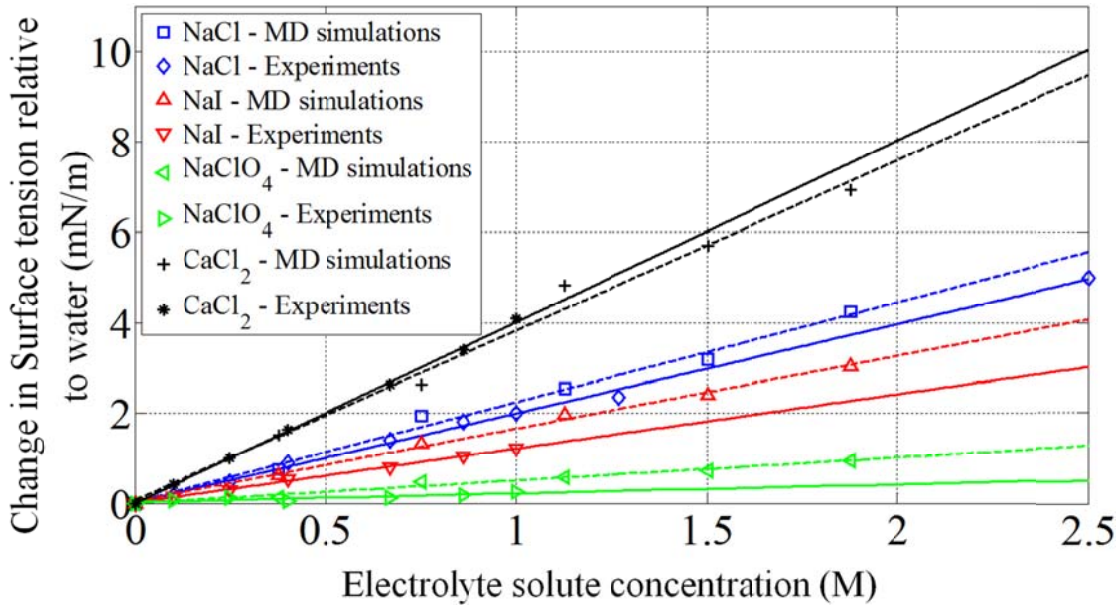

Figure 4.16 Effect of ionic solute concentration on the change in surface tension relative to water (experimental data are from Weissenborn and Pugh [30], Abramzon and Gaukhberg [31], and Svenningsson, *et al.* [32]).

The solid lines and broken lines in Figure 4.16 are the first order polynomial fitting lines for experiment measurement results and MD simulation results respectively. MD simulations accurately predict the increase of surface tension with the increase of electrolyte solute concentration for NaCl, NaI, $NaClO_4$ and $CaCl_2$, as indicated in Figure 4.16. The rates of surface tension increase with the concentration, $\partial\sigma/\partial C$, for these four species of electrolyte solutes predicted by MD simulations are seen to be in good agreement with the experimental data.

The increase of surface tension with the increase of electrolyte solute concentration indicated in Figure 4.16 is consistent with the well-known Gibbs adsorption equation (Carey [15], Miller [7]), and the distributions of ions within the interfacial regions and the center core regions. As an example, Figure 4.17 shows the ion distribution profile for a 1.88M NaCl aqueous solution film with $\delta_{ml} = 2.47$ nm at $T_r = 0.46$, together with its time-averaged local density profile predicted by MD simulation.

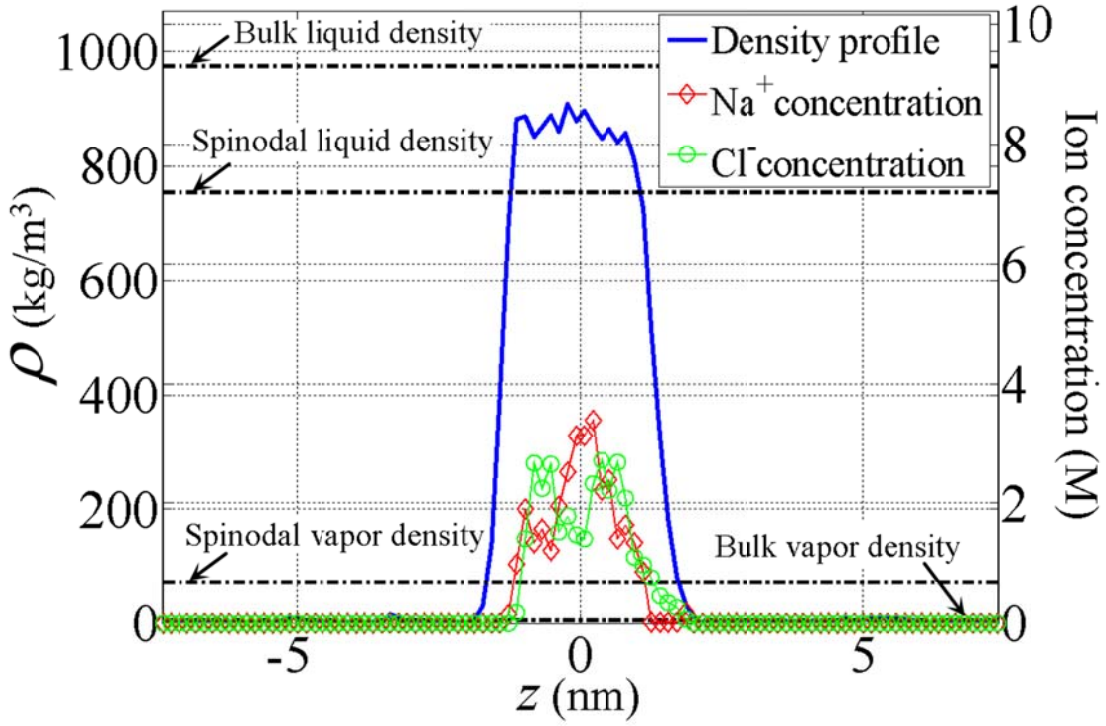

Figure 4.17 Ion concentration profile and density profile for the 1.88M NaCl aqueous solution simulation with film with $\delta_{ml} = 2.47$ nm at $T_r = 0.46$.

The Gibbs adsorption equation [35] is:

$$\Gamma_{NaCl} = -\left(\frac{C_{NaCl}}{RT}\right)\left(\frac{\partial \sigma}{\partial C_{NaCl}}\right)_T \tag{4.4}$$

in which, Γ_{NaCl} is the surface excess mass of NaCl, the excess of NaCl per unit area of the liquid-vapor interfacial region over what would be present if the concentration in the center core liquid region prevails all the way through the interfacial region. It is clearly indicated in Figure 4.17 that $\Gamma_{NaCl}$is a negative quantity, i.e. ions are more concentrated in the center core region than in the vapor-liquid interfacial regions, resulting a positive value of $(\partial\sigma/\partial C_{NaCl})_T$.

§ 4.4 SURFACE TENSION DEVIATION FOR THINNING FILMS

In the film capillarity theory analysis discussed previously, a noteworthy observation is the significant deviation of the surface tension value from its bulk value as the film becomes thinner. A characteristic threshold thickness δ_{th} is defined. When the film thickness δ_f drops below this threshold thickness, the surface tension values for thinning films decrease abruptly from its bulk value for a thick film containing both stable vapor and liquid phases. This surface tension deviation predicted by the film capillarity model is curve-fitted and described by Equation 2.73.

Values of surface tension predicted by a sequence of MD simulations with decreasing film thickness indicate the same type of surface tension deviation, as shown in Figure 4.18 for pure water at $T_r = 0.6$.

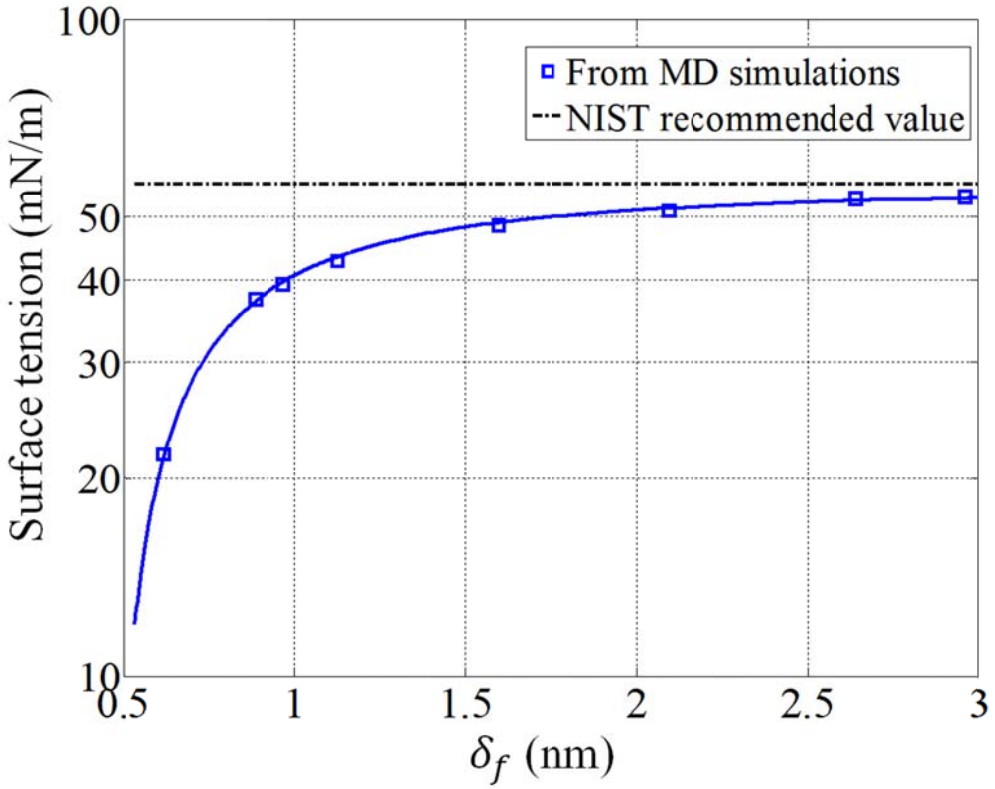

Figure 4.18 Surface tension variations with film thickness δ_f for pure water predicted by MD simulations at $T_r = 0.6$.

As proposed by Equation 2.74 in the film capillarity theory analysis, the surface tension deviation may have noteworthy impact on the determination of the critical thickness. Therefore,

we use the same definition of the characteristic threshold thickness δ_{th} and use the same function form of Equation 2.73 as those used in the film capillarity model to describe the surface tension deviation predicted by MD simulations. As a comparison, at reduced temperature $T_r = 0.6$, the film molecular capillarity model predicts $\delta_{th} = 1.53$ nm for pure water and the value of δ_{th} predicted by MD simulations for pure water at the same temperature is 1.62 nm. Determination of δ_{th} from MD simulation data requires curve-fitting of the variation of σ with δ_f, which has inherent uncertainties. It can be seen, however, that the order of magnitude of δ_{th} predicted by MD simulations is consistent with our film molecular capillarity theory results.

For pure water at room temperature of $T_r = 0.46$, the correlation-constants of Equation 2.73 are: $\sigma_\infty = 69.22$ mN/m, $\delta_{th} = 1.498$ nm and $m = 2.906$. Given in Table 4.1 are the correlation-constants of Equation 2.73 for NaCl, NaI, $NaClO_4$ and $CaCl_2$ aqueous solutions with various solute concentrations at $T_r = 0.46$, which are going to be used in the following chapter to compare the modified wave instability model (Equation 2.74) with the bubble merging experiments at room temperature of 25 °C.

Table 4.1
Surface tension deviation correlation constants for NaCl, NaI, $NaClO_4$ and $CaCl_2$ aqueous solutions at room temperature of 25°C.

Concentration (M)	0.375	0.751	1.127	1.502	1.878
$\sigma_{\infty,NaCl}$ (mN/m)	69.97	71.16	71.76	72.41	73.46
$\delta_{th,NaCl}$ (nm)	0.685	0.633	0.622	0.619	0.615
m_{NaCl}	2.127	2.913	2.632	2.098	2.279
$\sigma_{\infty,NaI}$ (mN/m)	69.84	70.54	71.20	71.61	72.27
$\delta_{th,NaI}$ (nm)	0.921	0.809	0.752	0.729	0.706
m_{NaI}	2.217	2.463	2.149	2.154	2.506
$\sigma_{\infty,NaClO_4}$ (mN/m)	69.35	69.70	69.81	69.95	70.17
$\delta_{th,NaClO_4}$ (nm)	1.453	1.415	1.381	1.355	1.341
m_{NaClO_4}	2.964	2.669	2.946	2.701	2.561
$\sigma_{\infty,CaCl_2}$ (mN/m)	70.73	71.86	74.05	74.94	76.15
$\delta_{th,CaCl_2}$ (nm)	0.627	0.603	0.596	0.591	0.590
m_{CaCl_2}	2.215	2.359	2.952	2.300	2.540

§ 4.5 SUMMARY

By using the method described in the previous chapter, MD simulations are carried out in this chapter for various fluid systems, film thickness, system temperatures and solute concentrations. Simulation results of density distribution profiles, ion distribution profiles and surface tension values are examined and analyzed in detail.

First, the stability of thin liquid films is studied and the critical thickness is defined, using the thermodynamic intrinsic stability criteria and density profiles derived from MD simulations. Based on the critical thickness variations with respect to system temperature and the electrolyte solute concentration, the effects of these two parameters on film stability are investigated.

Values of surface tension from MD simulations for various temperatures and system compositions are compared with the experimental data in literatures. Fairly good consistencies showed in the comparisons indicate that MD simulation is an acceptable method for our research purpose. In addition, the surface tension deviation for thinning films is also observed in our MD simulation results. We are able to characterize and describe this surface tension deviation using the definition of threshold thickness and the correlation proposed in the film capillarity model. For electrolyte aqueous solutions, constants of the surface tension deviation correlation derived from MD simulations supplement the results we derived for argon and pure water from the film capillarity theoretical analysis.

CHAPTER 5 – EXPERIMENT AND COMPARISON

In previous chapters, film stability is investigated by the wave instability models, the film capillarity intrinsic stability model and MD simulations. Critical thickness, corresponding to the thinnest stable film before the first occurrence of film rupture, is generally reported on the order of nanometers. Direct experimental measurements for films with thickness in the nanometer length scale are commonly difficult and involve complex optical systems. Therefore, although indirect, the bubble merging experiment method is adopted in our study. Since the bubble merging probability is tightly related with the critical thickness of separating liquid films between pairs of bubbles, by examining the variation of bubble merging probabilities with electrolyte species and concentrations, the effect of dissolved electrolyte ions on film stability is studied and compared with our predictions from the wave instability model, the film capillarity intrinsic stability model and MD simulations.

The apparatus and procedure of the bubble merging experiment are first described. Experiment results for various system compositions and concentrations are presented with the discussion of the relationship between the bubble merging probability and film stability in order to interpret the experiment results. Finally, conclusions of film stability analysis reached by the wave instability models, the film capillarity intrinsic stability model, MD simulations and bubble merging experiments are compared.

§ 5.1 EXPERIMENT APPARATUS AND PROCEDURE

In the experiments, pairs of contacted air bubbles are generated by two brass injection tubes with diameter 4.76mm aligned vertically in a transparent Plexiglas cylindrical chamber as shown in Figures 5.1. The cylindrical chamber is filled by pure water or electrolyte aqueous solutions at desired concentrations. The schematic diagram of the apparatus used is shown in Figures 5.1. The two injection tubes are connected to two 20 ml gas-tight syringes by polyvinyl tubes respectively. The pistons of the syringes are fixed on a rigid platform, which can be raised and lowered mechanically along a threaded bolt. Raising the platform at a constant speed pushes the pistons of two syringes simultaneously. Pairs of bubbles are generated on the tips of injection tubes in the solution. Buoyancy acts to push the bubble ejected from the lower tube upward against the bubble ejected downward form the upper tube. Because the vertical buoyant force acting on a bubble is dominant, placing the injection tubes vertically in the solution reduces the disturbance introduced by external vibrations or other sources. The separation between the tips of

injection tubes is adjusted to 10 mm in order to ensure that the ejected bubbles are pressed into close proximity before departure from the tips of injection tubes.

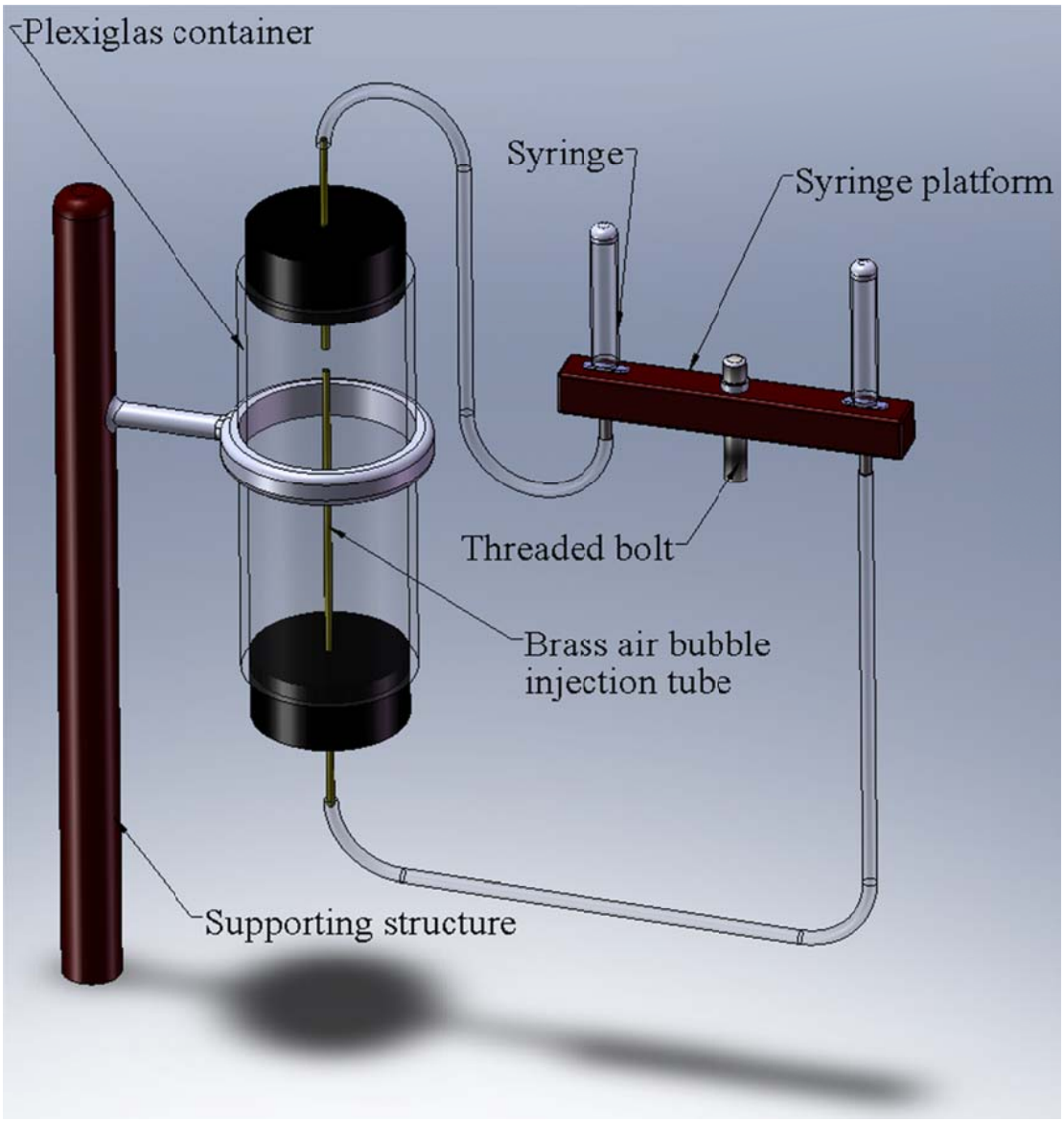

Figure 5.1 The schematic diagram of the experimental apparatus.

Seven concentrations ranging from 0 M (pure water) to a 1.88 M solutions of NaCl, NaI, $NaClO_4$ and $CaCl_2$ were tested at room temperature of 25°C respectively. The solutions were made by dissolving ACS reagent grade electrolytes with minimum purities of 99% into distilled water. At each concentration, 100 pairs of bubbles are generated. The degree of bubble merging is

determined by counting on the number of coalescing pairs and determining the fraction that coalesced, which is reported as the probability of merging.

§ 5.2 EXPERIMENT RESULTS AND INTERPRETATION

As shown in Figure 5.2a, pairs of air bubbles formed simultaneously at the top and bottom injection tubes are slightly pressed together before releasing. Measuring from still images of contacted bubbles give the lateral size $L_{lateral}$ of the separating film on the order of 3.5 mm. Figure 5.2b and 5.2c represent the typical behavior of bubbles in pure water or $NaClO_4$ solutions and in other electrolyte aqueous solutions respectively. Bubbles most often coalesced spontaneously on contact in pure water or $NaClO_4$ solutions, but were more likely to remain separate in other electrolyte aqueous solutions..

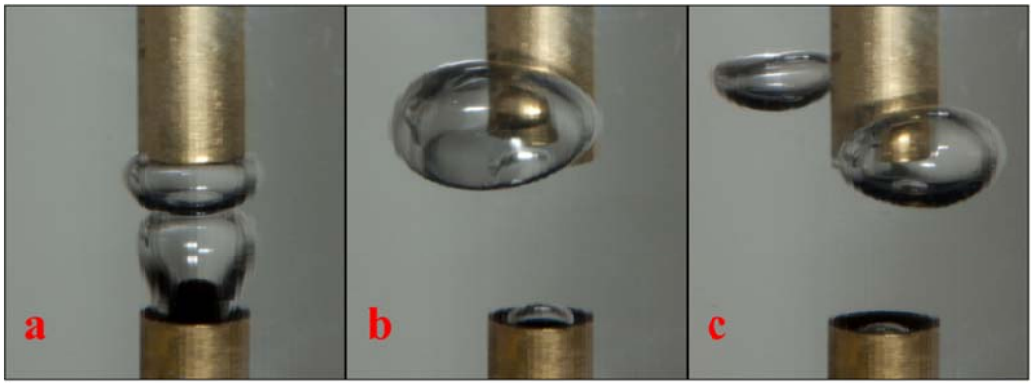

Figure 5.2 Typical behaviors of bubbles in experiments: (a) formation of pairs of bubbles, (b) merged bubble in pure water or $NaClO_4$ solutions, (b) separate bubbles in other electrolyte aqueous solution.

The probabilities of bubble merging P_m for NaCl, NaI, $NaClO_4$ and $CaCl_2$ aqueous solutions with seven different concentrations at room temperature of 25 °C are given in Table 5.1. In Figure 5.3 and 5.4, our experiment results for NaCl and $CaCl_2$ aqueous solutions are compared with previous reported results by Lessard and Zieminski [36], Aguilera *et al* [37] and Craig *et al* [75].

Table 5.1
The bubble merging probability P_m for NaCl, NaI, NaClO4 and CaCl2 aqueous solutions with various concentrations at room temperature of 25 °C.

Concentration (M)	$P_{m,NaCl}$	$P_{m,NaI}$	$P_{m,NaClO_4}$	$P_{m,CaCl_2}$
0	0.99	0.99	0.99	0.99
0.09	0.86	0.91	0.96	0.57
0.19	0.37	0.77	0.97	0.06
0.28	0.12	0.34	0.95	0.02
0.75	0.02	0.13	0.93	0.02
1.50	0.01	0.02	0.94	0.01
3.76	0.00	0.00	0.91	0.00

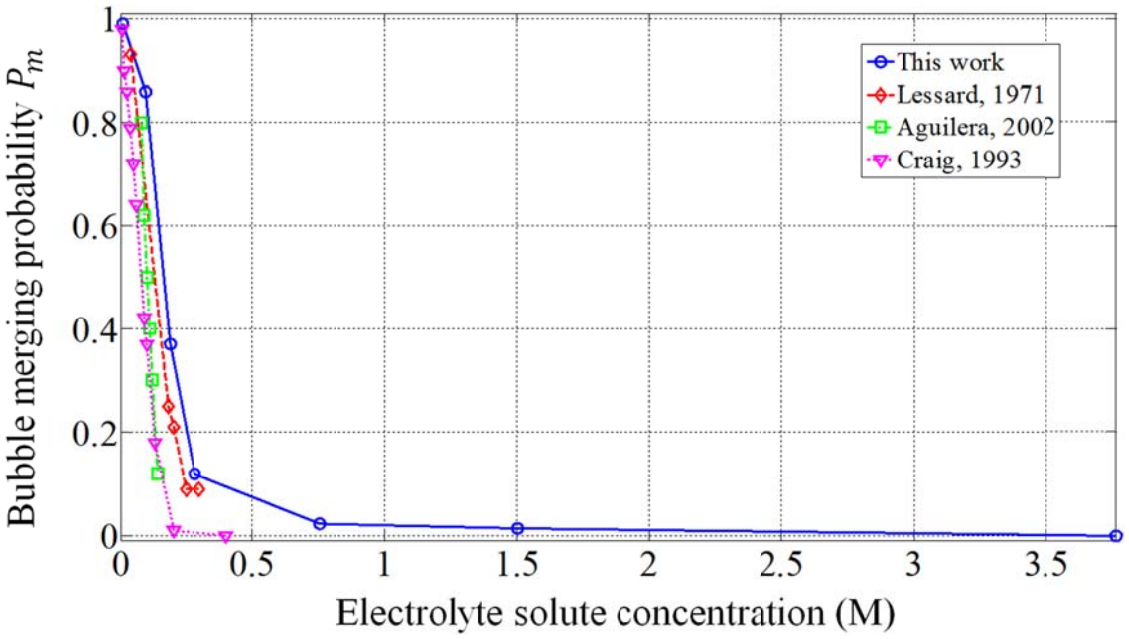

Figure 5.3 Comparison of bubble merging experiment results for NaCl aqueous solutions. Experiment results reported by other researchers include: Lessard [36], Aguilera [37] and Craig [75].

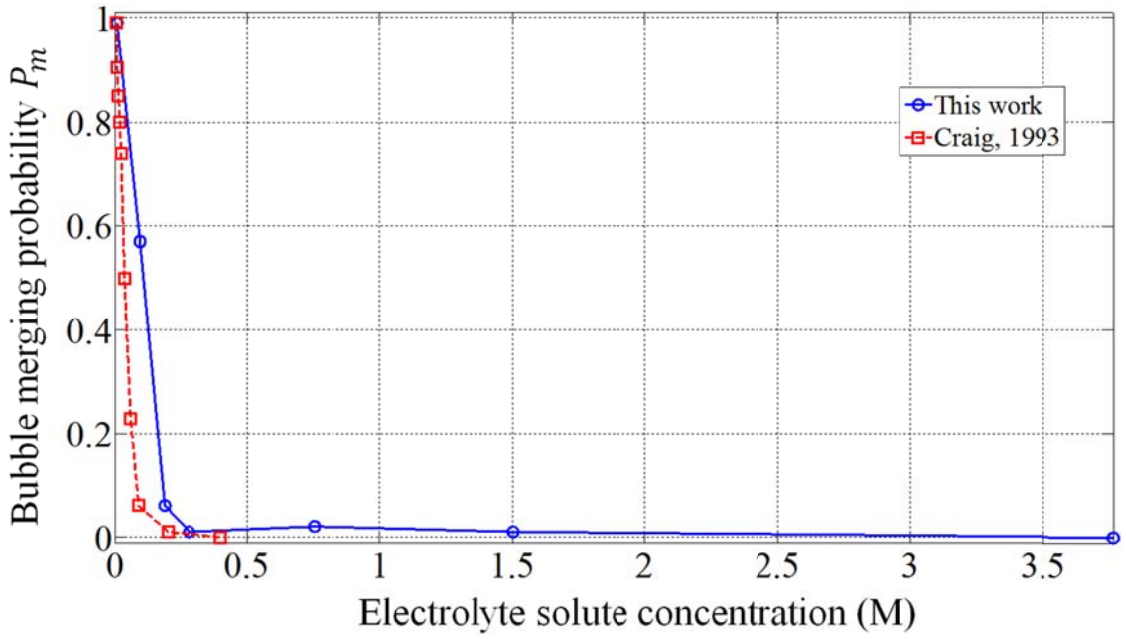

Figure 5.4 Comparison of bubble merging experiment results for $CaCl_2$ aqueous solutions. Experiment results reported by the other researcher are from Craig [75].

Although the numerical values of merging probability reported by different researchers are slightly different due to different experimental setup, the overall trend of electrolyte effect on bubble merging is consistent among the results, as shown in the above two plots.

From the perspective of the liquid film between contacted bubbles, whether bubbles merge or not is determined by the film thickness as well as the critical thickness under the experiment condition. As illustrated in Figure 5.5, if the thickness of the separating film δ_{sep} is greater than the critical thickness δ_c corresponding to the specified temperature and electrolyte solute concentration, film should remain stable and the pair of bubbles should remain separate after contact, whereas if film thin to less than the critical thickness, the resulting rupture of the film would lead to the merging of bubbles in the experiment. It is reasonable to assume that the thicknesses of the separating film for each pair distribute randomly within a fixed range. It follows that the experimentally determined trends of decreasing bubble merging probability with the increase of electrolyte solute concentrations shown in Figure 5.3 and 5.4 indicate the decrease of critical thickness, which is consistent with the trends predicted by MD simulations and wave instability models, as shown in the subsequent section.

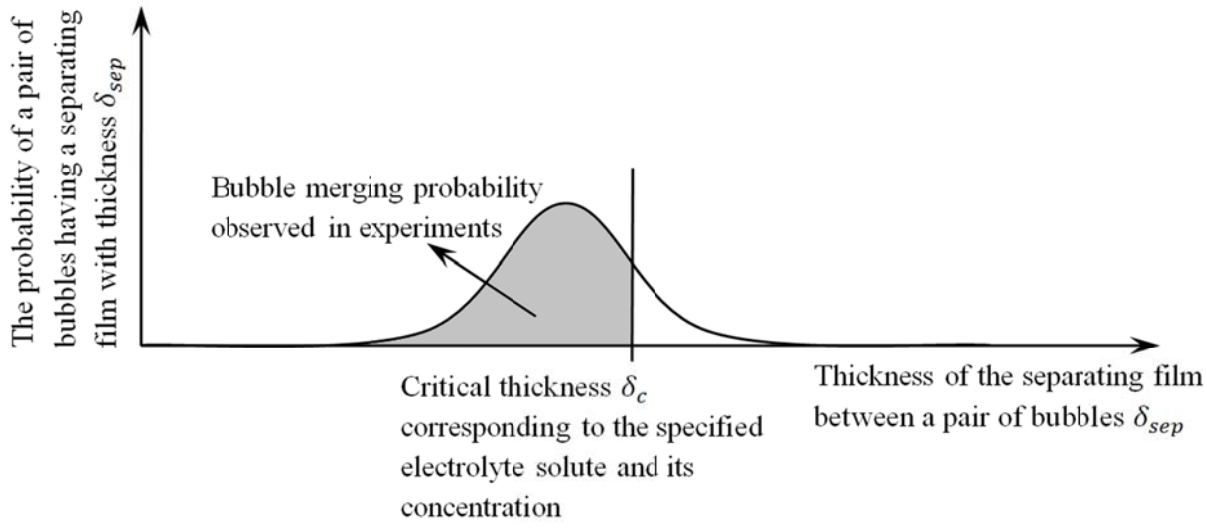

Figure 5.5 Illustration of the relationship between the bubble merging probability and critical thickness

§ 5.3 COMPARISONS AMONG THEORETICAL MODEL ANALYSIS, MD SIMULATIONS AND EXPERIMENTS

The research described in this report has studied the free liquid film stability and the effects of system variables on stability, such as film thickness, film lateral size, system temperature and the addition of electrolytes. The original wave instability model, the modified wave instability model with surface tension correction, the film capillarity intrinsic stability model, the MD simulation method and experimental method are examined in details in this study. As a key outcome, the critical thickness δ_c quantitatively characterizes the stability of a system, and its variations with other variables describe their effects on the film stability. In the theoretical model analysis and the MD simulation method, numerical values of δ_c are derived explicitly. Although the critical thickness δ_c is not measured directly in the experiments, the bubble merging probability reported in the experiments is interpreted to be tightly related with the critical thickness of separating liquid films. Therefore, comparisons across theoretical model analysis, MD simulations and experiments are based on the critical thickness δ_c and its variations. The first comparison uses argon and pure water as examples. Numerical values of δ_c and variations of δ_c with temperatures predicted by theoretical model analysis and MD simulations are compared, showing the effect of system temperature on film stability. The second comparison uses the electrolyte aqueous solutions as examples. Variations of δ_c with electrolyte concentration predicted by theoretical model analysis, MD simulations and experiments are compared, showing the effect of the addition of electrolytes on film stability.

Comparing the effect of system temperature on film stability

Figure 5.6 and Figure 5.7 show the variations of critical film thickness δ_c with reduced system temperatures indicated by the original wave instability model, the modified wave instability model with surface tension correction, the film capillarity intrinsic stability model and MD simulations for argon and water respectively. In the original wave instability model, the critical thickness δ_c is calculated by Equation 1.4, in which the Hamaker constant A_H is calculated by Equation 2.75, and the lateral film dimension is set as $L = 3.83$ nm for argon and $L = 2.48$ nm for water to better match the MD simulation domains. In the modified wave instability model, the critical thickness δ_c is calculated by Equation 2.74, in which the constants of the surface tension deviation correlation are given in Table 2.6. Values of critical thickness δ_c calculated by the film capillarity intrinsic stability model are also listed in Table 2.6, and δ_c derived from MD simulations are also plotted in Figure 4.10 and 4.11 for argon and water respectively.

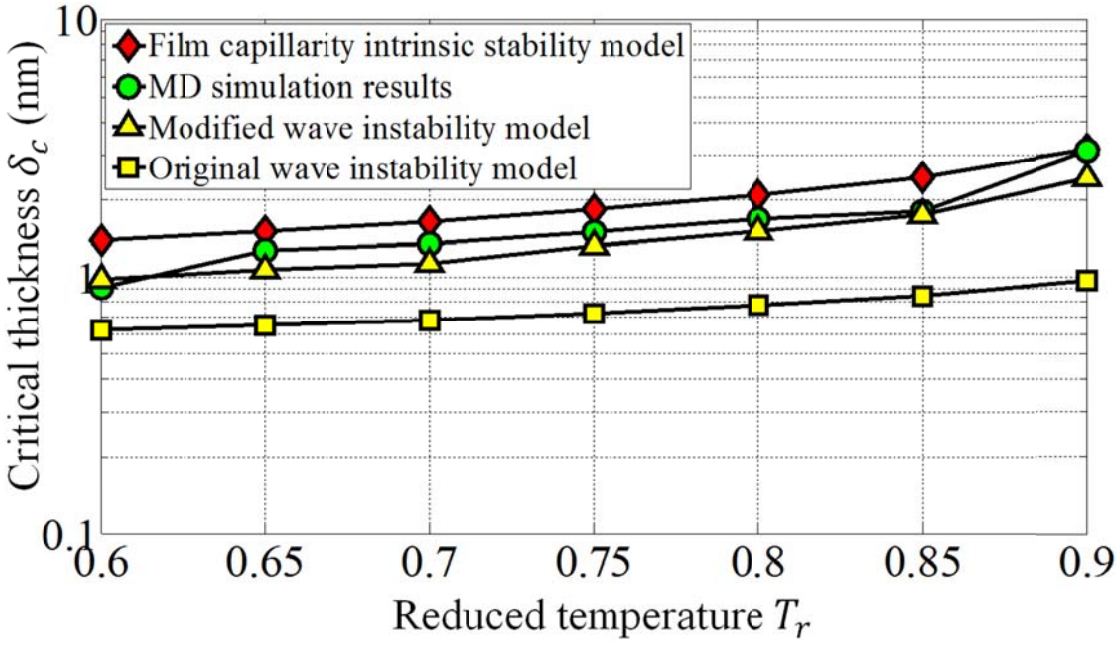

Figure 5.6 Critical thickness variations with reduced temperature predicted by the film capillarity intrinsic stability model, MD simulations, and wave instability models for the lateral dimension of the simulations ($L = 3.83$ nm) for argon

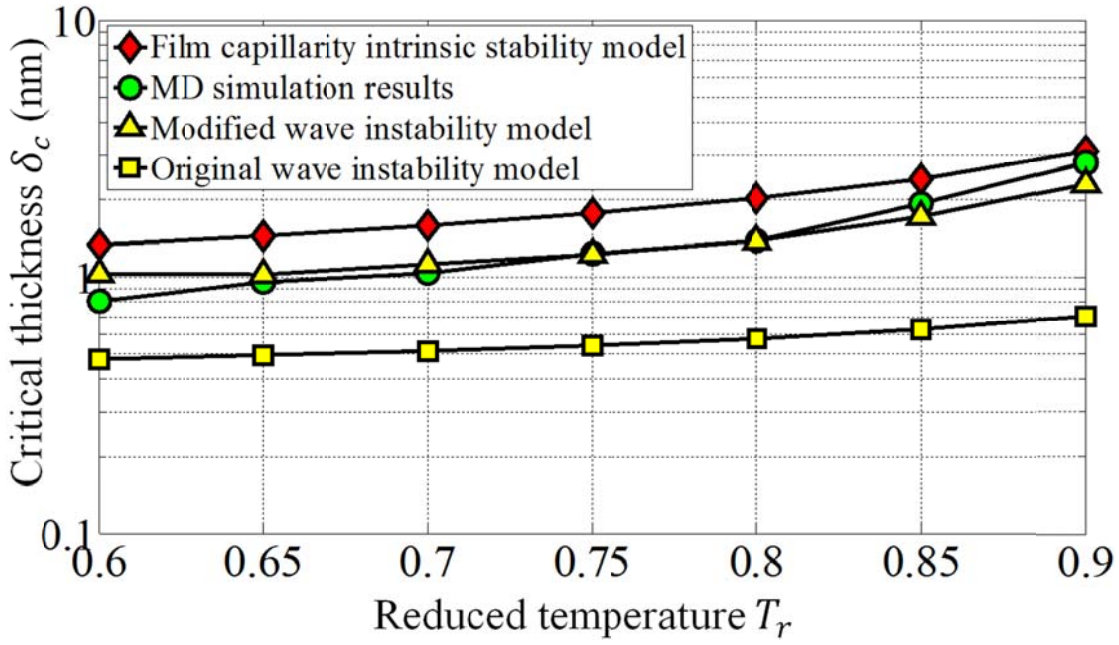

Figure 5.7 Critical thickness variations with reduced temperature predicted by the film capillarity intrinsic stability model, MD simulations, and wave instability models for the lateral dimension of the simulations ($L = 2.48$ nm) for water

From Figure 5.6 and 5.7, it is obvious that for the specific lateral film dimensions used in these MD simulations, the critical thickness observed in our MD simulations is generally below that predicted by the film capillarity intrinsic stability model, but the observed critical thickness for film rupture in the MD simulations was generally significantly greater than that predicted by the original wave instability model. For argon, the thickness for onset of rupture in our MD simulation results differs only slightly from our capillarity theory model's predictions of theδ_c, but for water, the differences are greater. This appears to be at least partly due to the fact that the identical potential function is used is both models for argon, whereas for water, the capillarity theory uses an averaged form of the SPC/E potential function used in the MD simulations. It also can be seen that the correction for the variation of surface tension with film thickness increases the wave instability model prediction of critical thickness, bringing it into better agreement with the thickness for incipient rupture observed in our argon MD simulations. For water, the predictions of this corrected version of the wave instability model indicate critical film thicknesses that are slightly larger than the MD simulation predictions. For both fluids, the modified wave instability model predictions are seen to be slightly lower than the critical thickness associated with the intrinsic theory predicted by film capillarity model. Overall, Figure 5.6 and 5.7 indicate that the predicted effect of system temperature on δ_c is consistent for all three models and MD simulations considered here.

Comparing the effect of electrolyte solute on film stability

In Figures 5.8 to 5.11, we compared the effect of four electrolyte solutes on film stability indicated by the original wave instability model, the modified wave instability model with surface tension correction, MD simulations and bubble merging experiments respectively. In the wave instability models, the lateral film dimension is set as $L = 3.5$ mm to be consistent with our bubble merging experiments. In the modified wave instability model, the critical thickness δ_c is calculated by Equation 2.74, in which the constants of the surface tension deviation correlation are given in Table 4.1 at the room temperature of 25 °C.

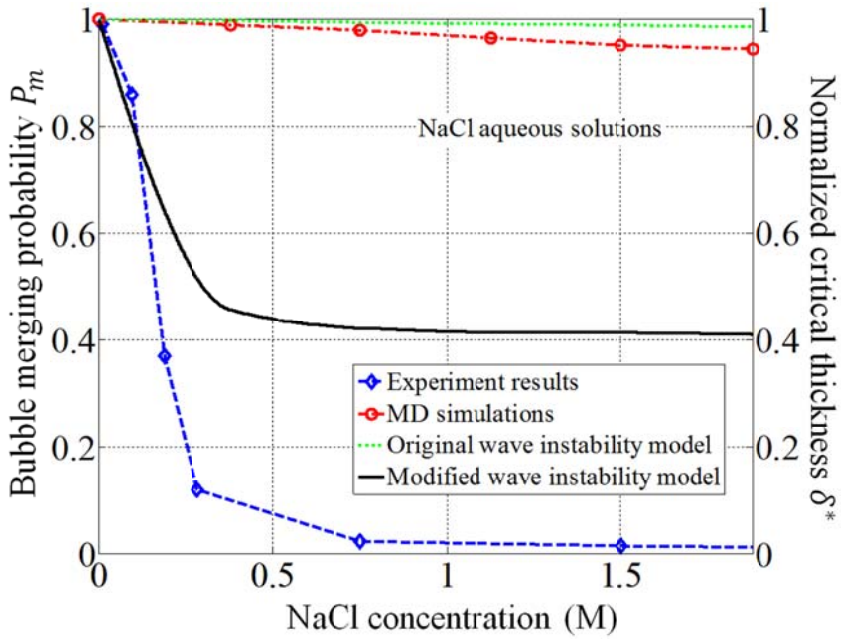

Figure 5.8 Critical thickness variations with NaCl solute concentrations predicted by wave instability models and MD simulations are compared with bubble merging probability variation from experiments

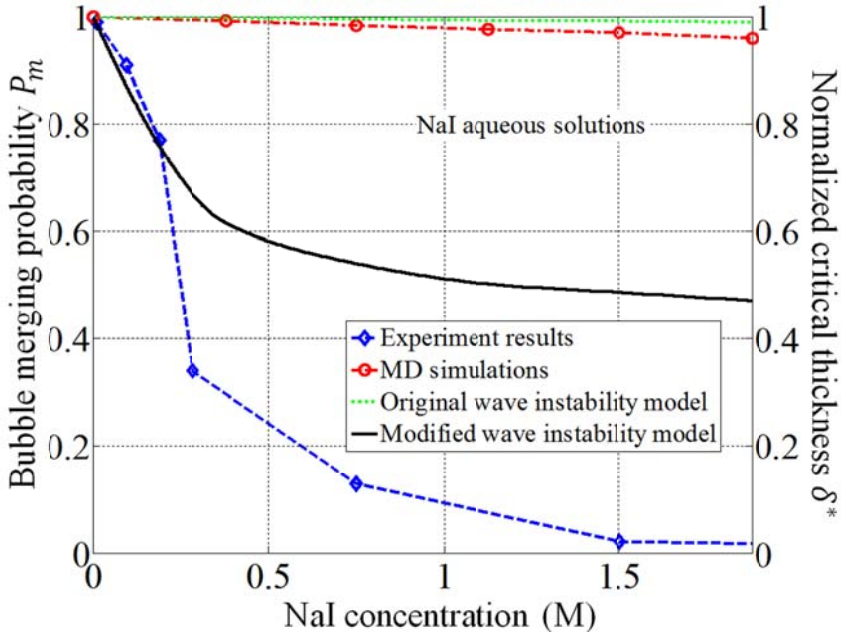

Figure 5.9 Critical thickness variations with NaI solute concentrations predicted by wave instability models and MD simulations are compared with bubble merging probability variation from experiments

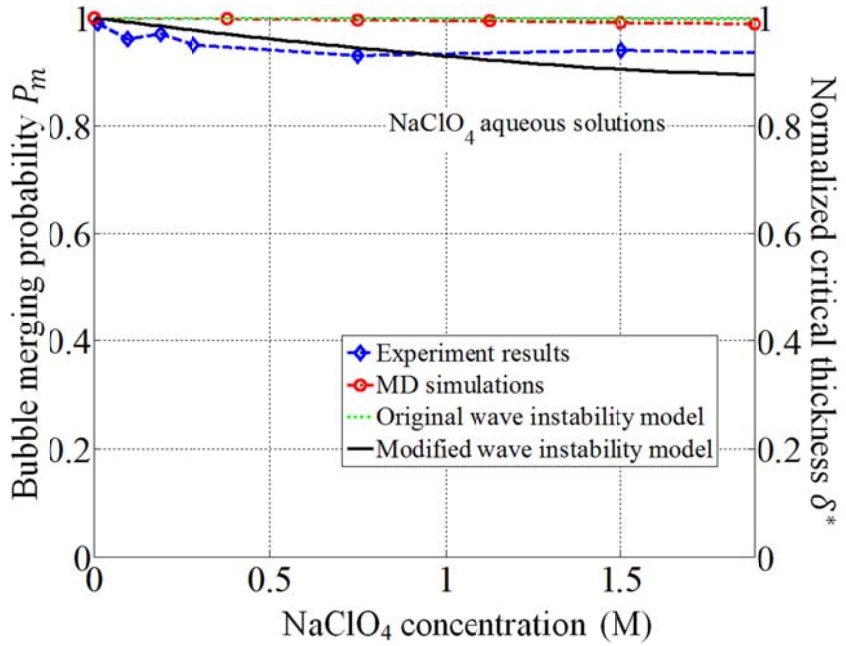

Figure 5.10 Critical thickness variations with $NaClO_4$ solute concentrations predicted by wave instability models and MD simulations are compared with bubble merging probability variation from experiments

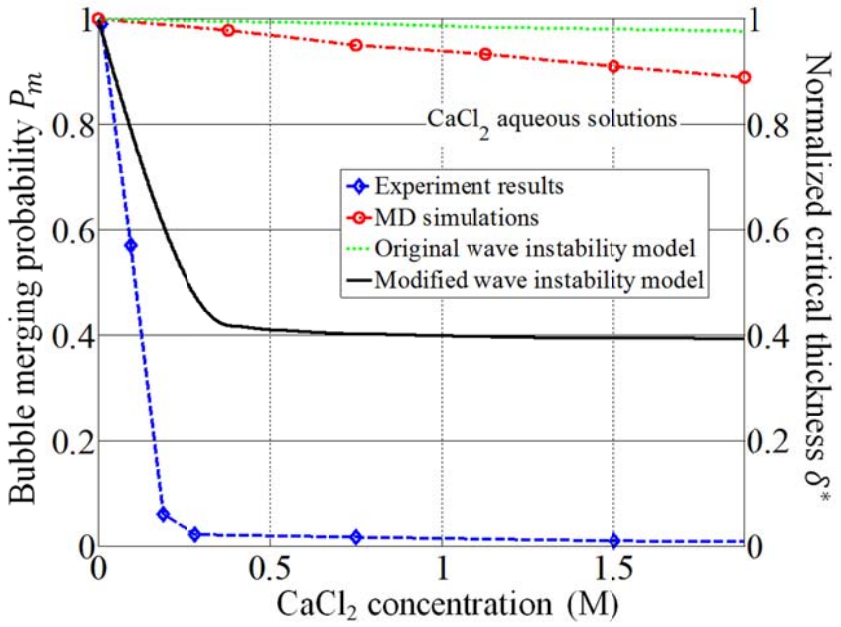

Figure 5.11 Critical thickness variations with $CaCl_2$ solute concentrations predicted by wave instability models and MD simulations are compared with bubble merging probability variation from experiments

As discussed previously, the dimensionless bubble merging probability reported by the experiment is related with the critical thickness such as the decreasing bubble merging probability indicates the decrease of critical thickness. Therefore, the critical thickness variation shown in Figures 5.8 to 5.11 is normalized to the critical thickness value in pure water predicted by corresponding models in order to present a clear comparison:

$$\delta_{c,normalized} = \frac{\delta_c}{\delta_{c,purewater}} \tag{5.1}$$

In previous discussion of the film capillarity theory, it is found that above a certain lateral film size transition value L_{tran}, the critical thickness δ_c predicted by wave instability is greater than that predicted by the intrinsic stability mechanism, as shown in Figure 2.17 and 2.18. This implies that for films with lateral extents great than L_{tran}, as a film becomes thinner it would become wave unstable first. For a film with $L < L_{tran}$, its rupture is more likely due to the lack of intrinsic stability before wave instability occurs. This transitional lateral film size L_{tran} is also found in MD simulations for electrolyte aqueous solution by comparing the δ_c predicted by MD simulations with that derived from Equation 2.74. For electrolyte concentrations in the range considered here (< 4 M), L_{tran} is on the order of 10 nm. Since in the experiment the lateral

dimension of the separating film $L \approx 3.5$ mm is orders of magnitude greater than the transitional dimension L_{tran}, the film ruptures observed during the experiment are expected to be due to the wave instability rather than lack of intrinsic stability predicted by MD simulations. As it is expected, Figures 5.8 to 5.11 show that the modified wave instability model with interfacial region thickness taking into account has the best agreement with the experiment results. For NaCl, NaI and $CaCl_2$ solutions, the results indicate steep declines in film critical thickness precisely over the range of concentrations in which the measured probabilities of bubble merging rapidly drop to a value close to zero. And for $NaClO_4$ aqueous solutions, the presence of the salt and its concentration variations do not show significant effects on liquid film stability and bubble coalescence.

§ 5.4 SUMMARY

In this chapter, the setup and procedure of bubble merging experiments have been discussed in detail. Four common engineering inorganic electrolytes: NaCl, NaI, $NaClO_4$ and $CaCl_2$ are examined in the experiments to study their impacts on bubble coalescence and the stability of the liquid film separating adjacent bubbles. Various electrolyte concentration solutions have been tested and the bubble merging probabilities are reported and compared with coalescence experiment results reported by other researchers.

Conclusions of film stability analysis reached by the wave instability models, the film capillarity intrinsic stability model, MD simulations and bubble merging experiments are compared. The first comparison is made among the wave instability models, the film capillarity intrinsic stability model, and MD simulations, using argon and pure water as examples. The effects of system temperatures on film stability are demonstrated in this comparison and consistent trends of critical thickness variation with temperatures are shown for all three models and MD simulations. The second comparison is made among the wave instability models, MD simulations and experiments, using electrolyte aqueous solutions as examples. Because the critical thickness is not directly measured in experiments, the relationship between the bubble merging probability and the film stability is examined first, proposing a comparison on a dimensionless basis. The effects of electrolyte solute concentration on film stability are demonstrated in this comparison and consistent trends of critical thickness variation with electrolyte concentrations are shown for the wave instability models, MD simulations and experiments, in which the modified wave instability model with interfacial region thickness taking into account has the best agreement with the experiment results.

CHAPTER 6 – CONCLUSIONS

In this report, the thin liquid film stability has been investigated by three strategies: thermodynamics theoretical analysis, molecular dynamics computer simulations and bubble merging experiments.

The thermodynamics theoretical analysis has demonstrated the viability of extending classical molecular capillarity theory to a full free liquid film. This extension has been formulated for molecules that are well-modeled by a Lennard-Jones interaction potential, and applied to argon liquid films. We have also developed the extension of capillarity theory to liquid water films by incorporating an averaged form for the SPC/E interaction potential which accounts for the dipole character of water. This new approach to modeling liquid water films predicts half film excess free energy values for thick films that agree well with NIST recommended values of interfacial tension between bulk liquid and vapor water phases.

The investigation documented here also demonstrated the usefulness of combining the film capillarity theory with MD simulations using the same or similar molecular interaction potentials. The capillarity theory, although more idealized, provides closed form relations that predict the relationships among parameters that govern the film structure and thermophysical behavior. The use of comparable MD simulations allows more detailed explorations of the molecular-level features of the film structure and thermophysics. Using approaches of both the film capillarity theory and MD simulations, we have deduced the conditions for incipient film rupture due to lack of intrinsic stability in the film core, and we have demonstrated that this prediction is close to observed film rupture conditions indicated by comparable MD simulations. Specifically, the critical film thickness corresponding to incipient film rupture for a thinning film predicted by the capillarity theory model was shown to be slightly higher than that observed in the corresponding MD simulation.

A key outcome of the film capillarity theory and MD simulations is the prediction that surface tension diminishes as the film thickness decreases below a threshold value of film thickness. The capillarity theory model predicts that for argon and water at $T_r < 0.9$, the film thickness must drop to less than a few nanometers for surface tension reduction to be significant. Our comparable MD simulations confirm this trend. Free liquid films between bubbles during boiling and two-phase flow are frequently much thicker than a few nanometers and we therefore expect that the effect of film thickness on surface tension will be negligible in those cases. The effect can be significant, however, as the liquid film thins towards conditions for onset of rupture, or for bubbles of small physical size in, for example, nanostructured boiling surfaces.

The predictions of the film capillarity theory model indicate that lack of core intrinsic stability in the liquid film can be a mechanism for onset of film rupture if the film thins to below 5 nm in

thickness without rupturing due to some other mechanism. Wave instability theory for thin free liquid films indicates that liquid films of macroscopic lateral extent will rupture by wave instability at film thicknesses much larger than 10 nm. However, our capillarity theory model and the comparable MD simulations both indicate that films with lateral extent on the order of 10 nm can be stable to thicknesses below 10 nm nanometers, and in such cases, lack of intrinsic stability may be the dominant mechanism that initiates film rupture. The results of our investigation also indicate that for films with thicknesses less than 10 nm, wave instability theory should be modified to account for the effects of surface tension reduction with film thickness.

As at the molecular level, the MD simulation is used as our exploratory and verificational tool, at the macroscopic levels, the bubble merging experiment is designed and carried out for electrolyte aqueous solutions to validate our conclusions reached by the modified version of wave instability model and MD simulations. We measured how salt concentration affects bubble merging probability in saline solutions and clearly defined how dissolved ionic solids would impact the film stability that plays a key role in bubble merging mechanism. Our experiments have shown that the presence of some types of electrolyte solutes in water makes it less likely that bubbles brought into contact will merge, which is consistent with the trend indicated by MD simulations and wave instability models. However, for bubbles with dimensions in the micron range or larger, wave instability is expected to be the dominant mechanism for film rupture. The prediction of critical thickness by our modified version of wave perturbation theory was consistent with our experimental results. For some types of electrolyte solutes, the improved wave perturbation model indicates a steep decline in film critical thickness precisely over the range of concentration in which the measured probability of bubble merging rapidly drops to a value close to zero, implying that the decrease in critical film thickness is enhancing the stability of the film and suppressing bubble merging.

Although the film molecular capillarity theory and the MD simulation models described here have limited accuracy in the systems of interest, and the bubble merging experiments in this study are limited in scope, they provide important insight into the free liquid film stability, and shed light on the effects of system variables on the stability, which are of significant engineering importance for applications involving coalescence of bubbles, two-phase flows, and collapse of foams.

REFERENCES

[1] H.B. Squire, Investigation of the instability of a moving liquid film, Br. J. Appl. Phys. 4 (1953) 167–169.
[2] W.W. Hagerty, J.F. Shea, A study of the stability of plane fluids sheets, Trans. ASME, J. Appl. Mech. 22 (1955) 509–514.
[3] A. Scheludko, Proc. Koninkl. Ned. Akad. Wet. Ser. B 65 (1) (1962) 87–96.
[4] A. Vrij, Possible mechanism for the spontaneous rupture of thin free liquid films, Discuss. Faraday Soc. 42 (1966) 23–33.
[5] A. Vrij, J. Th. G. Overbeek, Rupture of thin liquid films due to spontaneous fluctuations in thickness, J. Amer. Chem. Soc. 90 (1968) 3074–3078.
[6] W.A.B. Donners, A. Vrij, The critical thickness of thin free liquid films, Colloid Polym. Sci. 256 (1978) 804–813.
[7] C.A. Miller, Interfacial Phenomena, Marcel Dekker Inc., 1985. pp. 215–216.
[8] B. Radoev, A. Scheludko, E. Manev, Critical thickness of thin liquid films: theory and experiment, J. Colloid Interface Sci. 95 (1983) 254–265.
[9] E. Manev, R. Tsekov, B. Radoev, Effects of thickness non-homogeneity on the kinetic behavior of microscopic foam film, J. Dispers. Sci. Technol. 18 (1997) 769–788.
[10] T. Dong, Z. Yang, H. Wu, Molecular simulations of R141b boiling flow in micro/nano channel: interfacial phenomena, Energy Conversion Manag. 47 (2006) 2178–2191.
[11] C. Li, Z. Wang, P.-I. Wang, Y. Peles, N. Koratkar, G.P. Peterson, Nanostructured copper interfaces for enhanced boiling, Small (2008) 1084–1088.
[12] A.J. De Vries, Foam Stability, Part IV. Kinetic and Activation Energy of Film Rupture, Recueil des Travaux Chimiques des Pays-Bas 77 (1958) 383–399.
[13] J. S. Rowlinson, The thermodynamic theory of capillarity under the hypothesis of a continuous variation of density, J. Stat. Phys. 20 (1979) 200-244.
[14] V.P. Carey, Thermodynamic properties and structure of the liquid–vapor interface: a neoclassical Redlich–Kwong model, J. Chem. Phys. 118 (2003) 5053–5064.
[15] V. P. Carey, Statistical Thermodynamics and Microscale Thermophysics, Cambridge University Press, Cambridge, 1999.
[16] I. S. Sokolnikoff, R. M. Redheffer, Mathematics of Physics and Modern Engineering, McGraw-Hill, Inc., 1966.
[17] C.D. Holcomb, P. Clancy, J.A. Zollweg, A critical study of the simulation of the liquid–vapor interface of a Lennard-Jones fluid, Mol. Phys. 78 (1993) 437–459.
[18] R. Godawat, S.N. Jamadagni, J.R. Errington, S. Garde, Structure, stability, and rupture of free and supported liquid films and assemblies in molecular simulations, Ind. Eng. Chem. Res. 47 (2008) 3582–3590.
[19] M. Chen, Z.-Y. Guo, X.-G. Liang, Molecular simulation of some thermophysical properties and phenomena, Microscale Thermophys. Eng. 5 (2001) 1–16.
[20] A.P. Wemhoff, V.P. Carey, Molecular dynamics exploration of properties in the liquid–vapor interfacial region, Paper HT2003-47158, in: Proceedings of the ASME Summer Heat Transfer Conference, Las Vegas, NV, 2003.
[21] A.P. Wemhoff, V.P. Carey, Surface tension evaluation via thermodynamic analysis of statistical data from molecular dynamic simulations, Paper HT- FED04-56690, in: Proceedings of the 2004 ASME Heat Transfer/Fluids Engineering Summer Conference,

Charlotte, NC, 2004.
[22] J.G. Weng, S. Park, J.R. Lukes, C.L. Tien, Molecular dynamics investigation of thickness effect on liquid films, J. Chem. Phys. 113 (2000) 5917–5923.
[23] J. Alejandre, D.J. Tildesley, G.A. Chapela, Molecular dynamics simulation of the orthobaric densities and surface tension of water, J. Chem. Phys. 102 (1995) 4574–4583.
[24] L.X. Dang, T.-M. Chang, Molecular dynamics study of water clusters, liquid, and liquid–vapor interface of water with many-body potentials, J. Chem. Phys. 106 (1997) 8149–8159.
[25] M. Matusmoto, Y. Takaoka, Y. Kataoka, Liquid–vapor interface of water–methanol mixture. I. Computer simulation, J. Chem. Phys. 98 (1993) 1464–1472.
[26] H. Daiguji, Molecular dynamics study of n-alcohols adsorbed on an aqueous electrolyte solution, J. Chem. Phys. 115 (2001) 1538–1549.
[27] M. Tarek, D.J. Tobias, M.L. Klein, Molecular dynamics of an ethanol–water solution, Physica A 231 (1996) 117–122.
[28] J. Alejandre, D.J. Tildesley, G.A. Chapela, Fluid phase equilibria using molecular dynamics: the surface tension of chlorine and hexane, Mol. Phys. 85 (1995) 651–663.
[29] A. Hariharan, J.G. Harris, Structure and thermodynamics of the liquid–vapor interface of fluorocarbons and semifluorinated alkane diblocks: a molecular dynamics study, J. Chem. Phys. 101 (1994) 4156–4165.
[30] P. K. Weissenborn, R. J. Pugh, Surface tension of aqueous solutions of electrolytes: Relationship with ion hydration, oxygen solubility, and bubble coalescence, J. Colloid and Interface Science 184 (1996) 550-563.
[31] A. A. Abramzon, R. D. Gaukhberg, Surface tension of salt solutions, Russian Journal of Applied Chemistry 66 (1993) 1139.
[32] B. Svenningsson, Hygroscopic growth and critical super-saturations for mixed aerosol particles of inorganic and organic compounds of atmospheric relevance, Atmospheric Chemistry and Physics Discussions 5 (2005) 2833–2877.
[33] N. Matubayasi, Thermodynamic quantities of surface formation of aqueous electrolyte solutions, Journal of Colloid and Interface Science 209 (1999) 398-402.
[34] N. Ikeda, M. Aratono, K. Motomura, Thermodynamics study on the adsorption of sodium chloride at the water/hexane Interface, Journal of Colloid and Interface Science 149 (1991) 208-215.
[35] J. W. Gibbs, Collected works Vol. I, New Haven, Yale University Press, (1957) 219-331.
[36] R. R. Lessard, S. A. Zieminski, Bubble coalescence and gas transfer in aqueous electrolytic solutions, Ind. Eng. Chem. Fundam. 10 (1971) 260-269.
[37] M. E. Aguilera, A. L. Ramos, Effect of electrolytes on bubble coalescence in columns observed with visualization techniques, Ann. N.Y. Acad. Sci. 972 (2002) 242-246.
[38] L. Liendo, Estudio de la Coalescencia de Burbujas en Sistemas Electrolíticos, Thesis, Universidad Simón Bolívar, Chemical Engineering Department, Caracas, Venezuela (1998).
[39] H. J. C. Berendsen, J. R. Grigera, T. P. Straatsma, The missing term in effective pair potentials, J. Chem. Phys. 91 (1987) 6269–6271.
[40] L.D. Landau, E.M. Lifshitz, The Classical Theory of Fields, fourth ed., Pergamon Press, Oxford, 1994.
[41] NIST webbook: <http://webbook.nist.gov/chemistry/>, 2009.
[42] R.C. Tolman, Effect of droplet size on surface tension, J. Chem. Phys. 17 (1949) 333–

343.
[43] M.J. Haye, C. Bruin, Molecular dynamics study of the curvature correction to the surface tension, J. Chem. Phys. 100 (1989) 556–559.
[44] H.R. Pruppacher, J.D. Klett, Microphysics of Clouds and Precipitation, Reidel, Dordrecht, The Netherlands, 1980.
[45] J. Israelachvili, Intermolecular and Surface Forces, Academic, London, 1992.
[46] Reference database, J. Phys. Chem, 24 (1995) 1.
[47] Landolt-Bornstein, Numerical Data and Functional Relationships in Science and Technology, Springer, NY, 1982
[48] Reference database, J. Phys. Chem 19 (1990) 3.
[49] H., Goldstein, Classical mechanics, Addison-Wesley, MA, 1950.
[50] G. E. P., Box, M. E., Muller, A note on the generation of random normal deviates, Ann. Math. Stat., 29 (1958) 610-611
[51] V. P. Carey, N. E. Hawks, Stochastic modeling of molecular transport to an evaporating micro-droplet in a superheated gas, J. Heat Transfer, 117 (1995) 432-439
[52] M. Mecke, J. Winkelmann, J. Fischer, Molecular dynamics simulations of the liquid-vapor interface: the Lennard-Jones fluid, J. Chem. Phys., 107 (1997) 9264-9270.
[53] A. Trokhymchuk, J. Alejandre, Computer simulations of liquid-vapor interface in Lennard-Jones fluids: Some questions and answers, J. Chem. Phys., 111 (1999) 8510-8523.
[54] S. D. Stoddard, J. Ford, Numerical experiments on the stochastic behavior of a Lennard-Jones system, Phys. Rev., A8 (1973) 1504-1512
[55] W. B. Streett, D. J. Tildesdley, G. Saville, Multiple time step methods and an improved potential function for molecular dynamics simulations of molecular liquids, Computer modeling of matter, ACS symposium series, 86 (1978) 144-158
[56] J. J. Nicolas, K. E. Gubbins, W. B. Streett, D. J. Tildesdley, Equation of state for the Lennard-Jones fluid, Mol. Phys., 37 (1979) 1429-1454
[57] J. G. Powles, W. A. B. Evans, N. Quirke, Non-destructive molecular dynamics simulation of molecular fluids, Mol. Phys., 38 (1982) 1347-1370
[58] D. E. Smith, L. X. Dang, Computer simulations of NaCl association in polarizable water, J. Chem. Phys., 100 (1994) 3757-3766.
[59] S. Koneshan, J. C. Rasaiah, Solvent structure, dynamics, and ion mobility in aqueous solutions at 25°C, J. Phys. Chem. B, 102 (1998) 4193-4204.
[60] S. Paul, A. Chandra, Dynamics of water molecules at liquid-vapor interfaces of aqueous ionic solutions: Effects of ion concentration, Chem. Phys. Lett., 373 (2003) 87-93.
[61] P. Sandeep, M. P. Florian, Molecular dynamics simulation of aqueous NaF and NaI solutions near a hydrophobic surface, J. Phys. Chem. B., 109 (2005) 6405-6415
[62] E. Guardia, G. Sese, J. A. Padro, S. G. Kalko, Molecular dynamics simulation of Mg^{2+} and Ca^{2+} ions in water, Journal of Solution Chemistry, 28 (1999) 1113-1126.
[63] D. B. Marcel, W. K. I-Feng, B. Hendrik, G. Sutapa, Interfacial behavior of perchlorate versus chloride ions in aqueous solutions, J. Phys. Chem. B, 113 (2009) 15843–15850.
[64] D. Frenkel, B. Smit, Understanding molecular simulation: from algorithms to applications, 2nd Ed., Academic press, San Diego, 2002
[65] D. M. Heyes, Pressure tensor of partial-charge and point-dipole lattices with bulk and surface geometries, Phys. Rev. B, 49 (1994) 755-764.
[66] J. A. Kolafa, J. W. Perram, Cutoff errors in the Ewald summation formulae for point

charge systems, Mol. Sim., 9 (1992) 351-368
[67] W. C. Swope, H. C. Andersen, P. H. Berens, and K. R. Wilson, A computer simulation method for the calculation of equilibrium constants for the formation of physical clusters of molecules: Application to small water cluster, J. Chem. Phys., 76 (1982) 637-649.
[68] H. C. Andersen, Rattle: a 'Velocity' version of the SHAKE algorithm for molecular dynamics calculations, J. Comp. Phys., 52 (1983) 24-34.
[69] J. P. Ryckaert, G. Ciccotti, H. J. C. Berendsen, Numerical integration of the Cartesian equations of motion of a system with constraints: Molecular dynamics of n-alkenes, J. Comp. Phys., 23 (1977) 327-341
[70] C. L. Tien, J. G. P. Weng, Molecular dynamics simulation of nano-scale interfacial phenomena in fluids, Advances in Applied Mechanics, 38 (2001) 95-146
[71] G. Ciccotti, J. P. Ryckaert, Molecular dynamics simulation of rigid molecules, Comp. Phys. Rep., 4 (1986) 348-392
[72] C. K. Huang, V. P. Carey, The effects of dissolved salt on the Leidenfrost transition, Int. J. Heat and Mass Transfer, 50 (2007) 269–282.
[73] J. D. Bernardin, I. Mudawar, A cavity activation and bubble growth model of the Leidenfrost point, ASME J. Heat Transfer, 124 (2002) 864-874.
[74] J. D. Bernardin, I. Mudawar, A Leidenfrost point model for impinging droplets and sprays, ASME J. Heat Transfer, 124 (2004) 272-278.
[75] V. S. J. Craig, B. W. Ninham, R. M. Pashley, Effect of electrolytes on bubble coalescence, Letters to Nature, 364 (1993) 317-319.